Wear Behaviour of A Convex Pattern Surface for Bulk Handling Equipment

Yan, Y.

DOI
10.4233/uuid:6ea7d012-cb3c-4c5b-a658-aa76e6b8f949

Publication date
2022

Document Version
Final published version

Citation (APA)
Yan, Y. (2022). *Wear Behaviour of A Convex Pattern Surface for Bulk Handling Equipment*. [Dissertation (TU Delft), Delft University of Technology]. https://doi.org/10.4233/uuid:6ea7d012-cb3c-4c5b-a658-aa76e6b8f949

Wear Behaviour of A Convex Pattern Surface for Bulk Handling Equipment

Yunpeng Yan

Delft University of Technology

Wear Behaviour of A Convex Pattern Surface for Bulk Handling Equipment

Dissertation

for the purpose of obtaining the degree of doctor
at Delft University of Technology
by the authority of the Rector Magnificus Prof.dr.ir. T.H.J.J. van der Hagen
chair of the Board for Doctorates
to be defended publicly on
Wednesday 14 December 2022 at 17:30 o'clock

by

Yunpeng YAN
Master of Science in Agricultural Mechanization Engineering, Jilin University, China
born in Shandong, China

This dissertation has been approved by the promotors.

Composition of the doctoral committee:

Rector Magnificus	chairperson
Dr.ir. DL Schott	Delft University of Technology, promotor
Dr.ir. R.L.J. Helmons	Delft University of Technology, copromotor

Independent members:

Prof.dr.ir. J.T. Padding	Delft University of Technology
Prof. Dr.-Ing. A. Katterfeld	Otto-von-Guericke University, Germany
Dr. M.W.N. Buxton	Delft University of Technology
Prof.dr.ir. C. van Rhee	Delft University of Technology
Prof.dr. C. Wheeler	University of Newcastle, Australia

The research presented in this thesis was supported by TU Delft/CSC doctoral programme.

TRAIL Thesis Series no. T2022/16, the Netherlands Research School TRAIL

TRAIL
P.O. Box 5017
2600 GA Delft
The Netherlands
E-mail: info@rsTRAIL.nl

ISBN: 978-90-5584-318-3

Printed in the Netherlands

Dedicated to
My parents, wife, and daughter Yihe.

Summary

Bulk handling plays a significant role in a range of industries, such as the mining, agricultural, chemical, and pharmaceutical industry. For the mining industry, economic development results in an increasing demand of steel and consequently the raw materials used for steel production, such as cokes and iron ore. Dealing with bulk material leads to severe wear on bulk handling equipment due to the countless contact between materials and equipment surfaces. The wear causes surface deformation and deterioration of handling equipment, bringing a high risk of reduction in the lifespan of equipment.

Inspired by a bionic design method, a previous study applied a convex pattern to a transfer chute to reduce wear caused by bulk material. The convex pattern configuration is proposed by seeking biological morphologies and categorizing the corresponding wear reduction mechanisms of each morphology. A numerical study based on the Archard wear model using discrete element method (DEM) indicates that the convex pattern surface enables to reduce the abrasive wear by 63 % compared to a plain one.

Following the previous study, this thesis aims to reveal the principles of the convex configuration on wear reduction for bulk handling equipment and to predict the surface deformation due to the contact with bulk material. For the surface deformation, by evaluating multiple numerical methods, DEM with deformable geometry technique has the advantage to integrate bulk material and surface deformation effectively and accurately.

This thesis consists of two parts. The first part elaborates the wear mechanisms of the convex pattern surface on wear reduction with non-deformable geometry. The second part models the surface deformation caused by a single particle contact and multiple contacts from bulk material separately.

The convex configuration is optimized based on a design of experiments approach. By applying a definitive screening design, six factors including two operational conditions at three levels are evaluated. Two flow regimes, namely continuous and discontinuous flow regime, are distinguished as a result of the combination of design factors. Although the discontinuous flow regime is capable to reduce wear, it is discarded as it induces severe particle accumulation. For the continuous flow regime, a regression model indicates that three individual factors and one interaction have a significant effect on wear rate. The design with the lowest wear rate is

considered as a reference for the following study. The numerical result implies that the convex pattern sample reduces wear compared to a plain sample as it alters the bulk flow behaviour by facilitating the rolling and decelerating the sliding of particles.

As bulk handling equipment deals with multiple materials with various particle size distribution, it is essential to comprehend the effect of particle size on sliding wear of the convex pattern sample. A coarse graining technique, which is used to reduce computational time by replacing physical particles with representative parcels, is implemented to evaluate the effectiveness of the reference sample on sliding wear reduction. The result demonstrates that when the particle radius is smaller than the equivalent radius of the convex, the convex pattern sample reduces wear by altering the flow behaviour of particles. Otherwise, the particles traverse across the convex pattern, converting to the resistance of the particles and therefore leading to the increase of wear.

As the mechanisms of the convex pattern sample on wear reduction are revealed, it is crucial to investigate the effectiveness of the sample subjecting to surface deformation due to wear. DEM combined with a deformable geometry technique is implemented to model the surface deformation due to wear. As a benchmark, a single contact test, namely pin-on-disc test, is performed to evaluate the feasibility of the numerical model. Three wear properties of a meshed disc, including wear depth, wear width, and wear volume, are compared with the test results. The mesh size sensitivity indicates that the mesh size makes wear volume converge but it has a significant effect on the shape of the wear contour. After experiencing a run-in phase, the numerical results demonstrate that by properly scaling up the wear coefficient of the Archard wear model and selecting the element size, the long-time or long-distance laboratory test can be modelled by a short-term or short-distance numerical simulation. The scaling effect enables to significantly save computational effort with a promising calculation precision.

Furthermore, the surface deformation of a convex pattern sample due to the contact with bulk material is modelled. The wear experiments are performed on a circular wear tester and the results demonstrate that the convex pattern sample reduces wear by 43 % compared to a plain sample after the experiment of 56 hours. To investigate the deformation of the convex pattern sample, the wear contour is reconstructed based on the point cloud obtained from 3D scanning. The numerical model is validated by comparing the wear volume of a plain sample between the simulation and wear experiment. The simulation results indicate that the deformed convex pattern surface continues to reduce the sliding wear compared to a plain sample and the reduction performance weakens as wear evolves. On the other hand, particle size plays a significant role in the effectiveness of wear reduction on the convex pattern sample. The wear caused by contact with the particles corresponding to a lower scaling factor is less than that corresponding to a higher scaling factor and this is consistent with the study using non-deformable geometry.

In conclusion, the convex pattern surface reduces wear as it alters the flow behaviour of bulk material by strengthening the rolling and reducing the sliding of individual particles. As indicated in a validated numerical model, the surface deformation undermines the effectiveness of the convex pattern as it reduces the capability of changing the bulk flow behaviour. Compared to a plain sample, the convex pattern sample continues to reduce the sliding wear with the surface deformation.

Further work should focus on long-term laboratory testing and evaluate the feasibility of applying the convex configuration to the industry dealing with a large amount of material and facing severe wear.

Table of contents

1 Towards the wear reduction of bulk handling equipment

1.1 Wear on bulk handling equipment

Bulk handling plays a significant role in a range of industries, such as the mining, agricultural, chemical, and pharmaceutical industry [1]. For the mining industry, economic development results in an increasing demand of steel and consequently the raw materials used for steel production, such as cokes and iron ore. During the process of transferring raw materials from belt to equipment shown in Figure 1.1, the countless contacts between bulk solids and bulk handling equipment lead to severe wear.

Wear causes surface deformation and deterioration, resulting in a reduction in lifespan of equipment. The maintenance of worn area is costly and increases downtime. Therefore, the surface wear of bulk solids handling equipment must be reduced.

Figure 1.1 Transferring of iron ore from a belt conveyor through a transfer chute [2]

Abrasive wear and impact wear are considered as two principal wear mechanisms during bulk handling process [3,4]. Abrasive wear is caused by relative sliding and rolling of particles against equipment surfaces, while impact wear occurs when solid particles strike a surface. As a continuation of previous work [5], this research focuses on abrasive wear as it is the most dominant wear mechanism in transfer chutes. Roberts et al. [6] state that approximately 91 % of the energy loss contributes to bulk material sliding over the chute, with the remaining 9 % due to inter granular friction. Among the 91 % of the energy loss, around 82 % are attributed to the bulk material sliding along the chute bottom, and 9 % due to sliding against the side walls. Severe wear has been found in several locations on bulk handling equipment, for example, silo walls and transfer chute bottom sections shown in Figure 1.2 [7,8].

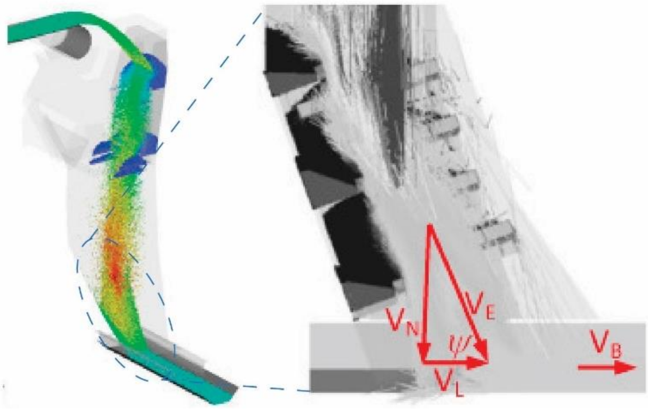

Figure 1.2 High wear area in a transfer chute [8]

Generally, to improve the wear resistance of equipment, the following five approaches can be distinguished:

1) To optimize operational conditions based on theoretical wear models [6,9]. For example, Roberts et al. [6] describe the chute flow mathematically and determine chute profiles to achieve optimum flow, as shown in Figure 1.3;

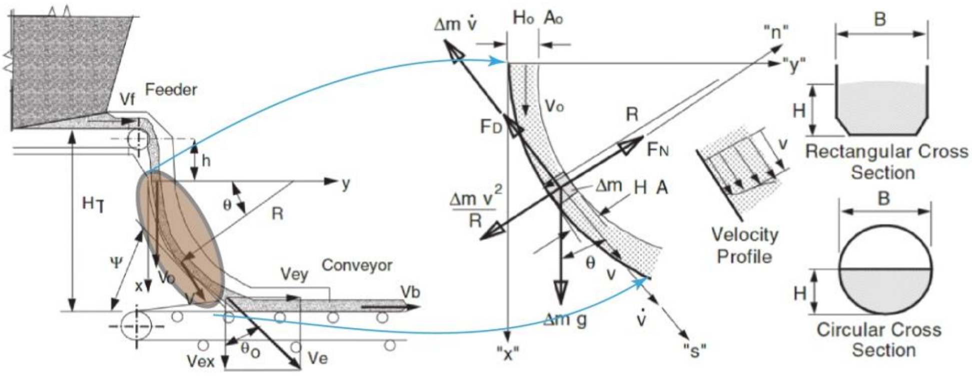

Figure 1.3 Chute design based on material flow model, based on [6]

2) To use wear-resistant materials with coating technologies [10]. For example, coatings comprised of a combination of materials in a form of multilayer have been gaining much interest and widely used to minimize and control friction and wear phenomena encountered in mechanical systems [11], as shown in Figure 1.4;

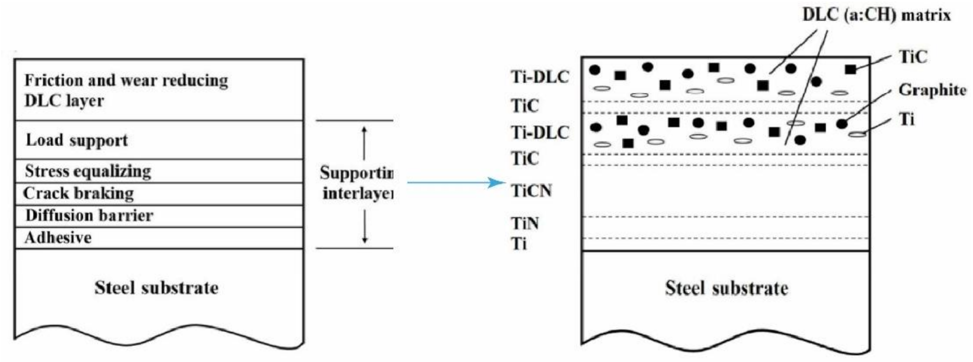

Figure 1.4 Schematic representation and example of multilayer coating [11]

3) To supply a repulsive force to diminish the contact force between particulate solids and equipment [1]. Fluidizing gas flow is distributed to the bottom of a perforated plate of a chute to facilitate the flowing of bulk material, as shown in Figure 1.5 (a);
4) To add assistant components enabling the self-wear mechanism of the bulk solids [1]. For instance, a group of ribs perpendicular to a chute bottom is mounted to form multiple chambers, so the flowing particles directly contact with the non-moving particles stored in the chambers, as shown in Figure 1.5 (b);
5) To fabricate a surface geometry pattern to change the flow behaviour of bulk material along the surface [12]. For instance, a triangular prism and partial circular column are applied to reduce drag force and therefore wear during subsoiling [13], as shown in Figure 1.5 (c).

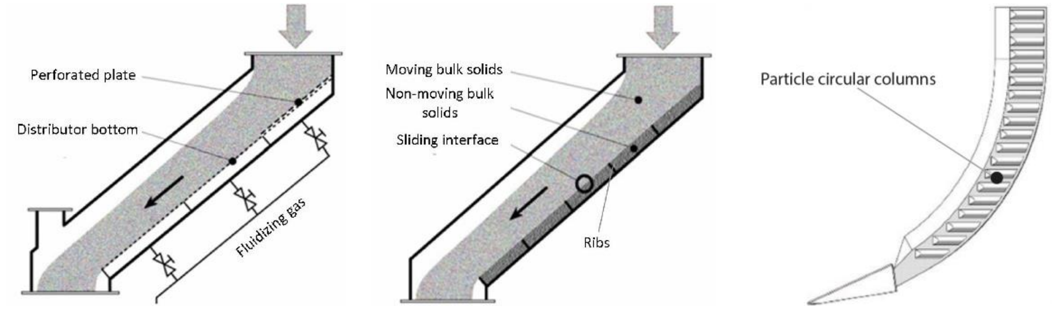

(a) (b) (c)

Figure 1.5 Three approaches to reducing wear (a) applying fluidized gas as repulsive force [5], (b) particle self-wear mechanism [5], (c) equipping geometrical patterns [13]

As an extension of approach five, bionic design [12] which embraces the practical use of mechanisms and functions of biological science in design, chemistry, engineering, and so on, has been playing a significant role in reducing wear due to contact between bulk materials and devices [13]. The bionic design method includes designing and testing various biological systems as potential prototypes and strives to make some adapted engineered versions of the biomimetic device which we are trying to develop. For example, a cemented carbide drill bit inspired biologically by a dung beetle is shown in Figure 1.6. The dome structure reduces impact and abrasion of bulk solids while the pit structure decreases friction force and prevents getting stuck when drilling. Compared to an original drill, this novel one reduces the abrasive wear rate by 23 % and increases drilling speed by 45 % [14].

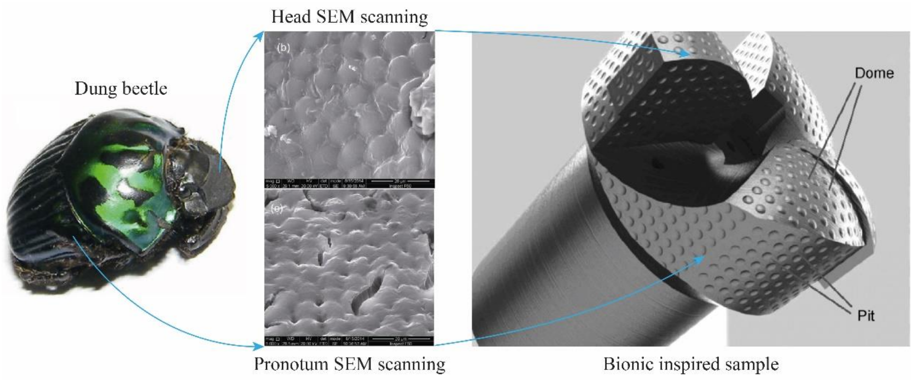

Figure 1.6 Bionic drill bit inspired by dung beetle, based on [14]

Similarly, inspired by the bionic design method, Chen [15] applied biological wear-resistant morphologies to a transfer chute for transferring free flowing material (e.g., iron ore). First, the studies sought biological morphologies which can be applied as a biological prototype are classified. Second, the corresponding wear reduction mechanism of the morphologies are categorized. Third, a geometrical design of parallelogram arrangement with semi-ellipsoids which is inspired by a convex scale on sandfish body surface was proposed (Figure 1.7). With the comparison of an original plain chute, numerical results indicate that the convex pattern equipped with bionic surface reduces abrasive wear significantly by 63 %. The success of the application of bionic design method provides a new perspective on wear reduction of bulk handling equipment.

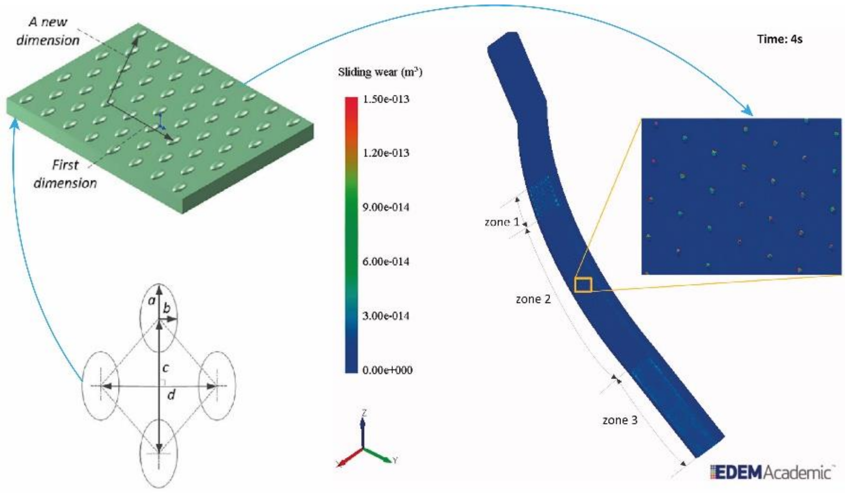

Figure 1.7 Bio-inspired transfer chute for wear reduction, based on [15,16]

However, although the designed transfer chute shows promising performance on wear reduction, three crucial aspects still need to be unfolded. First, the wear reduction mechanisms of the convex pattern for bulk handling equipment (e.g. transfer chute) need to be understood. Second, the deformation of the surface should be modelled to represent reality and to understand to what extent the sample remains reducing wear while being exposed to wear. Third, the numerical results and the effectiveness of the bionic sample on wear reduction should be verified by experiments.

1.2 Research scope

Following the previous work [5] where a convex pattern surface is applied to the wear reduction of transfer chutes based on DEM modelling, this thesis continues to reveal the mechanisms of the convex pattern sample on abrasive wear reduction performance and to predict the surface deformation caused by bulk material.

For the surface deformation during bulk handling processes, wear modelling is complex as multiple wear mechanisms coexist simultaneously. Besides, bulk material refers to a vast number of interactions instead of a single interaction. From a time scale point of view, this research deals with long term (e.g., from days to months) modelling of wear. It is unpractical to include all potential mechanisms into a single model as the surface deformation modelling is highly related to computational expenses and feasible level of modelling detail. Therefore, assumptions and requirements are set to simplify the process based on three aspects which affect wear mentioned in the previous work [5].

1) Bulk material: Individual particles are unique in multiple aspects, including angularity, hardness, and frangibility. To simplify the characteristics, the particles are assumed as rounded and rigid in this study. For the modeling of bulk material, only free flowing solids are taken into account.
2) Surface: The geometry surface is assumed as smooth with respect to surface roughness. For surface deformation, it is considered that all of the deformed geometry is removed in a form of plastic deformation. On the contrary, the elastic deformation and cracking due to fatigue are beyond the scope. Besides, the material properties, such as work hardening referring to material science (e.g. homogeneity and isotropy), are excluded from this study.
3) Operational conditions: The bulk material flows under low velocity (e.g., < 2 m/s). As impact wear normally occurs at high impact velocity, only abrasive wear is considered in this study. The effect from other perspectives, such as environmental conditions (e.g. temperature, moisture content), is ignored. Besides, the surface deformation occurs over a long time (e.g., from days to months) instead of a short time scale (e.g., seconds).

Based on the three points stated above, it can be summarized that this research focuses on the surface deformation due to the contact with free-flowing bulk material over a long time scale.

1.3 Research objective and research questions

The primary objective is to model and predict the wear rate and deformation of a convex pattern surface proposed to reduce sliding wear for a transfer chute. This can be achieved by combining discrete element method (DEM) with a deformable geometry technique.

Based on the research objective, the main research question is stated:

How to model and predict the wear reduction performance and deformation of the convex pattern surface caused by contact with bulk material?

To answer the main research question, the following five sub-questions are addressed in this thesis.

1) What are the main wear mechanisms in bulk handling and what is a suitable numerical method for wear modelling in this context?
2) What is the effect of the parameters of the convex configuration on wear reduction performance of the convex pattern surface?

3) To what extent can the convex pattern sample reduce wear for different particle size distributions?
4) In what way can the surface deformation caused by sliding of a single particle be modelled?
5) To what extent does the deformed convex pattern sample continue to reduce sliding wear caused by bulk material?

1.4 Outline of the thesis

Figure 1.8 depicts the outline of this dissertation. The chapters are related to research questions and the main contents (Chapter 3 - 6) consist of two aspects considering the modelling of surface deformation. The first aspect (Chapter 3 and 4) elaborates the wear mechanisms of the convex pattern surface on wear reduction with non-deformable geometry. The second aspect (Chapter 5 and 6) models the surface deformation caused by a single particle and bulk solids.

Chapter 2 summarizes the principal wear mechanisms and potential numerical models applied to the modelling of surface deformation. First, two wear mechanisms with the corresponding multiple wear modes are specified. Second, seven numerical methods used for modelling surface deformation due to wear are evaluated, including finite element method (FEM), discrete element method (DEM), smoothed particle hydrodynamics (SPH), element deletion method (EDM), DEM with deformable geometry, and corresponding coupled methods.

Chapter 3 optimizes the convex pattern sample to reduce sliding wear based on a design of experiments approach and reveals the mechanisms of the wear reduction of a convex pattern sample. A definitive screening design is applied to sort out the critical factors and second-order interactions between factors. Two flow regimes are identified with respect to the flow behaviour of particles. The essential mechanisms of the convex pattern sample enabling to reduce sliding wear are clarified and an optimal design is obtained for further investigation.

Chapter 4 investigates the effect of particle size on the wear reduction properties of the sample obtained in Chapter 3. A coarse graining technique is applied and the effect of particle size on wear volume of the sample is formulated. A relation indicates the boundary where the convex pattern sample has positive or negative effect on wear reduction with respect to particle size distributions.

As a benchmark, **Chapter 5** establishes a pin-on-disc numerical model to study surface deformation caused by a single contact. A geometrical deformation technique is implemented to predict a long time laboratory test with an acceptable short time-span numerical model. The wear contours are extracted and analysed statistically and compared with test results.

Chapter 6 models the surface deformation of the convex pattern surface caused by bulk material. As a benchmark, the wear experiments are conducted to verify the numerical model. Wear properties, including wear volume, wear distribution, and 3D reconstruction, are used to demonstrate the effect of the convex pattern sample on sliding wear reduction. The numerical model reveals the effectiveness of the deformed convex pattern sample on wear reduction compared to a plain sample.

The overall conclusions and recommendations are summarized in **Chapter 7**.

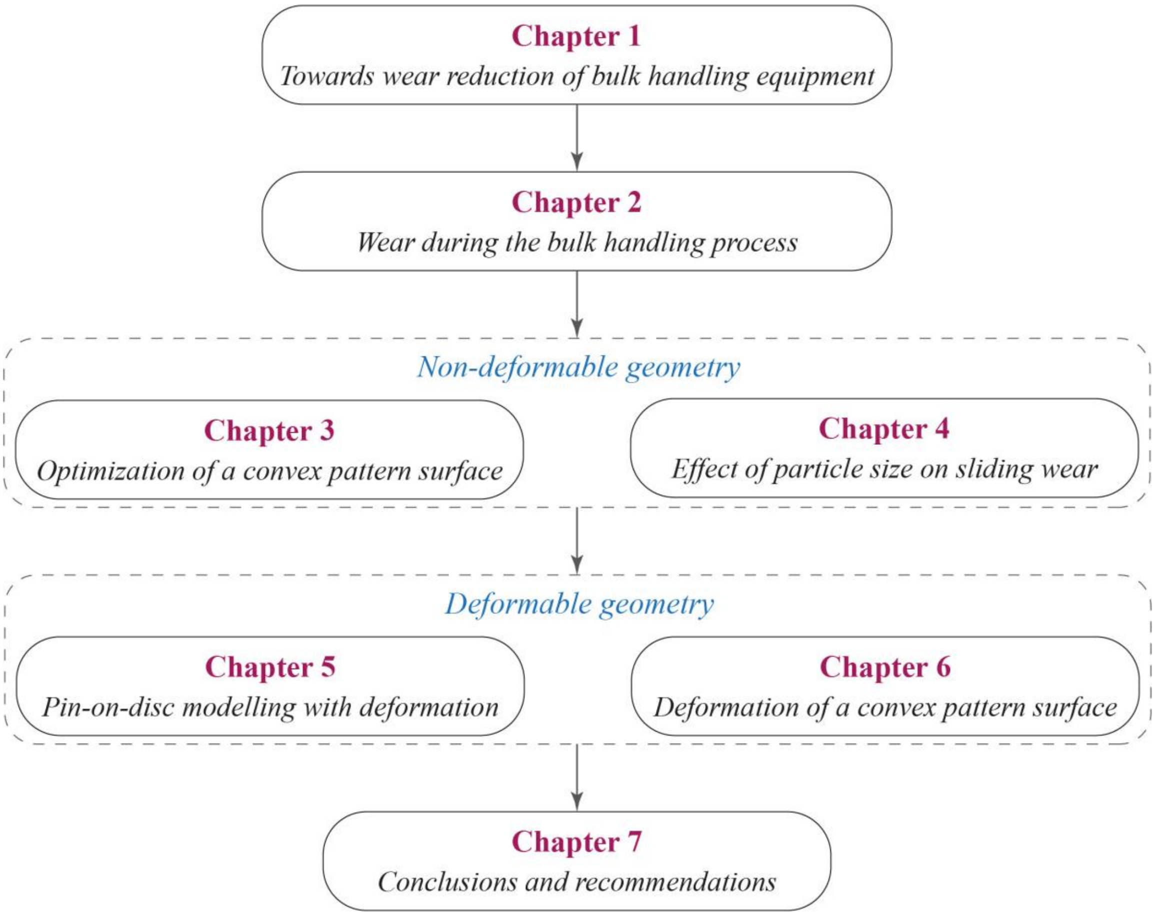

Figure 1.8 Outline of this dissertation

2 Wear during bulk handling

Wear of bulk handling equipment is a complicated process. To comprehend the surface deformation caused by the contact between bulk material and handling equipment, this chapter explains the wear mechanisms, system characteristics, and potential numerical methods relevant to modeling surface deformation. In Section 2.1, the two principal wear mechanisms, namely abrasive wear and impact wear, are elaborated. Section 2.2 introduces the three system characteristics. Section 2.3 describes numerical methods for the modelling of surface deformation caused by wear. Section 2.4 concludes the wear mechanisms and the most suitable numerical method to model the surface deformation of bulk handling equipment.

2.1 Wear mechanisms

The wear mechanisms play a significant role in the surface deformation during bulk handling processes, and abrasive and impact wear are considered as the two principal wear mechanisms.

2.1.1 Abrasive wear

Abrasive wear is caused by a relative sliding and rolling of particles against an equipment surface [17]. For abrasive wear, material is displaced or removed from a contact surface by hard particles, or by hard protuberances on a counter face, forced against and moving along the surface. Abrasive wear occurs in two forms which are two-body abrasion and three-body abrasion [17,18]. Two-body abrasive wear is caused by abrasive particles simply sliding against a surface [19], while three-body abrasion happens by both sliding and rolling of particles [17]. For two-body abrasive wear, translation is the only motion of particles. However, for three-body abrasive wear, the motion of particles also includes rotation. As a result, the two-body abrasion causes higher wear rate than three-body abrasion. Depending on handling operations, equipment surfaces can suffer these two abrasions at the same time. In some situations, particles may slide in one region of a contact, but roll in another. It is therefore more convenient and helpful to classify abrasive wear as either sliding abrasion or rolling abrasion as shown in Figure 2.1, relying on the motion of the particles. It should be noted that the body above the particles could also be represented as a bed of particles.

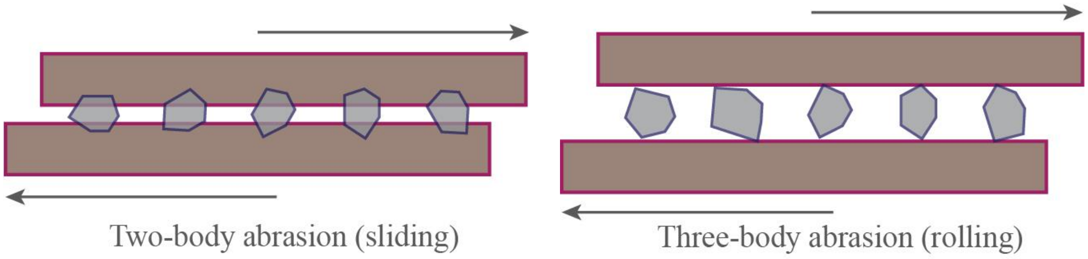

(a) (b)

Figure 2.1 Illustration of abrasive wear (a) sliding abrasion, (b) rolling abrasion, based on [17]

In practice, however, particles with irregular shapes deform a surface in different ways. Abrasive particles can deform the material in ways that lead to the removal of only part of the material displaced from the groove, or even to the removal of no material at all [17].

The surface deformation caused by abrasive wear is relevant to the properties of surface material summarized in Section 2.2. For ductile material, it is considered that the three following main wear modes contribute to the surface deformation [17,20], which are (see Figure 2.2):

1) Micro-cutting (Figure 2.2 (a)), in which material is deflected through a shear area and flows up the front face of the particle to form a chip [17].
2) Micro-ploughing (Figure 2.2 (b)), in which a ridge of deformed material is pushed along a piece of the particle [17].
3) Wedge formation (Figure 2.2 (c)), in which represents intermediate behaviour and leads to, like the cutting mode, to removal of material from the surface [17].

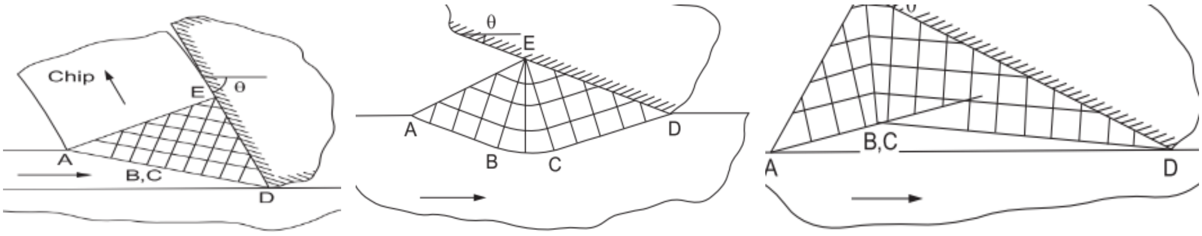

(a) (b) (c)

Figure 2.2 Wear modes of ductile material [17]
(a) micro-cutting, (b) micro-ploughing, (c) wedge formation

Figure 2.3 shows that the cracks form in a brittle surface subjected to a concentrating load and spread beneath the sharp rigid indenter. At the point of initial contact, high stresses occur. When the load on the indenter increases to a critical value associated with the material, tensile stresses across the vertical mid-plane induce a median crack. Further increase in load is accompanied by progressive extension of the cracks. After the unloading lateral cracks are formed and the formation of these cracks is driven by residual elastic stresses [17].

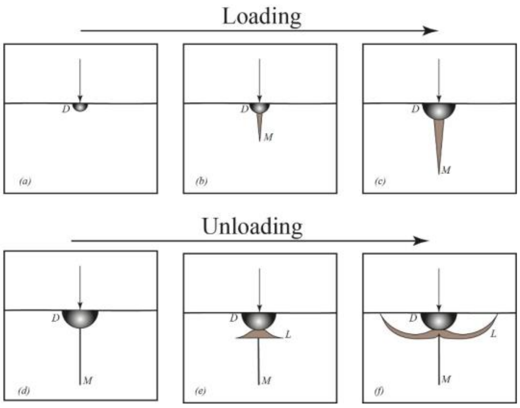

Figure 2.3 Crack formation in a brittle material due to point indentation, based on [17]

For brittle material, micro-cracking is a main mode of wear as highly concentrated stresses are imposed by abrasive particles based on the removal of material by lateral cracking. As a sharp particle slides over the surface forming a plastic groove, lateral cracks grow upwards to the free surface from the base of the sub- surface deformed region [17].

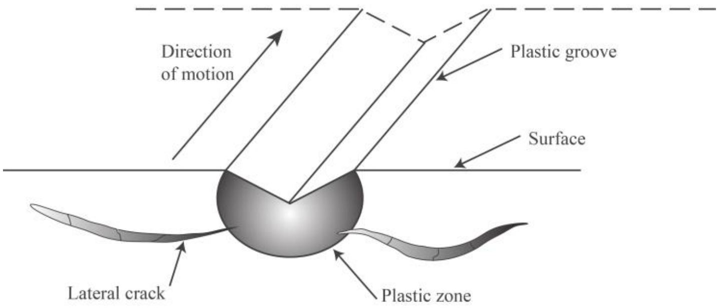

Figure 2.4 Schematic illustration of material removal in a brittle material, based on [17]

2.1.2 Impact wear

Impact wear occurs when discrete solid particles strike a surface [18] (see Figure 2.5). This type of wear is called erosion, often qualified as solid particle erosion or solid impingement erosion to distinguish it from the damage caused by the impact of liquid jets or drops [17]. It differs from three-body abrasion as it involves loose particles impacting a surface in the origin of the forces from the contact between particles and a surface. As shown in Figure 2.6, multiple forces from different origins may generate an action on a particle contacting with a solid surface. Contact forces may be exerted from neighboring particles, and drag force will be triggered by a flowing fluid if present. However, the dominant force on an impact particle is usually the contact force exerted by the surface. This is because the contact force is responsible for decelerating the particle from its initial impact velocity. Impact wear depends not only on the number and mass of individual particles striking the surface, but on their impact velocity [21,22]. Therefore, it is reasonable to state that the main differences for three-body abrasive wear and impact wear are contact time between particles and surface and the relative normal velocity.

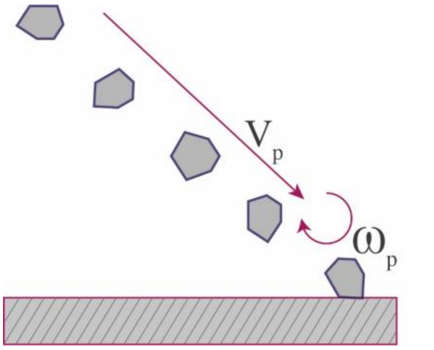

Figure 2.5 Schematic of impact wear, based on [18]

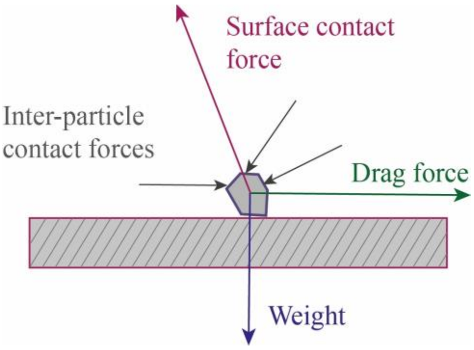

Figure 2.6 Schematic of forces acting on a particle, based on [22]

The wear modes of the impact wear are generally considered different depending on impact angels [23–25]. Similarly, the surface deformation of the impact wear is related to material properties. For ductile material, it is considered that two main wear modes contribute to the surface deformation at low and high contact angles responsively, which are (see Figure 2.7)

1) Micro-cutting, in which the surface is highly deformed to raise the material into a prominent chips. The surface deformation caused by a single angular particle is dependent on the orientation of the particle when it strikes the surface, and on whether the particle rolls forwards or backwards during contact. Type 1 cutting is defined as a particle rolling forward, and Type 2 when rolling backward.

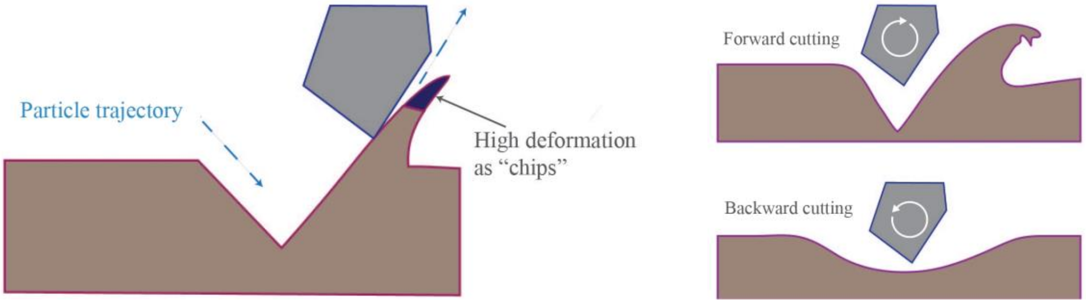

(a) (b)

Figure 2.7 Cutting mode of impact wear (a) illustration of particle cutting, (b) two types of cutting, based on [17,26]

2) Lip formation, in which the incidence can be thought of as an indentation process, leading the formation of crater 'lips' to highly deformed material. As a result, the lips are subsequently removed as platelets after being impacted by successive particles. This deformation mode embraces both the ploughing and wedge-formation of abrasive wear.

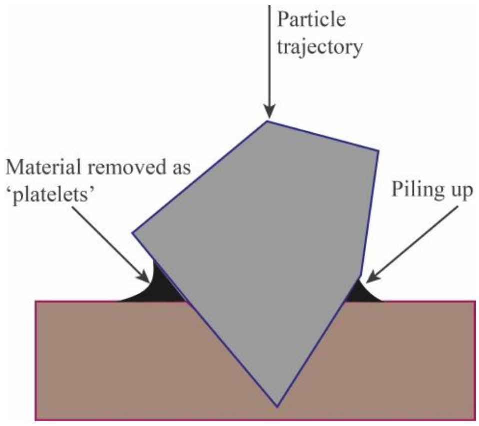

Figure 2.8 Mode of lip formation of impact wear, based on [26]

2.2 System characteristics

Generally, the trends of wear loss of materials depend not only on properties of particles, but also on the wearing materials as well as the operational conditions [17]. As each aspect involves multiple characteristics and some exceeds the scope of this research, Figure 2.9 specifies the possible properties and conditions for the three system characteristics.

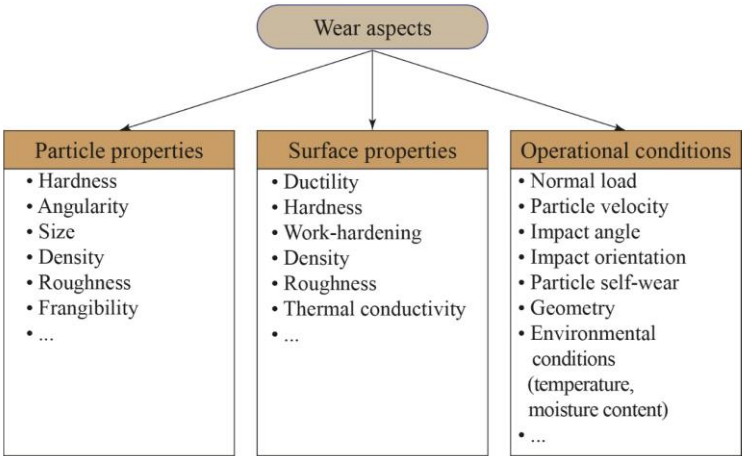

Figure 2.9 System characteristics for bulk handling

2.2.1 Particle properties

Particles as wear media refer to general material properties (e.g., hardness and roughness) and geometrical characteristics (e.g., size and angularity). As material science corresponding to microstructure exceeds the scope of this research, only particle hardness (which is one of the most significant parameters of deformation modelling), shape, and size, are considered in this study.

2.2.1.1 Particle hardness

Hardness means the ability of a surface resisting the deformations subjected to loads applied on an indenter [27]. The hardness of the particles involved in abrasion or erosion influences the rate of wear: particles with lower hardness than that of the surface cause less wear than harder particles. For particles significantly harder than the surface, then the exact value of their hardness matters less [21]. This behaviour is illustrated in Figure 2.10 which shows the relative wear rates in two-body abrasion of a wide range of metals and ceramics abraded by various types of grit particles [28]. From Figure 2.10, it can be seen that the wear rate becomes much more sensitive to the ratio of abrasive hardness H_a to the surface hardness H_s when H_a/H_s is less than 1.

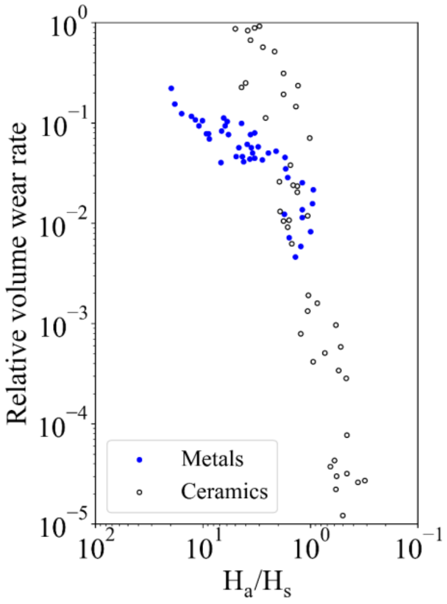

Figure 2.10 Relative volume wear rate plotted against the ratio of the hardness of the abrasive to that of the surface (H_a/H_s) for a range of metallic and ceramic materials and abrasive particle, for two-body abrasion, based on [28]

During indention of a spherical particle, an equipment surface deforms when the hardness ratio of abrasive particle to surface $H_a/H_s > 1.2$ [27], as shown in Figure 2.11 (a). If the hardness ratio $H_a/H_s < 1.2$, the particle deforms rather than the surface as shown in Figure 2.11 (b).

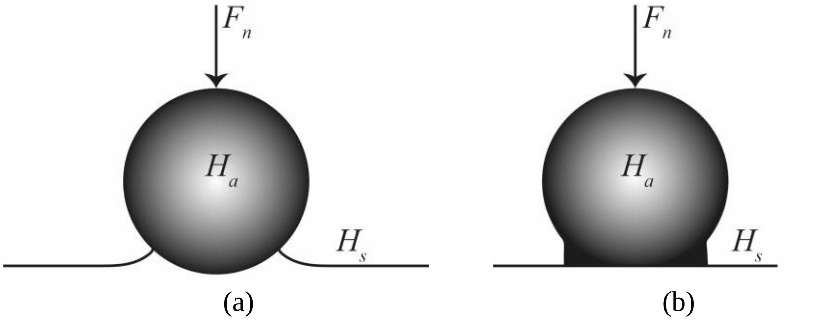

(a) (b)

Figure 2.11 Illustration of critical hardness ratio (a) $H_a/H_s > 1.2$, (b) $H_a/H_s < 1.2$, based on [27]

2.2.1.2 Particle angularity

Particle angularity affects the deformation of equipment surface and thus affects wear rate [29]. Wear rates depend strongly on the shape of particles, with angular particles causing greater wear than rounded particles. It has been confirmed by laboratory tests that increasing particle angularity leads to a significant increase in abrasive or impact wear rates [30]. Descriptors of particle visual appearance, such as “rounded”, “semi-angular” or “angular”, have been used to roughly classify and distinguish among various groups of abrasive particles [31–33]. Multiple attempts have been made to characterize abrasive particle shapes applying various conventional numerical descriptors. These descriptors correlate particle shape with its ability to abrade geometry. For example, L, I and S denote the longest, intermediate and smallest dimensions of a rectangular box containing exactly particles as shown in Figure 2.12, the following dimension ratios can be defined [34]:

Plainness = S/L, Elongation = I/L, Aspect ratio = S/I.

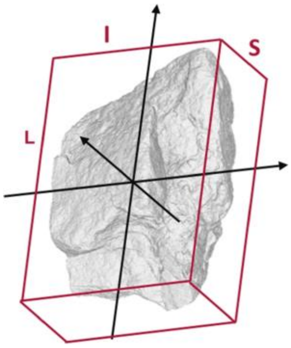

Figure 2.12 Characteristic lengths of a particle [34]

2.2.1.3 Particle size

The sizes of abrasive particles cover a wide range [21] from micrometre to centimetre. Regular-shaped particles can be accurately described by the given shape and a number of dimensions. However, no single physical dimension can adequately describe the size of an irregularly shaped particle, just as a single dimension cannot describe the shape of a cylinder, a cuboid or a cone [35]. The dimensions we use in principle depend on the following two perspectives:

1) What property or dimension of the particle we are able to measure;
2) The use to which the dimension is to be put. Some common diameters are used to express particle size, as shown in Figure 2.13 [35].

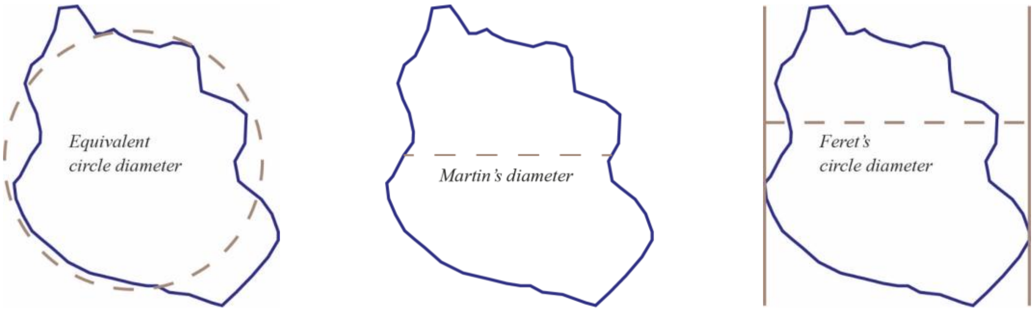

(a) (b) (c)

Figure 2.13 Illustration of parameters in particle characterizations (a) Equivalent circle diameter, (b) Martin's diameter, (c) Feret's diameter

Figure 2.14 shows the laboratory studies of both abrasive and impact wear of copper [36]. It should be noted that the ranges of particle size are chosen from around 10 µm to 125 µm with at least 3 intervals, and then the particle size is increased to 250 µm. It can be seen that wear rates for particles smaller than about 100 µm drop markedly with decreasing particle size. When particle size increases to 150 µm, wear rates reach nearly a constant. There are various explanations for this size effect [37,38]. The explanation of strain distribution appears to be the most convincing theory [39], which suggests the surface after abrasion will have a preferentially hardened layer of around 10 µm. Because of the layer near the surface, small particles are only able to influence this layer with high stress. However, sufficiently big particles can penetrate the hard layer and continue to plastically deform the material which is softer than that encountered by the small particles. Therefore, after some critical particle size, the influence of this hard layer on material deformation becomes slight.

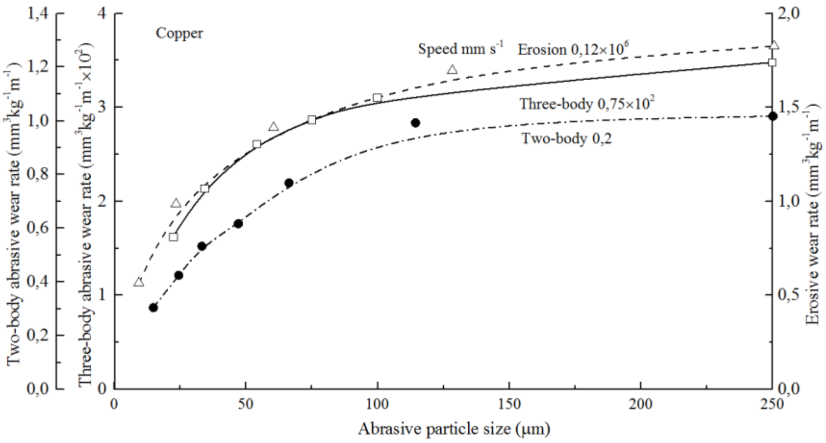

Figure 2.14 Wear rates of copper under conditions of erosion, two-body and three-body abrasion [36]

2.2.2 Surface properties

Surface properties reflect the material characteristics. As different materials display different deformation behaviour, it is essential to evaluate the ductility of the material. Besides, the deformation is directly associated with hardness ratio between particle and surface, so the surface hardness along with work hardening is considered.

2.2.2.1 Surface ductility

A solid will either be ductile or brittle depending upon the ratio of shear strength to tensile strength [40]. Surface ductility represents the ability of a structure to sustain large deformations in a plastic range without significant loss of resistance [41]. The surface materials of bulk solids handling equipment are assumed to be either ductile or brittle, and ductile and brittle surfaces suffer from different deformation mechanisms. A truly ductile material, for example pure copper, is unlikely to sustain a cleavage crack, but may fail by plastic instability. Some materials, like diamond and mica, apparently can undergo pure brittle cleavage with no discoverable plasticity [42].

When a rigid sphere and a plain ductile specimen are pressed against each other under increasing load, the contact is purely elastic initially. Then an elastoplastic area reaches which is a plastic zone surrounded by elastically deformed material. Finally, a full plastic zone exists. This process is shown in Figure 2.15 [43].

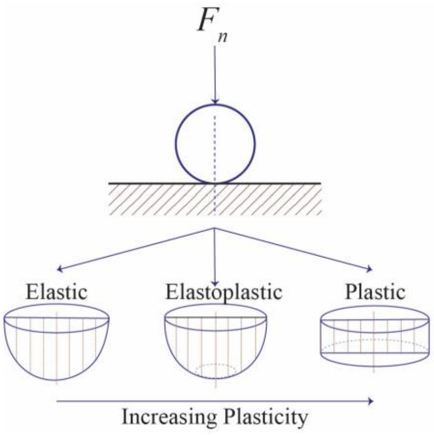

Figure 2.15 Schematic illustration for indentation of a sphere and a plain surface, based on [43]

Plastic deformation process has a substantial role in the overall wear process of ductile materials, but fracturing process has a major role in the wear process of brittle materials [44,45]. For brittle materials, the increasing load can result not only in elastic and plastic deformation but also in micro-cracking at and below the stressed surfaces [43]. Surface loading by a point indenter results in median and lateral cracks below the stressed surface [46]. The process of cracking formation during loading and unloading is shown in Figure 2.3. It should be noted that the shapes of indenters can significantly influence fracture generation and distribution [47].

2.2.2.2 Surface hardness

For abrasive wear (two-body abrasion and three-body abrasion) and impact wear, surface hardness has various influences on wear rate. Generally, it is considered that abrasive wear occurs when the ratio of abrasive particle hardness to the surface hardness is higher than 1.2. Specifically, different materials indicate different critical values. Figure 2.16 shows the experimental wear rate results when referring to a material with different matrices. It is obvious that two regions are observed: when the H_a/H_s ratio is less than 1.9 the increasing of abrasive hardness causes evident increase in wear rate. However, when the ratio is higher than 1.9, the increase in abrasive hardness in relation to material hardness has little effect on the wear rate [48]. Figure 2.16 also corresponds to three wear regions which are a small mild wear region (0.5-0.8), a mild-severe wear transition region (0.8-1.9), and a severe wear region (1.9-7.2).

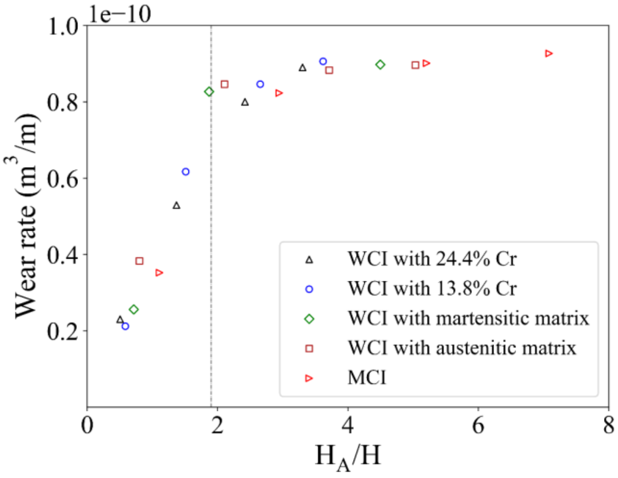

Figure 2.16 Relationship between wear rate and the ratio of the abrasive particle hardness (H_a) and surface hardness (H_s), based on [48]

In three-body abrasive wear the relation between wear rate and material hardness is more complicated than in two-body abrasive wear [49,50], because particles not only slide but also roll against surface. Sliding of particles can lead to micro-cutting, thus a cutting wear mechanism of three-body abrasion was formed [51]. Rolling of particles can cause craters because of plastic deformation and the corresponding plastic deformation was observed [52,53]. Based on the explanation above, micro-cutting and plastic deformation in three-body abrasive wear may coexist and the ratio between them can change with changes in operational conditions [49]. With increasing hardness of material, the wear rate decreases continuously but not decrease linearly. The wear decreasing rate becomes smaller in the range of higher hardness values, as shown in Figure 2.17 [50].

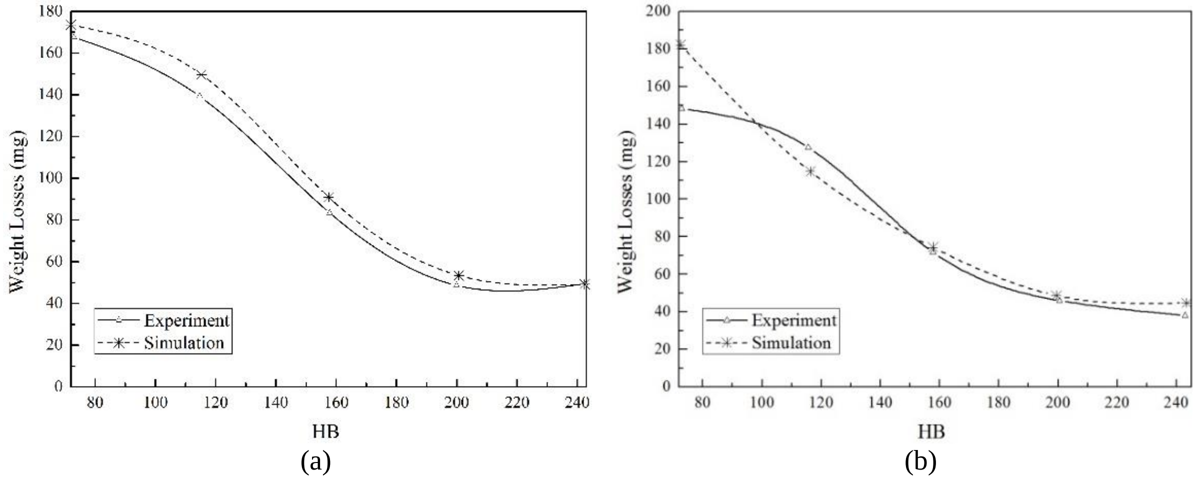

(a) (b)

Figure 2.17 Comparison of simulation and experimental results of various ring materials against (a) pure copper plate, (b) 0.8 % C steel plate [50]

2.2.2.3 Surface work-hardening

Work hardening also known as strain hardening, related to material properties, is a strengthening process led by plastic deformation [54]. In bulk handling conditions, equipment surfaces suffer from both erosive and abrasive wear, which will induce the phenomenon of work hardening [55]. Surface work-hardening increases the hardness of surface contacting with bulk solids and therefore decreases wear rate.

Several studies have revealed that the surface hardness after particle contact has better relationship than the original hardness with wear rate [56]. As shown in Figure 2.18, the surface material becomes heavily work-hardened by particle impacts, which can be reflected in the difference between the two sets of hardness values. The impact wear has stronger relation with the work-hardened hardness (solid line) of the surface rather than to the annealed hardness (dashed line) of the surface [56]. Therefore, the work-hardened hardness should be used when refereeing to a relation with wear rate.

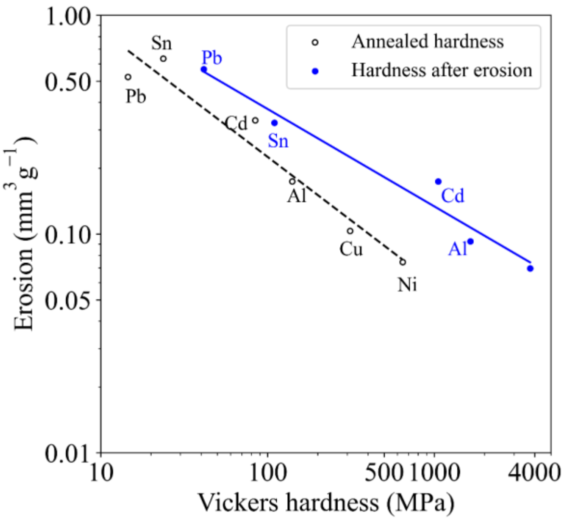

Figure 2.18 Volume erosion for a number of metals as a function of Vickers hardness of the annealed surface and of the eroded surface, based on [56]

2.2.3 Operational conditions

Operational conditions involve bulk flow and environmental effects. This study focuses on the effect of particle flow behaviour on wear and the environmental factors exceed the scope of this research.

2.2.3.1 Normal load

For abrasive wear, it is generally observed that mass loss (wear rate) increases with applied load [57], as an example shown in Figure 2.19. It also indicates that the wear rate for each material appears to be independent of particle size at the highest load. At high load, when particles become more deeply embedded in spacemen, cutting may become more significant and result in a high increase of wear rate. This phenomenon is consistent with the explanation of surface work-hardening.

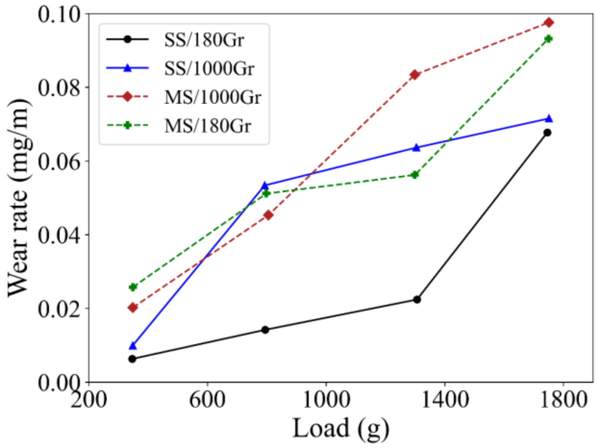

Figure 2.19 Wear rate against applied load for three-body abrasion wear, based on [57]

2.2.3.2 Particle velocity

Particle velocity plays a significant effect on impact wear. One theoretical feature predicts that the erosive wear should depend on the cube of the impact velocity. Experimental works reported that velocity exponents for the erosion of metals at normal incidence tend in general to be higher than the values of 2.3-2.4 commonly found in low angle erosion experiments [58], as shown in Figure 2.20 [21].

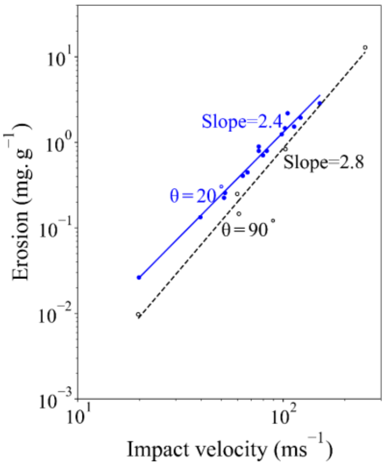

Figure 2.20 Measurement of erosion rate of copper, based on [21]

Table 2.1 lists the velocity exponents corresponding to different metal materials at normal incidence. It is noteworthy that values of around 3 are often found for impact wear by both angular and spherical particles at normal incidence [59]. As impact wear normally refers to high impact velocity (e.g., > 20 m/s), it can be justified that the impact wear is excluded in this research as the particle velocity in this study is constrained below 2 m/s.

Table 2.1 Velocity exponents reported in normal impact erosion [59]

Material	Abrasive material	Velocity exponent
Cu, OFHC	82 µm SiC grit	3.0
Cu, OFHC	Various grits	2.8
Steel, 11 % Cr	13882 µm glass spheres	3.4
Al 1100 - 0	250 µm SiC grit	2.9
Al, 99.9 %	1.58 mm WC spheres	3.3
Al alloy	138 µm glass spheres	2.4
Al	430 µm steel spheres	2.5
Al 6061-T6	550 µm glass spheres	3.0
	230 µm glass spheres	2.3
	650 µm glass spheres	3.3

2.2.3.3 Impact angle

The geometry of the deformation due to the impact of a hard particle depends on the impact velocity, on the shape and orientation of the particle, and on the impact angle. Impact angles in erosion are usually defined relative to the plane of the surface, as shown in Figure 2.21 [21].

For brittle materials (e.g., glass and graphite) attacked by aluminium particles (297 µm) at a velocity of 96 m/s and by glass spheres (475 µm) at a velocity of 108 m/s [23], impact wear rate of brittle materials increases with the increase of impact angle, as shown in Figure 2.21 (curve b). In brittle materials, material will be removed by the intersection of cracks which initializes from the point of impact of the eroding particles [23]. Ductile materials undergo mass loss by a process of plastic deformation in which material is removed by the displacing or cutting action of the successive impacting particle.

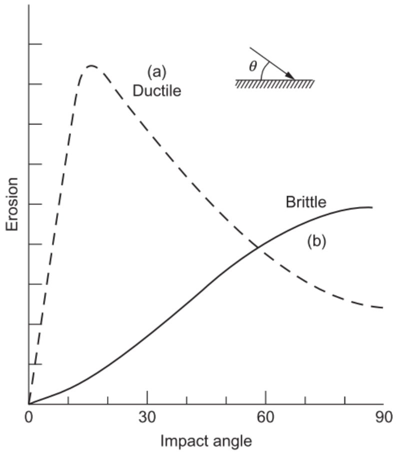

Figure 2.21 Typical dependence of erosion on impact angle [23]

2.2.3.4 Impact orientation

It is possible that rotation of particles may affect the erosion rate and even the erosion mechanisms when the particles strike a target surface. A variable termed as 'rake angle' which shows the orientation of the particle relative to the surface at the impact point is proposed [60]. Figure 2.22 shows how an angular particle impacts at a range of rake angles and how the rake angle is defined [60]. The rake angle as defined in Figure 2.22 varies associated with particle orientation, and the impact of spherical particles is a special situation equivalent to that of angular particles with a zero rake angle [61]. It is argued that the nature of the impact deformation depends strongly on this angle.

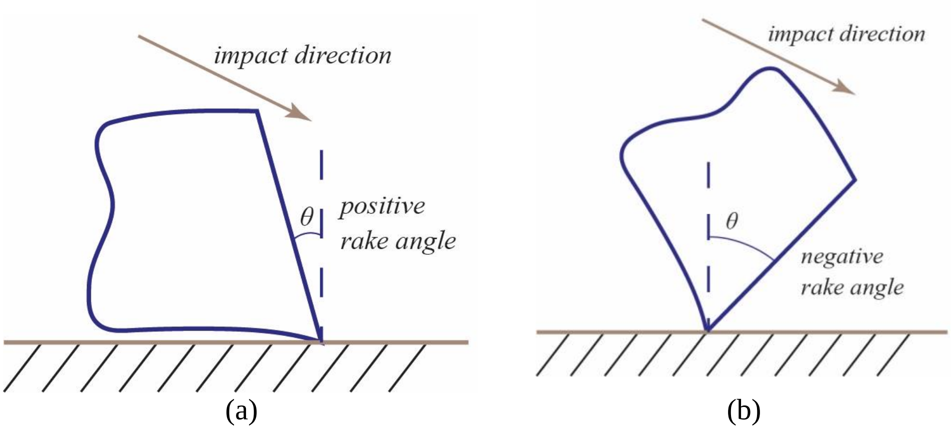

(a) (b)

Figure 2.22 A particle striking a surface at different orientations (a) positive rake angle, (b) negative rake angle, based on [43]

Studies of the impact of single particle on metals show three basic types of impact damage [62,63] shown in Figure 2.7. Figure 2.23 illustrates two spherical particles with contrasting spin directions striking a target [61]. Rounded particles deform the surface by ploughing, displacing material to the side and in front of the particle [61].

The particles with backward spin have an effective contact velocity higher than the impact velocity. For ductile materials, it might be expected that the shear force applied by the particle would increase as a result of an increasing contact velocity [61]. This in turn results in more material being displaced from under the particle to the front of the crater during impact, generating a larger lip. On the other hand, the spherical particles with top spin have a lower effective contact velocity than the impact velocity. The forward momentum of the particle means that it tends to roll on the target surface resulting in little surface deformation and small lips [61]. Further impacts on neighboring areas lead to the detachment of heavily-strained material from the rim of the crater or from the lip at its end.

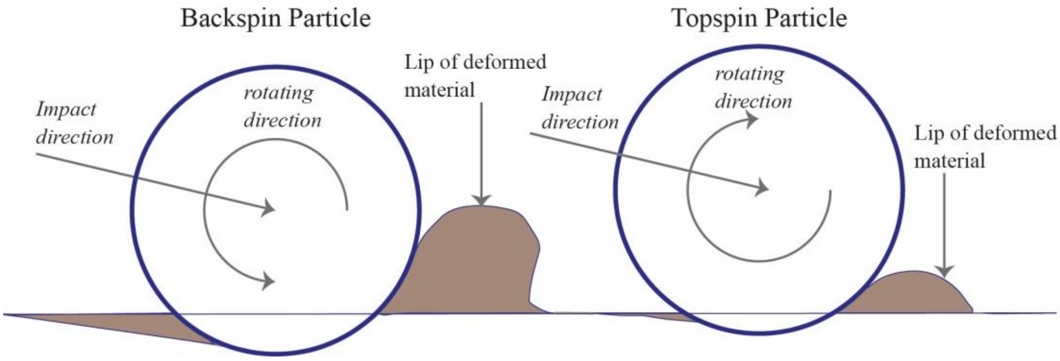

Figure 2.23 Illustration of spinning spherical particles with a target surface, based on [61]

Similarly, the deformation caused by an angular particle depends on the orientation of the particle as it strikes the surface, and on whether the particle rolls forwards or backwards during contact. In the mode which is termed type I cutting (Figure 2.7 (b)), the particle rolls forwards, indenting the surface and raising material into a prominent lip, which is vulnerable to removal by subsequent nearby impacts. If the particle rolls backwards, a true machining action can occur, in which the sharp corner of the abrasive grain cuts a chip from the surface, and this mode is termed type II cutting. This mode occurs over only a narrow range of impact angles and orientations [63]. Based on these mechanisms, the direction of rotation of a particle should be considered into surface deformation [61].

As is clear from Figure 2.24, backward spin of the angular particles increases the effective impact velocity and decreases the effective impact angle. This might be expected to result in an increase in impact wear rate, particularly at angles larger than that corresponding to the peak erosion rate which is a peak at angles between 0° and 90°.

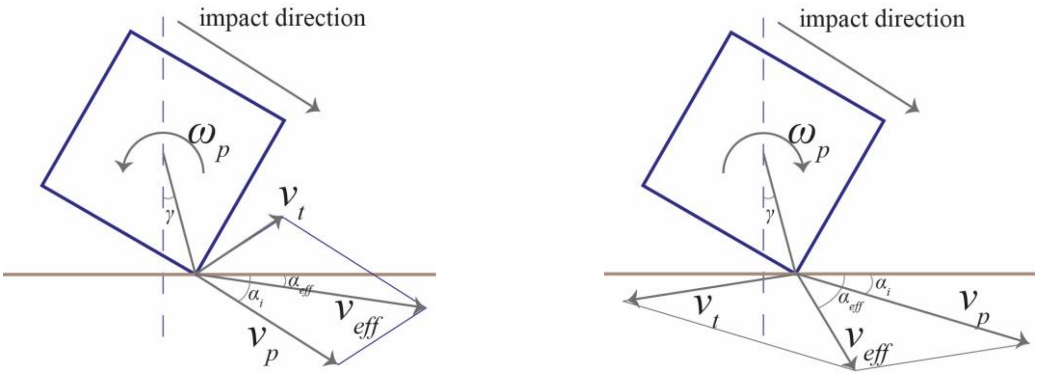

(a) (b)

Figure 2.24 Schematic diagram indicating the velocity vectors associated with spinning angular particles impacting a surface (a) particle with back-spin, (b) particle with top-spin, based on [61]

Figure 2.25 Finnie [64] developed an erosion model for ductile metals which was based on an analysis of the mechanisms of kinetic energy exchange during the impact of a single solid particle where cutting was the predominant mechanism. This model was later modified by Bitter [23,24], who incorporated the effect of deformation wear acting in conjunction with cutting wear. A modified Finnie-Bitter model is predicted by impact wear experiments shown in Figure 2.25. The results are for the wear of a steel target by crushed glass abrasive material (150 µm – 250 µm). It should be noted that the rake angle in the predicted model is 0° which means the particle can be considered as spherical. The lines shown in Figure 2.25 indicate the predictions of the model for the three possible modes of particle spin: top-spin, back-spin and non-spinning particles. The predictive model presents generally good agreement with the experimental data over a wide range of impact angles. The effect on erosion depends on the direction of spin, and the results indicate a higher erosion rate if particles strike the target with “back-spin” rather than “top-spin” or “no-spin” [61].

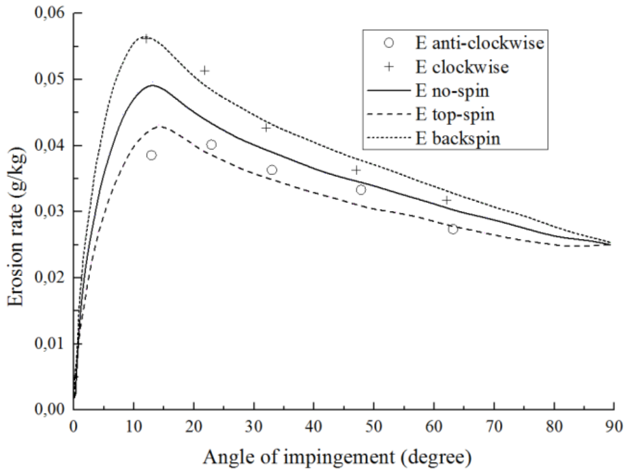

Figure 2.25 Experimental data and predictions of the modified Finnie-Bitter erosion model [61]

During bulk handling process, three aspects including particle properties, surface characteristics, and operational conditions determine the wear mechanisms. Abrasive and impact wear are the two principal wear mechanisms occurring on bulk handling equipment. For each mechanism, multiple wear modes coexist, such as cutting, plastic deformation, and cracking, resulting in different formation of surface deformation. Figure 2.26 gives an overview of system characteristics and wear mechanisms of surface deformation during bulk handling.

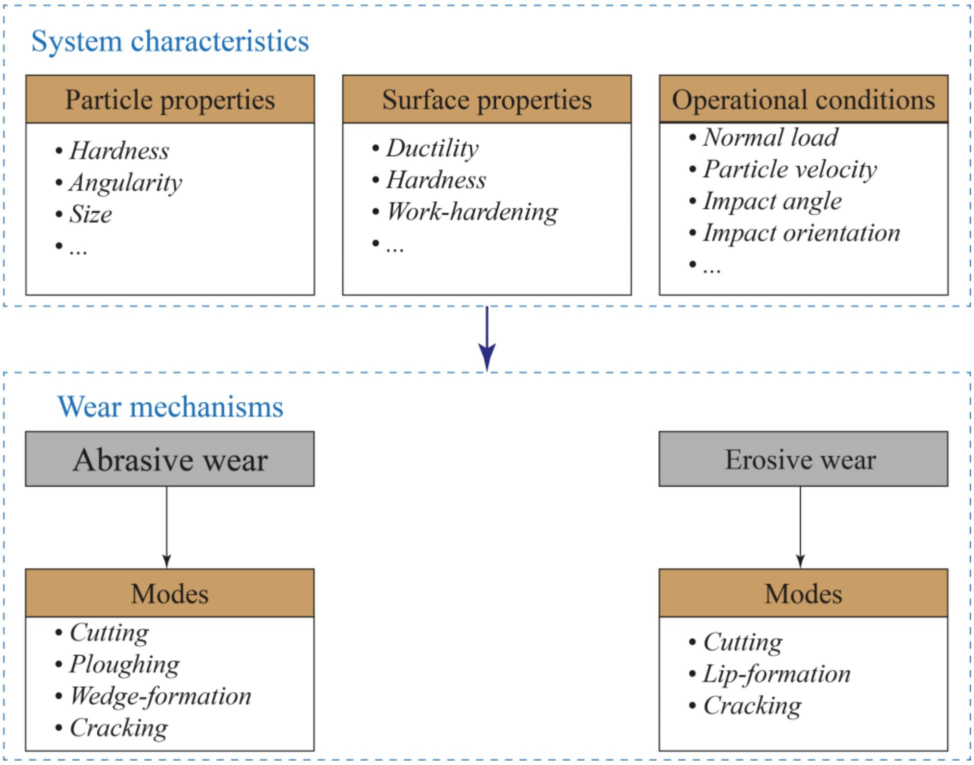

Figure 2.26 Schematic relating to surface deformation during bulk handling

2.3 Numerical modelling for surface deformation caused by bulk material

The modelling of wear on bulk solids handling equipment refers to two parts: bulk material and surface deformation of surface. For the modelling of bulk material, discrete element method

(DEM) has been successfully used by researchers and engineers to design, analyze and optimize bulk material handling systems and equipment for granular materials [65,66]. DEM is used in different fields ranging from mining [67,68] to agriculture [69,70], and geotechnical applications [71].

For the modelling of surface deformation, numerical methods categorized in Figure 2.27, such as finite element method (FEM), smoothed particle hydrodynamics (SPH), and discrete element method (DEM), have been implemented in a wide field of research. Below evaluates seven numerical methods and the most suitable one for surface deformation due to bulk material is selected.

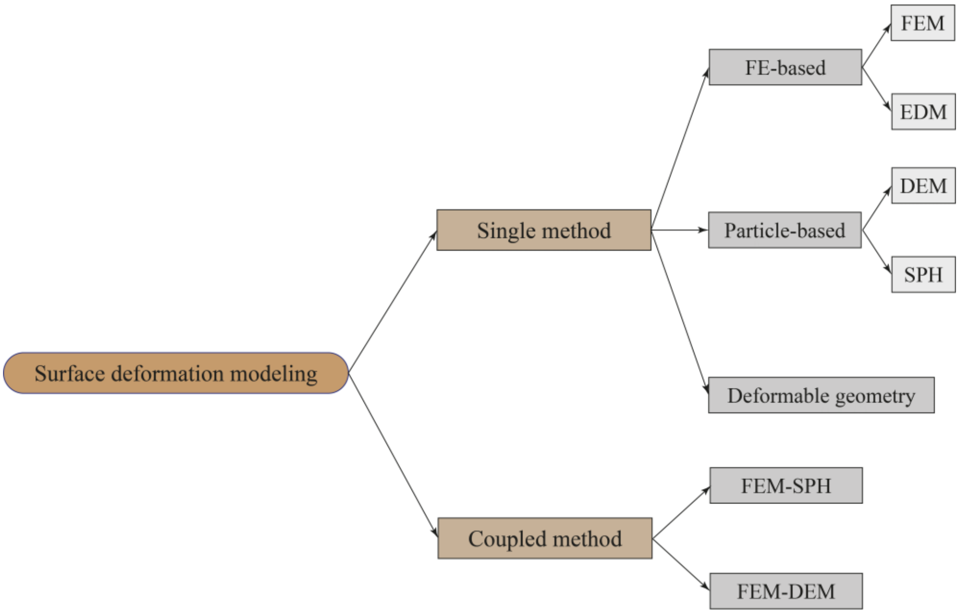

Figure 2.27 Numerical methods for surface deformation

2.3.1 Finite element method

Finite element method (FEM) is one of the most used methods [72] for simulating the process of sliding wear [73–75], impact wear [76,77], fretting wear [78,79], and cracking generation and propagation [80–82]. FEM computes the stress-strain field by discretizing a continuum geometry into a finite number of elements assembled at nodes. Therefore, the deformation due to wear is calculated by determining the stress-strain correlation associated with a wear model [83].

Figure 2.28 shows the process of fretting wear damage modelled by FEM [80]. The fretting wear occurs when small relative oscillatory movements appear between two bodies in contact [84]. During this simulation, the coordinates of nodes in an expanded region under the contact surface are updated by interpolating the current damage field to a new position. However, the calculation convergence tends to fail when referring to multiple layers of meshes.

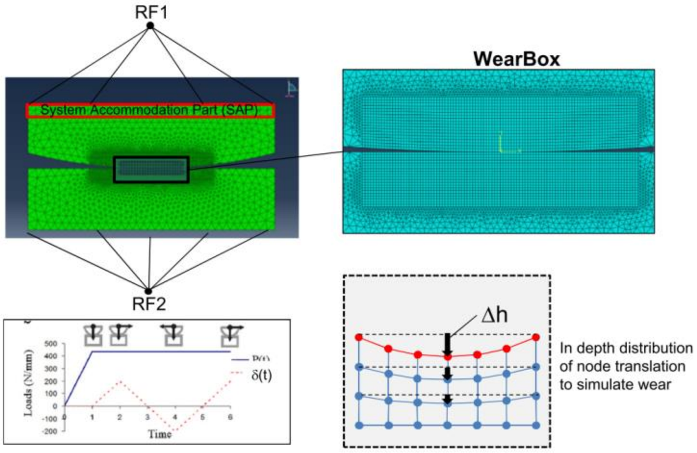

Figure 2.28 Illustration of the progressive node translation strategy [80]

To overcome the element distortion problem, adaptive remeshing techniques have been suggested. One adaptive remeshing technique, depicted in Figure 2.29, can be divided into four main steps: (1) development of a representative three-dimensional finite-element model; (2) calculation of the effective stress intensity factors along the crack front; (3) determination of the crack front advances applying an adequate fatigue crack growth law; (4) definition of a new three-dimensional finite-element model incorporating the new crack front. For wear modelling and simulation, user defined subroutines based on adaptive meshing technique are applied to adjust the contact nodes in order to adapt the mesh to the evolving geometries [85–87]. When referring to big deformation in comparison with mesh size, the adaptive remeshing technique can be a proper option to avoid mesh distortion.

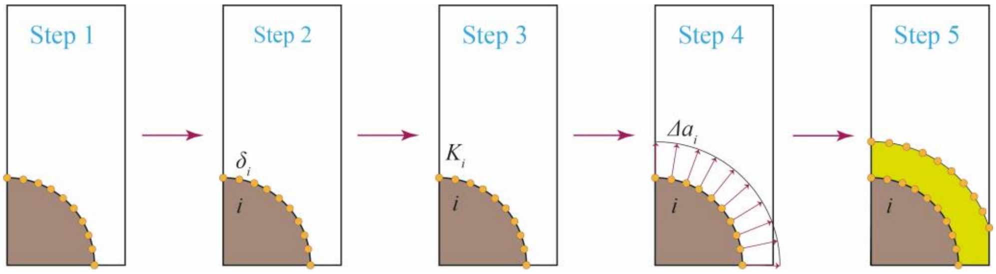

Figure 2.29 Adaptive remeshing technique, based on [81]

2.3.2 Element deletion method

The element deletion method (EDM) is on the basis of finite element method. In the element deletion method, elements are removed when the necessary conditions, such as the critical stress-strain relationship, is met during the deformation. The element deletion method has the advantage to overcome the stress concentration at cracked surface by deleting the corresponding elements. However, it might induce physical inaccuracy as the material removal is dependent on element size and results in non-smooth profile [88,89].

Figure 2.30 shows the mechanism of the element deletion method. First, valid fracture criteria are needed for determining those elements deleted. Second, implementation of element deletion and preparation for disconnected node removal are necessary. Third, rearrangement of the boundary conditions after the element deletion. Since some elements might be deleted depending on the level of critical damage factor of each fracture criterion, the new boundary surface would be generated.

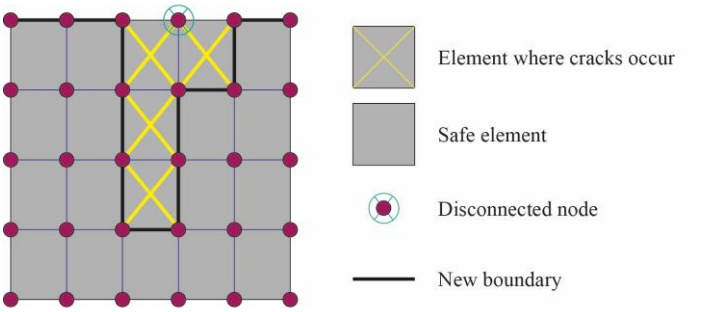

Figure 2.30 Schematic diagram of the element deletion method, based on [88]

2.3.3 Discrete element method

Simulation of non-continuous phenomena like fracturing is not well adapted to a continuous description. A bonded particle model based on Timoshenko theory [90] offers the possibility to simulate the deformation of materials, such as abrasive wear [91,92], elastic deformation [93], rock cutting and polishing [94–96], and fracture and damage during machining process [97]. In this case, the DEM is an alternative because it naturally takes into account discontinuities [93].

The bonding contact model was used to bond particles with a finite-sized “glue” bond, as shown in Figure 2.31 [98]. If the contact radii of two particles overlap during the bond formation time, these two particles will be bonded together. When the particles no longer overlap the bond is lost [91], and therefore individual elements are leaving the surface object.

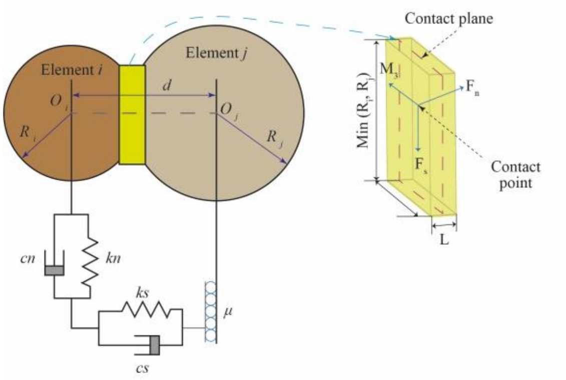

Figure 2.31 Illustration of inter-element contact constitutive model, based on [98]

As the DEM essentially takes most of discontinuities into account, the material failure characterized with multiple fracturing and cracking makes it a suitable tool to study rock cutting [99–102]. Typically, a cutting tool is treated as a rigid object and the rocks are built by assembling discrete particles with a specific contact model [99,103,104].

Inspired by the advantage of the DEM on the modelling of material failure, a cutting tool is discretized with solid particles to represent the continuous geometry. The shape of the tool is changed by eliminating particles if the accumulated wear exceeds the particle size [100]. Figure 2.33 illustrates a rock cutting process with a pick of dredge cutter head in 2D. From Figure 2.33 (d) it can be seen that the shape of the cutter head changes due to the removal of particles.

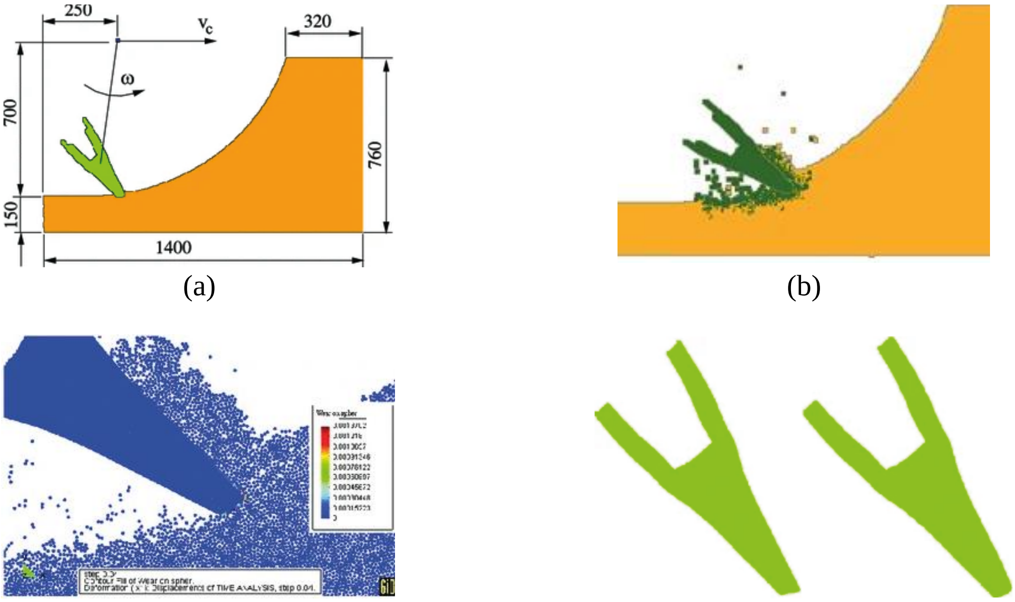

(a) (b)

(c) (d)

Figure 2.32 Modelling of rock cutting with a dredge cutter header (a) model settings for rock cutting, (b) thermomechanical simulation of rock cutting, (c) accumulated wear on the tool surface, (d) change of the tool shape due to wear [100]

As the discretized geometry based on individual particles leads to non-smooth surface and influences the contact behaviour with particles, quantifying the wear loss brings relatively high error.

2.3.4 Smoothed particle hydrodynamics

Smoothed particle hydrodynamics (SPH) which is a particle-based method for continuum mechanics may have significant advantages over FEM for the simulation of surface deformation because it does not involve the use of elements which can deform, tangle, and distort [105]. Similar with FEM, the deformation occurs when a fracture criterion is met governed by the stress-strain response of a proposed constitutive mode [106].

SPH is a mesh-free numerical technique, in which particles without fixed connectivity are used to discretize the problem domain. The SPH particles carry material properties and can move relative to each other according to the governing conservation equations, as shown in Figure 2.33. The computation domain is discretized by an amount of mass points and each point occupies independent domain and mass. Thus, the mesh tangling and element distortion problems encountered in large deformation problems with grid-based finite element methods can be avoided [105]. However, many researchers evaluated the SPH method on numerical aspects and identified several challenges, such as low accuracy, modelling stability, convergence and efficiency issues, in comparison with FEM [107].

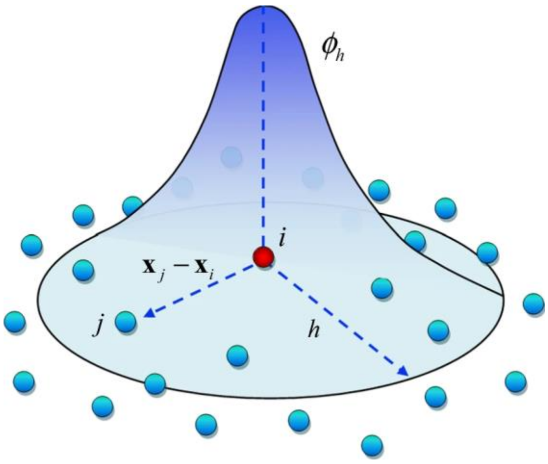

Figure 2.33 Schematic illustration of a SPH smoothing kernel function
in a three-dimensional case [108]

As a particle or grid/mesh free method, SPH is an ideal tool to model free surface and interfacial flow problems as the connectivity between particles are updated as part of the computation [107]. For fracture generation, SPH can be applied to modelling the failure of discontinuous solids, such as rock and concrete [106,109], and the plastic and crack propagation of continuous structure, such as a shell deformation [110], dynamic deformation of a beam and crack formation of a cylinder [111,112], and metal cutting process [113]. For surface deformation, SPH is also an alternative when refers to large deformation, such as impact wear caused by particle impact [114,115] and abrasive wear [116] due to the relative sliding of a counterpart.

2.3.5 DEM with deformable geometry technique (DEM-DG)

DEM method combined with a deformable geometry technique provides a new option for modelling of surface deformation. Successful applications include prediction of wear rate of a steel plate [117], material loss at soil tillage via scratch test [118], and wear profile update of an industrial vertical stirred mill screw liner [119]. In this method, the meshed geometry is imported into DEM environment and only the surface layer of the object is meshed. Therefore, the computational demand is significantly lower compared to FEM. The procedure of this method is illustrated in Figure 2.34.

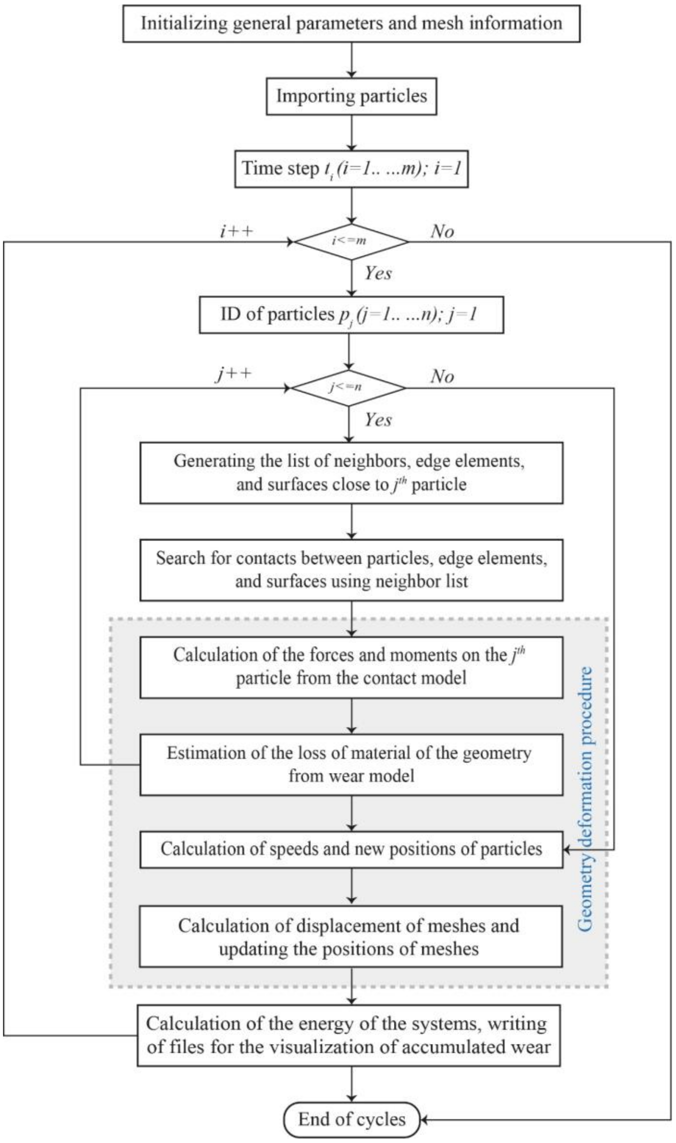

Figure 2.34 Flow chart of DEM with geometry deformation technique

The highlighted part demonstrates the process of calculating wear volume and updating the mesh deformation of the geometry. First, the contact between the particle and the surface elements is detected and the forces are calculated based on the contact model. Second, the loss of the material is evaluated based on the wear model. Third, the new positions of the elements and velocity of the particle are recalculated. Fourth, the element is displaced in normal direction. Therefore, the representation of the wear loss is performed by deforming the meshes subjected to abrasive wear.

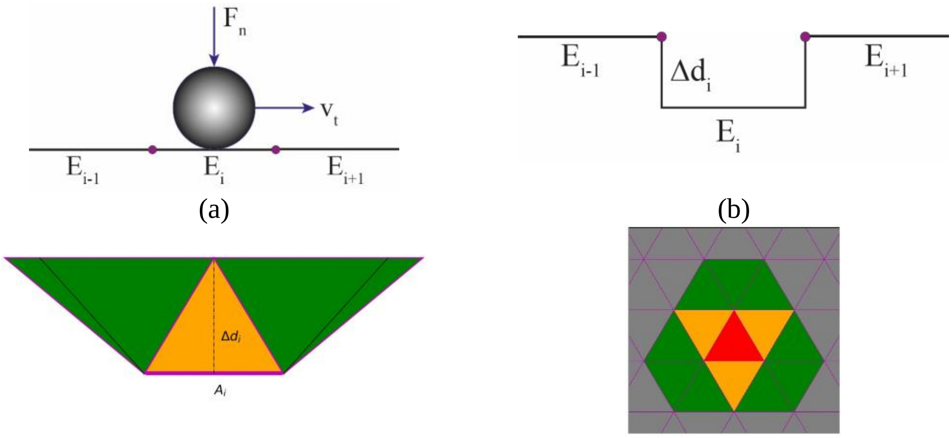

(a) (b)

(c) (d)

Figure 2.35 Mesh deformation procedure (a) particle in contact with the surface E_i of the mesh element, (b) displacement of the mesh element, (c) side view of the interconnection between nodes, and (d) top view of the wear representation, based on [117]

2.3.6 Coupled methods for surface deformation

Individual methods have disadvantages as mentioned above, for example the mesh distortion issue for FEM and high computational cost for DEM. Two methods coupled together has potential to discard the disadvantages and combine the advantage of individual methods.

2.3.6.1 FEM-SPH coupled method

For FEM, the meshes may be distorted during large deformation as mentioned before. For mesh-free method, such as SPH, there is no mesh tangling problems but time consuming. Shown in Figure 2.36, the impacted area [114] or abraded area [116] is modelled by the SPH, while the other section with less deformation uses FE discretization. The results obtained from this coupled method include surface morphology and wear rate which are comparable to the experimental results. However, the weakness of the method is similar with SPH as explained in Section 2.3.4, such as stability issue and low accuracy.

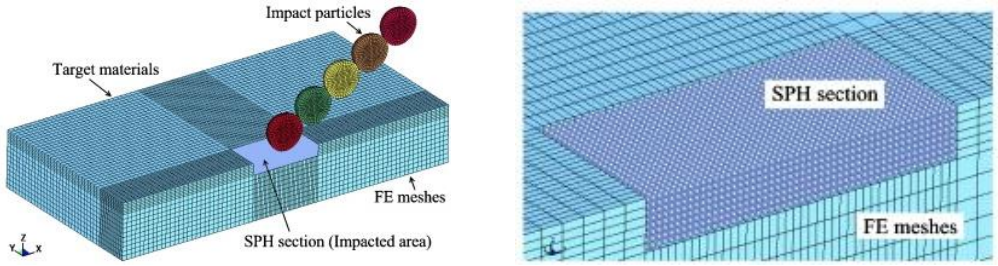

(a) (b)

Figure 2.36 Numerical model of impact wear at 30° impact angle (a) FE mesh section, (b) SPH section at centre of the target material [114]

2.3.6.2 FEM-DEM coupled method

The DEM is a suitable method to model materials with discontinuities and material failure characterized with fracture. The FEM is usually a method when involving continuous material behaviour. As complementary methods to each other, FEM and DEM coupled method takes advantages of each method [120–122]. The coupled finite-discrete element methods allows us to create multiscale models where material models at different levels are employed in different subdomains of the same body [120].

Figure 2.37 illustrates a multiscale discrete-finite element model. The DEM and FEM subdomains overlap each other, so a transitory zone between the two domains is formed. In this zone the contributions of each of the two methods to the overall stiffness vary gradually to minimize unrealistic wave reflections at the interface between the DEM and FEM subdomains [123].

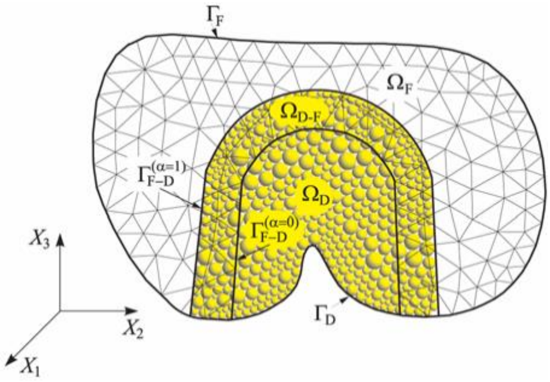

Figure 2.37 Multiscale discrete-finite element model [120]

To cut the computation cost of the pure DEM simulation, the rock cutting process can be modelled by combining the DEM with the FEM in such a way that the discrete elements are used only in a portion of the analysed domain where material fracture occurs, while finite elements are used outside the DEM subdomain [122]. Figure 2.38 shows similar failures of rock during cutting using DEM and DEM/FEM coupled models. This indicates that the coupled model gives similar results to the DEM model while improving the computation efficiency.

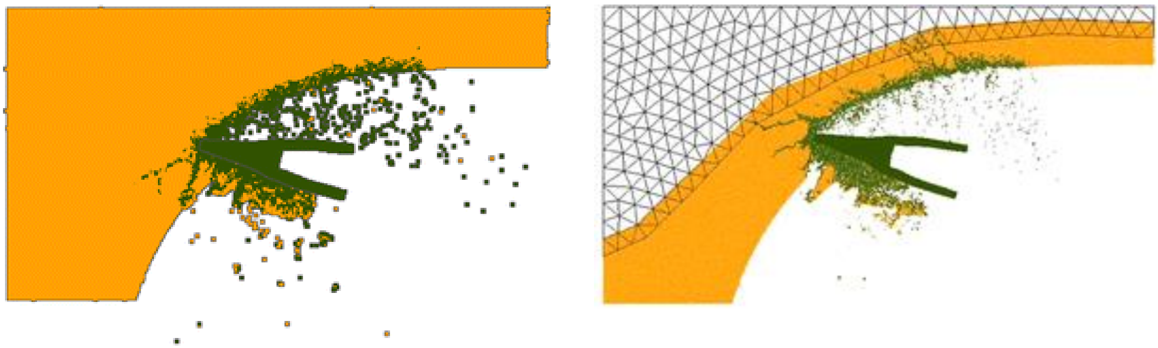

(a) (b)

Figure 2.38 Simulation with rock cutting [122]
(a) DEM model, (b) DEM/FEM model

2.3.7 Evaluation of numerical methods for surface deformation

As the surface deformation is caused by the contact with bulk material, the numerical methods should be capable to model the interaction between bulk material and surface accurately and efficiently. For the accuracy, the surface is assumed to be smooth in terms of roughness and continuous with respect to material characteristics. For the efficiency, the computational demand is evaluated as the numerical model refers to bulk material.

The traditional FE-based methods, FEM and EDM, complete material removal by detecting if a critical value governed by a stress-strain equation is met. This detection procedure is computationally expensive as an extra technique is normally required to re-mesh the geometry to avoid the element distortion problem. Besides, this method is typically applies to single interaction.

Both DEM and SPH are a particle-based method which means the object is discretized by particles, leading to an unsmooth surface. Besides, DEM is costly as it requires a large amount of small particles to mimic a relative smooth surface. SPH, which is a particle-based method for continuum mechanics, solves the stress-strain equation to determine surface deformation and therefore leads to high computational cost similar with FEM.

FEM-SPH and FEM-DEM coupled methods combine the advantages of two individual methods and improve the computational expense because a subdomain is discretized with particles. The subdomain is represented by particles and therefore is unsmooth.

The DEM combined with deformable geometry technique is selected to model the surface deformation. In comparison with other methods, first, the surface is discretized with elements rather than individual particles, so it is smooth and continuous. Second, this method allows the material removal in a form of plastic deformation based on a specific wear model by efficiently solving a force-displacement relationship derived from the bulk-surface contact in DEM.

2.4 Conclusions

This chapter addresses the question:

What are the main wear mechanisms and what is a suitable numerical method for wear modelling with respect to bulk handling process?

Wear occurs as a result of interaction between particles and geometry during the bulk handling process. Two main wear mechanisms are abrasive wear and impact wear. Each of the wear mechanisms contains multiple wear modes depending on the three system characteristics, namely particle properties, surface properties, and operational conditions. The wear modes for the abrasive wear consist of micro-cutting, micro-ploughing, and wedge formation, while the impact wear deforms surface by micro-cutting and lip formation associated with the impact angle of particles.

The selection of the numerical model refers to bulk material and surface deformation. Multiple numerical methods including coupled methods are evaluated on the modelling of surface deformation caused by bulk material. By comparing the numerical methods, the DEM with deformable geometry technique has the advantage to integrate bulk material and surface deformation effectively and accurately.

Chapter 3 and 4 elaborate the wear mechanisms of the convex pattern surface on wear reduction with non-deformable geometry. Chapter 5 and 6 model the surface deformation caused by a single particle and bulk solids using the deformable geometry technique.

3 Optimization of a convex pattern surface based on DSD*

To reduce the sliding wear of a transfer chute, a bio-inspired convex pattern surface is proposed in a previous study. Continuously, this chapter optimizes the surface based on a definitive screening design (DSD) approach and discrete element method (DEM). An optimal sample with lowest wear rate compared to a reference plain sample is obtained. The structure of this chapter is as follows. Section 3.2 demonstrates the contact model and wear model applied to this study. Section 3.3 calibrates two critical parameters between particles based on two laboratory tests. Section 3.4 designs experiments and develops the results analysis procedure. Section 3.5 evaluates numerical results and identifies two flow regimes. Section 3.6 draws main conclusions.

---

*This chapter is based on Yan, Y., Helmons, R., Wheeler, C., & Schott, D. (2021). Optimization of a convex pattern surface for sliding wear reduction based on a definitive screening design and discrete element method. Powder Technology, 394, 1094-1110. https://doi.org/10.1016/j.powtec.2021.09.041.

3.1 Introduction

Bulk solids handling plays a significant role in a range of industries, such as the mining, agricultural, chemical, and pharmacology industries [1]. For the mining industry, the process of transferring bulk solids, e.g. iron ore, leads to surface wear of handling equipment. Two principal wear mechanisms can be distinguished: abrasive wear and erosive (impact) wear [3,4]. Studies show that approximately 82 % of the energy loss is attributed to the bulk material sliding along the chute bottom and 9 % of the losses due to sliding against the side walls [6]. Severe wear has been found in several locations on bulk handling equipment, for example, silo walls and transfer chute bottom sections [6,7]. Wear leads to surface deformation and volume loss of handling equipment and accelerates the damage of the equipment, resulting in a reduction of lifespan. The maintenance of wear areas is costly and generally increases downtime. To save costs and reduce downtime, the surface wear of bulk solids handling equipment must be reduced.

Traditional methods to reduce surface wear of bulk solids handling equipment rely on five aspects [16]: (1) optimizing operational conditions based on theoretical wear models [6,9]; (2) using wear-resistant materials with coating technologies [124]; (3) supplying a repulsive force to diminish the contact force between particulate solids and equipment [1]; (4) adding assistant components by using the self-wear mechanism of the bulk solids [124]; and (5) fabricating a surface geometry pattern to affect the kinematics of the bulk material flowing along the surface [12,125]. In this research, a geometry pattern equipped on a smooth surface is studied based on a bionic design [5]. Scientists have discovered several surface morphologies [126–128] that can achieve lower wear rates compared to smooth surfaces [129–131], and recently a convex pattern surface was introduced to reduce the sliding wear of transfer chutes [132,133]. However, the effects of geometrical parameters of a convex pattern and operational conditions, such as bulk velocity and particle bed height, on the sliding wear, are still uncertain.

This paper aims at optimizing a convex pattern surface for sliding wear reduction through the discrete element method (DEM). First, the critical factors of the convex pattern and the selected operational conditions are sorted out based on a definitive screening design (DSD). Second, the relationship between the bulk flow regimes and the factors is investigated. Third, the mechanisms of the sliding wear reduction are elaborated based on the contact behaviour between particles and samples.

3.2 Discrete element method

3.2.1 DEM contact model

Discrete element method (DEM) is developed by Cundall and Strack [134] to model particle systems by tracking the movement of each particle and interaction with its surroundings over time. DEM is the most attractive computational method used by researchers and engineers to successfully design, analyze, and optimize bulk materials handling systems and equipment for granular materials [135,136]. In this study, a DEM software package EDEM [137] is used.

The motion of discrete particles in DEM is governed by Newton’s second law of motion [135]. The Hertz-Mindlin no-slip contact model is a nonlinear elastic contact model [138] which is appropriate for non-cohesive granular materials. Figure 3.1 illustrates the contact between two particles. This contact consists of two springs, two dampers, and a slider. The springs are used to represent particle stiffness in normal and tangential directions. Two dampers are used to model the damping forces, and the slider is applied to generate a friction force. The normal force F_n is calculated according to Equation (3.1), where S_n, δ_n, D_n, and v_n are the stiffness, overlap, coefficient of damping force, and velocity in the normal direction of the contact, respectively.

$$F_n = -\frac{2}{3} S_n \delta_n^{1/2} + D_n v_n \tag{3.1}$$

The tangential force F_t is restrained by Coulomb law [139], which is expressed by Equation (3.2), where μ_{st} is the coefficient of static friction; S_t, δ_t, D_t, and v_t are the stiffness, overlap, coefficient of damping force, and velocity in the tangential direction of the contact, respectively.

$$F_t = \min\left\{-S_t\delta_t + D_t v_t, \mu_{st} F_n\right\} \tag{3.2}$$

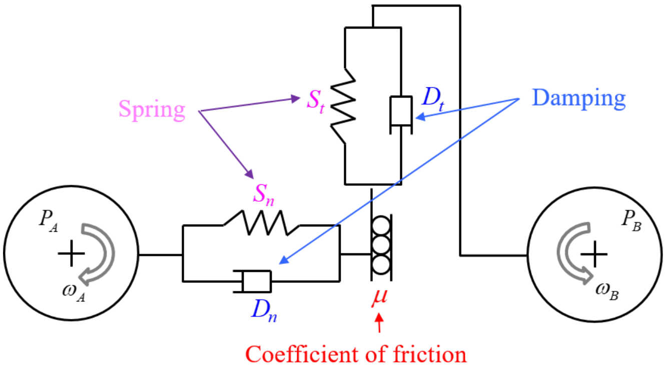

Figure 3.1 Illustration of contact between two particles

Spherical particles are normally used in DEM for simulation of non-spherical particles, since DEM is an expensive technique for modeling particulate systems at the individual particle scale [140]. In this study we use spherical particles based on findings of previous studies. These have shown that using spherical particles can reach a good agreement with experimental results. For example, Esteves et al. [119] compared a vertical stirred mills screw liner wear (wear profile and wear volume) after more than 3000 hours test with simulation results (spherical particles and Archard wear model). For other applications, such as ball mill liner wear, spherical particles were used to predict the wear of mill based on DEM simulations [141–143].

The non-spherical particle shape is accounted for by the use of a rolling friction model [144,145]. A review of rolling friction identified four different classes of rolling resistance models that are commonly used in DEM [146]. In this study, rolling type A is chosen because it is effective for modeling small scale systems such as sand-pile formation and can also be used for rolling energy dissipation in a dynamic scenario if the adopted computational time step is sufficiently small [146]. Type A applies a constant torque on a particle to represent rolling friction, and the direction of the torque occurs always against the relative rotation between two contact entities. This mechanism can also be applied to the contact between particles. A typical model of rolling model Type A by Zhou [147] is expressed by Equation (3.3)

$$M_r = -\frac{\omega_{rel}}{|\omega_{rel}|}\mu_r R_r F_n \qquad (a)$$

$$\omega_{rel} = \omega_i - \omega_j \qquad (b) \tag{3.3}$$

where M_r is the torque between two in-contact disks i and j. ω_i and ω_j are the angular velocities of particles i and j, respectively, and ω_{rel} is the relative angular velocity between them.

To ensure realistic behaviour of the bulk material, calibration of the sliding and rolling friction coefficients has been performed in this study. Laboratory scale experiments were executed to determine the characteristic behaviour of the material. These experimental results were used to calibrate the material to confirm the ability of the DEM material model to capture the material behaviour realistically. A detailed description of the calibration can be found in Section 3.3.

3.2.2 Sliding wear model

Archard wear model [148] is applied to calculate the wear volume caused by the sliding of particles. This wear model has been widely used for bulk handling process, such as the prediction of the wear of mill lifters [149] and local failure prediction of abrasive wear on tipper bodies [150]. Equation (3.4) shows the generalized equation to calculate sliding wear volume,

$$W_v = k\frac{F_n}{H_s}l_s \tag{3.4}$$

where W_v (mm^3) is the wear volume, H_s (N/mm^2) is the hardness of the surface, k is a dimensionless wear coefficient, F_n (N) is the normal force applied to an equipment surface, and l_s (mm) is the sliding distance. By introducing the coefficient of sliding wear α_s in Equation (3.5),

$$\alpha_s = \frac{k}{H_s} \tag{3.5}$$

Equation (3.4) is simplified as Equation (3.6).

$$W_v = \alpha_s F_n l_s \tag{3.6}$$

3.3 Calibration of DEM parameters

3.3.1 Experiments

River gravel, which is classified as dry, non-cohesive, and free-flowing, is used in this research. A sample of the river gravel is shown in Figure 3.2, and the particle size distribution is given in Figure 3.3.

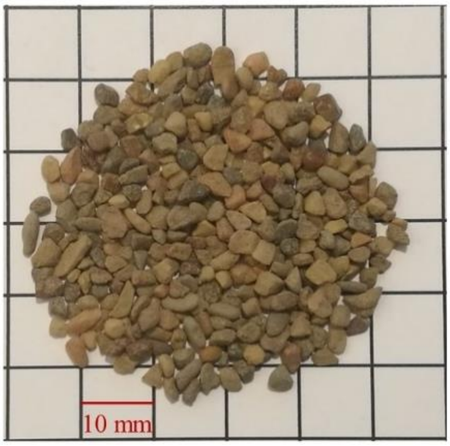

Figure 3.2 Sample of river gravel

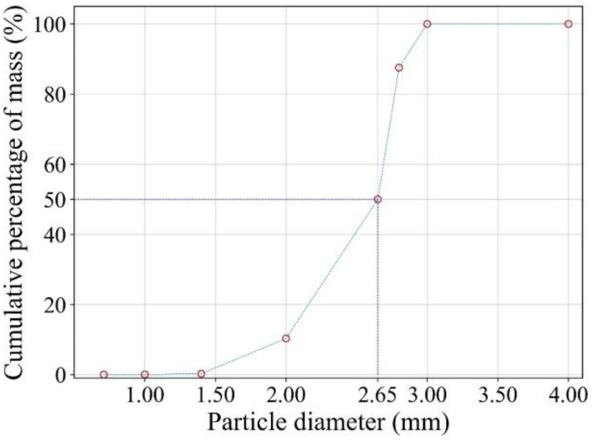

Figure 3.3 Particle size distribution

The shear box test (Figure 3.4) and drawdown test (Figure 3.5) were executed at The University of Newcastle, Australia, to characterize the relevant bulk properties. Both the tests were performed three times for repeatability.

The shear box is made of Perspex with dimensions of 200 × 200 × 200 mm^3. In the experiment, a total mass of 11.64 kg of river gravel is poured into the box to a filling height of 200 mm. After the preparation, the right wall is opened, and the remaining gravel forms a slope. The angle of the slope is called shear angle.

The box of the drawdown test is made of two kinds of materials which are Perspex for front and back walls and steel for side walls. The upper box and lower box have the identical dimensions with length of 500 mm, width of 100 mm, and height of 500 mm. A square opening is positioned at the bottom center which can be opened to allow the discharge of the bulk material. A total mass of 19.68 kg of the river gravel fills a height of 280 mm in the upper box. The outflowing bulk material forms a pile in the lower box, while the remaining bulk material forms two slopes in the upper box. In addition, the test allows the measurement of the discharge time during the experiment. After the measurement of discharge time T_d, the shear angle α_{DD} and angle of repose β_{DD} are determined.

Figure 3.4 and Figure 3.5 show the examples of the shear box test and drawdown test. The experimental results are summarized in Table 3.1. For the shear box test, the averaged shear angle of the shear box test was determined as 30.0 ± 0.4 degrees. For the drawdown test, the averaged shear angle and angle of repose are 36.1 ± 0.5 and 33.3 ± 0.9 degrees respectively. In addition, the averaged discharge time of the drawdown test is 5.4 ± 0.1 seconds.

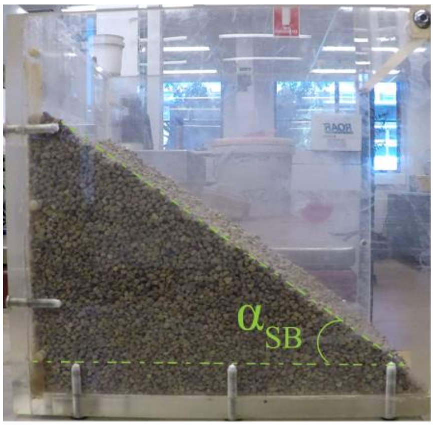

Figure 3.4 Shear angle in the shear box test

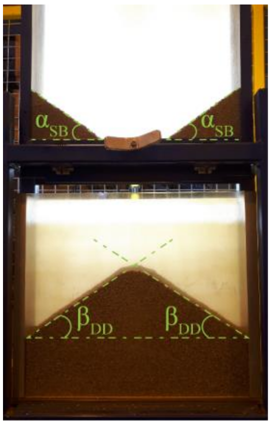

Figure 3.5 Shear angle and angle of repose in the drawdown test

Table 3.1 Summary of the experimental results

Experiment	Measured variable	Value
Shear box	α_{SB}	36 ± 0.4°
Draw down test	α_{DD}	36.1 ± 0.5°
	β_{DD}	33.3 ± 0.9°
	T_d	5.4 ± 0.1s

3.3.2 DEM calibration

To save computational time, particles with a size lower than 2 mm are neglected in DEM simulations as those only account for 0.26 % of the total mass shown in Figure 3.3. Based on literature review [150–152], the coefficient of sliding friction $\mu_{s,p\text{-}p}$ and the coefficient of rolling friction $\mu_{r,p\text{-}p}$ between particles are the most influential parameters on bulk flow properties, so these two parameters need to be calibrated. The other parameters of the DEM model are given in Table 3.2. The particle solids density is calibrated by the drawdown test in the filling process since the shear angle for the shear box test is not sensitive to the particle solids density [151].

Table 3.2 General DEM parameters

Categories	Parameters	Values
River sand	Particle density (kg/m^3)	2460
	Poisson ratio υ (-)	0.24
	Shear modulus G (GPa)	0.07
Perspex	Density (kg/m^3)	1200
	Poisson ratio υ (-)	0.5
	Shear modulus G (GPa)	0.1
Steel	Density (kg/m^3)	7932
	Poisson ratio υ (-)	0.3
	Shear modulus G (GPa)	78
Particle-particle	Coefficient of restitution	0.45
Particle-perspex	Coefficient of restitution (-)	0.4
	Coefficient of static friction (-)	0.36
	Coefficient of rolling friction (-)	0.36
Particle-steel	Coefficient of restitution (-)	0.6
	Coefficient of static friction (-)	0.38
	Coefficient of rolling friction (-)	0.3
Time step	Δt (s)	5×10^{-6}
Gravitational acceleration	G (m/s^2)	9.81

The shear box test is performed first to get a rough range of possible combinations of these two parameters because this test needs less computational time compared with the drawdown test. To reduce the computational time, the effect of the box dimensions is investigated. Based on [140], a similar shear angle is obtained when the width of the shear box is four times larger than the particle diameter with a periodic boundary condition. Considering the d_{50} of the river gravel is 2.65 mm, as shown in Figure 3.3, the width of the box is set as 20 mm under the application of periodic boundary conditions. In the test, both the coefficients of sliding and rolling friction are set at 0.24. Three sizes are evaluated, and each test is repeated three times. The results listed in Table 3.3 show the shear angle of the shear box with a dimension of 100 mm by 100 mm can obtain a comparable result to that of 200 mm by 200 mm.

Table 3.3 Simulation results of shear box test

Dimension (mm^3)	Averaged α_{SB}(°)	Deviation (°)
200×200×20	31.2	0.9
150×150×20	30.4	0.5
100×100×20	31.1	0.7

After the investigation of the effect of the dimensions of the container on the shear angle, the total sixteen shear box test simulations are performed for a range of sliding and rolling friction coefficients listed in Table 3.4. Figure 3.6 shows the shear angle as a function of sliding and rolling frictions between particles. It can be seen that multiple combinations of these two coefficients result in the same shear angles. The area from 36° to 38° represents the potential combinations to match the experimental results.

Table 3.4 Coefficients of sliding and rolling friction in DEM simulations

$\mu_{s,p\text{-}p}$	0.2	0.4	0.6	0.8
$\mu_{r,p\text{-}p}$	0.1	0.3	0.5	0.7

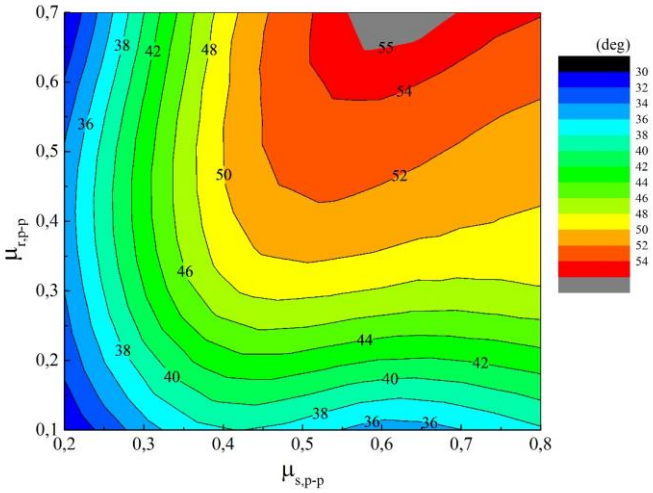

Figure 3.6 Shear angle results of shear box test

For the drawdown test (see Figure 3.5), the width of the box is set as 60 mm because when the width of the box is higher than 20 times the particle diameter, the wall effect can be neglected [152]. This means the shear angle, angle of repose, and discharge time are only determined by the contact parameters. To obtain the final combination, two steps are used for the drawdown test. First, a wide range of $\mu_{s,p\text{-}p}$ from 0.2 to 0.7 is investigated to obtain a narrow scope. Second, a detailed investigation is conducted at this narrow scope.

Table 3.5 lists the selection of the combinations for the first step. As explained in [151], the coefficient of static friction determines the discharge time and increasing the coefficient of static friction reduces the mass flow rate and increases the discharge time. In contrast, the coefficient of rolling friction has minor influence on the discharge time. Therefore, the coefficient of static friction should be lower than 0.3 to guarantee a faster discharge.

Table 3.5 Selection of combinations

Run	$\mu_{s,p\text{-}p}$	$\mu_{r,p\text{-}p}$	β_{DD} (°)	α_{DD} (°)	T_d (s)
1	0.2	0.45	35.1	35.5	6.2
2	0.3	0.15	36.9	37.6	10.5
3	0.5	0.1	26.3	36.0	12.3
4	0.6	0.12	37.5	38.8	11.1
5	0.7	0.1	28.0	36.9	10.9

For the second step, the value of $\mu_{s,p\text{-}p}$ is selected at a range of 0.21 to 0.29 with an interval of 0.01 and the corresponding $\mu_{r,p\text{-}p}$ is chosen from Figure 3.6. Finally, a combination of (0.21, 0.4) ($\mu_{s,p\text{-}p}$, $\mu_{r,p\text{-}p}$) satisfies the experimental results, as shown in Table 3.6.

Table 3.6 Comparison between experimental and simulation results

Test	Criteria	Experimental result	Simulation result
Shear box	α_{SB} (°)	36.0 ± 0.4	35.7
Draw down test	α_{DD} (°)	36.1 ± 0.5	36.3
	β_{DD} (°)	33.3 ± 0.9	34.3
	T_d (s)	5.4 ± 0.1	5.6

3.4 Experimental design for simulations

3.4.1 Simulation setup

A convex pattern surface, as shown in Figure 3.7 can be described by five parameters [5,132]: major and minor radii a and b, vertical and horizontal distance c and d, and height of the convex h. To ensure that the sliding wear happens only on the top surface, the sample is covered by a holder. The sample is meshed using Ansys Workbench 18.2 to demonstrate the wear distribution. It should be noted that the sliding wear does not remove the surface material, and the sample keeps intact during the simulation.

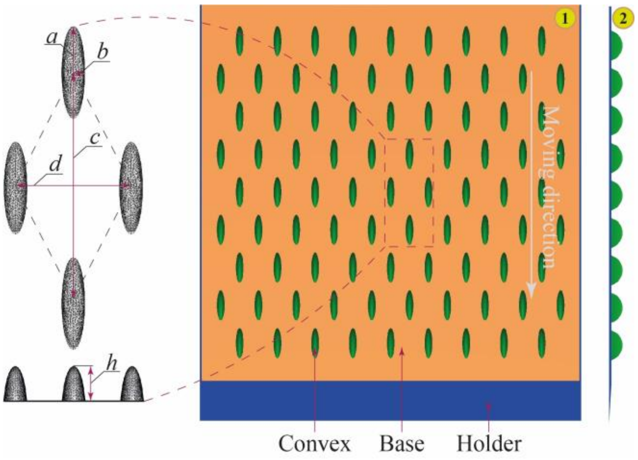

Figure 3.7 Meshed convex pattern surface based on [132] (1) top view, (2) side view (a: major radius; b: minor radius; c: vertical distance; d: horizontal distance; h: height of convex)

In terms of operational conditions, the normal load [57] and the relative velocity [21,61] have significant effect on the sliding wear. The normal load is directly related to the particle bed thickness, which is defined by the depth of the particle bed, so particle bed thickness is selected as an operational condition. The velocity of the sample is achieved by applying a constant velocity to the sample in y-direction. Figure 3.8 shows a particle bed clipped from the middle (thickness t) with dimensions of 2000 mm by 300 mm. The sample with the dimensions of 200 mm by 200 mm is located at the left bottom center of the particle bed and moves in y-direction with a velocity v.

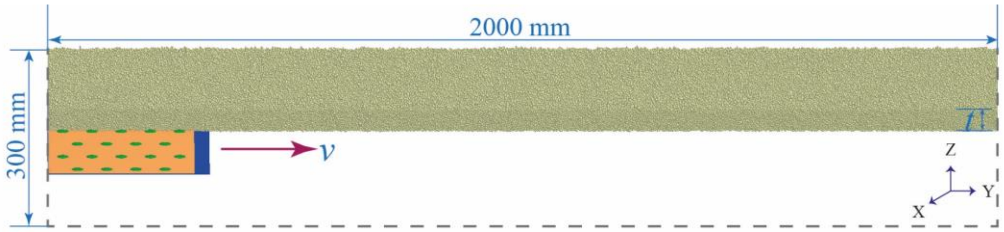

Figure 3.8 Simulation setup (clipped from the middle of the particle bed with v sample velocity, t particle bed thickness)

The central and side bins are linked to and move with the sample to investigate the contact behaviour between particles and the sample, as shown in Figure 3.9. The dimensions of the central bins are 200 mm by 200 mm and side bins 200 mm by 50 mm. The moving bins consist of several multiple layers from the bottom to the surface of the particle bed, and the thickness of each layer is set as 5 mm.

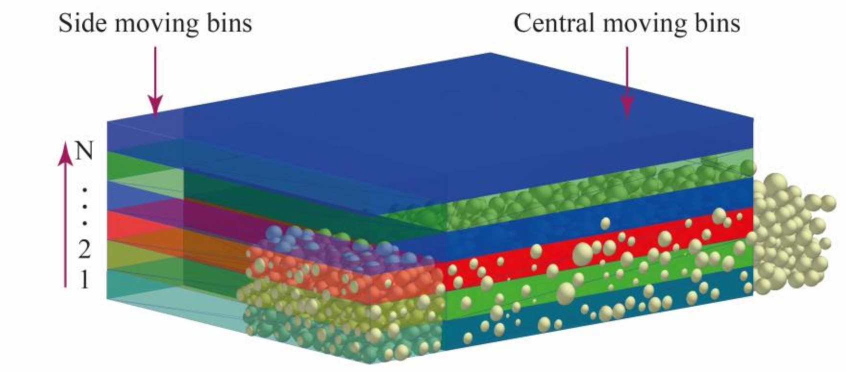

Figure 3.9 Setting of moving bins (clipped from the middle of the sample)

3.4.2 Definitive screening design (DSD)

Screening design is a major use of fractional factorial design [153], which is used to identify the factors that affect the response. In this research, the response, which is the dependent variable, is the sliding wear volume, and the independent variables are the six factors listed in Table 3.7. A three-level definitive screening design is applied to this research, as it is able to assess the curvature of the factor-response relationship [154]. For the screening design, the independent factors should be at a wide but reasonable range [153]. Therefore, level 2 is two times higher than level 1, and level 3 four times higher than level 1 except for the horizontal distance d. Considering the particle size distribution, the level 1 of the major and minor radii are set as 2 mm. To guarantee the space between two convexes, the horizontal distance should be at least two times higher than the minor radius, so level 1 of d is set as 20 mm. The horizontal distance d is increased by 20 mm from level 1 to level 3. The vertical distance c has no influence on the sliding wear reduction [5] and is therefore kept constant as 40 mm.

Table 3.7 Six factors at three levels for screening design

Factors	Levels		
	Minimum (-1)	Middle (0)	Maximum (1)
a (major radius/mm)	2	4	8
b (minor radius/mm)	2	4	8
d (horizontal distance/mm)	20	40	60
h (height/mm)	1.5	3	6
v (sample velocity/m/s)	0.5	1	2
t (bed thickness/mm)	10	20	40

Table 3.8 shows the three-level definitive screening design pattern. The columns of the design are orthogonal to each other if the level 1, 2, and 3 are regarded as -1, 0, and 1, respectively, which means that in the list of test runs, the levels of each factor occur an equal number of times with each of the levels of the other factors. This design ensures that the estimated factor effects are statistically independent [154].

Table 3.8 Three-level definitive screening design for six factors

Run order	Run Pattern	Factors					
		a	b	d	h	v	t
R1	+0+--+	8	4	60	1.5	0.5	40
R2	-++-0-	2	8	60	1.5	1.0	10
R3	+-+0+-	8	2	60	3.0	2.0	10
R4	0-----	4	2	20	1.5	0.5	10
R5	0+++++	4	8	60	6.0	2.0	40
R6	000000	4	4	40	3.0	1.0	20
R7	++0+--	8	8	40	6.0	0.5	10
R8	-+-0-+	2	8	20	3.0	0.5	40
R9	+--+0+	8	2	20	6.0	1.0	40
R10	--++-0	2	2	60	6.0	0.5	20
R11	-0-++-	2	4	20	6.0	2.0	10
R12	++--+0	8	8	20	1.5	2.0	20
R13	--0-++	2	2	40	1.5	2.0	40

3.4.3 Analysis procedure

The analysis of the wear results should be based on the steady state of the simulation setup. Therefore, the stability of the simulation setup is evaluated first. In order to verify that the convex pattern surface can reduce the sliding wear, the simulations with plain surfaces under corresponding operational conditions listed in Table 3.8 are performed as references.

The stability of the sliding process includes two aspects: the bulk flow steady state and the sliding wear stability. Correspondingly, two criteria are used to evaluate the stability of the sliding process: relative velocity of bulk material and relative wear gradient of samples.

For the relative velocity of bulk material, it is considered that the particle flow reaches a steady state when the ratio of the averaged particle velocity at the sample moving direction (y-direction) to the sample velocity approaches a steady value. It should be noted that only the particles in the central moving bins (see Figure 3.9) with the original particle bed height are considered for this criterion. The relative velocity η is defined as

$$\eta = \frac{\overline{v_p}}{v_s} \times 100\% \tag{3.7}$$

where η is relative velocity, $\overline{v_p}$ (mm/s)is averaged particle velocity in sample moving direction, and v_s (mm/s) is the translational velocity of the sample.

Relative wear gradient φ_R is used to evaluate the stability of the sliding wear process, which is denoted by Equation (3.8),

$$\varphi_R = \frac{\varphi}{\max(\varphi)} \tag{3.8}$$

where φ_R is relative wear gradient, φ (mm^3/mm) is wear gradient, and max(φ) (mm^3) is the maximum value of wear rate among all simulations.

The wear gradient φ is denoted by Equation (3.9)

$$\varphi = \frac{W_{v,s} - W_{v,s-\Delta s}}{\Delta s} \tag{3.9}$$

where Δs (mm) is displacement increment of the sample, and $W_{v,s} - W_{v,s-\Delta s}$ (mm^3) is wear volume increment.

After the analysis of the stability of the simulation setup, the sliding wear result is investigated. A relative wear volume is used to compare the sliding wear for Group A and Group B separately pointed in Section 3.5.

The relative wear γ is defined by Equation (3.10),

$$\gamma = \frac{w_{v,convex}}{\max\left\{w_{v,convex}, w_{v,flat}\right\}} \tag{3.10}$$

where γ, $W_{v,convex}$ (mm^3) and $W_{v,flat}$ (mm^3) indicate the relative wear, wear volumes of the convex sample and corresponding plain surface, respectively. max{$W_{v,convex}$, $W_{v,flat}$} represents the maximum value in each group.

The wear rate w_r is denoted by Equation (3.11),

$$w_r = \frac{W_v}{m} = \frac{W_v}{v \times t \times l \times \rho} \tag{3.11}$$

where w_r ($mm^3/(kg/s)$), W_v (mm^3), m (kg/s), v (m/s), t (mm), l (mm), and ρ (g/mm^3) represent wear rate, wear volume, mass flow rate, sample velocity, particle bed thickness, width of the particle bed, and bulk density, respectively.

3.5 Results

3.5.1 Steady state evaluation

Figure 3.10 shows the relative velocities of the thirteen simulations. These simulations are separated into two groups (Group A and B) based on the two bulk flow regimes, as shown in Figure 3.11.

The continuous flow regime of Group A as shown in Figure 3.10 has a relatively wide range of ratios from 15 % to 70 %. It can be divided into three subgroups because the simulations in those subgroups have common factors. For Group A1, the common factors are the horizontal distance (20 mm) and the particle bed thickness (40 mm). Group A2 has the same horizontal distance (60 mm) and the particle bed thickness (40 mm). Group A3 has the identical sample velocity (2 m/s). For the discontinuous flow regime of group B, the relative velocity is close to 100 %, which means the particles move with the sample at a close velocity, and this result is consistent with the flow regime shown in Figure 3.11 (b).

For all simulations, the relative velocities increase rapidly at the first 200 mm and experience a transitional state from 200 mm to 800 mm. Finally, all simulations reach a steady state from 800 mm to 1700 mm with fluctuations less than 7 %. The fluctuations occur because the particle bed height is always changing with the movement of the sample, so the averaged particle velocity changes.

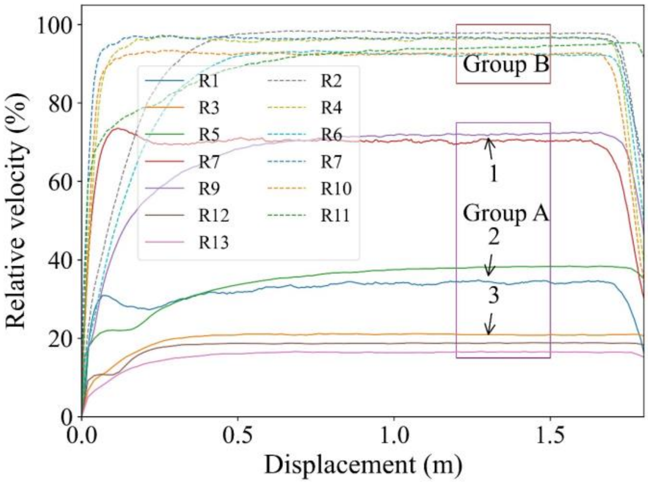

Figure 3.10 Relative velocity of particles

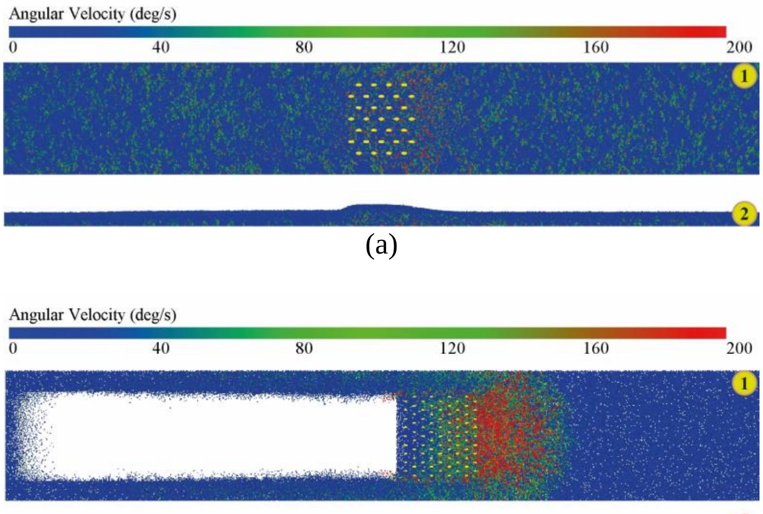

(a)

(b)

Figure 3.11 Bulk flow regimes (1: bottom view (x-y direction), 2: side view (y-z direction)), (a) Continuous flow regime of Group A, (b) Discontinuous flow regime of Group B

Figure 3.12 shows the relative wear gradient of all simulations. It can be seen that the continuous flow regime of Group A (including Group A1, A2, and A3) has significant high relative wear gradient than the discontinuous flow regime of Group B, which means the wear gradient is closely related to the bulk flow regimes. Group B shows a relatively high fluctuation, and all simulations have fluctuation of less than 0.002. The possible reason is that the discontinuous flow regime of Group B causes the particles to accumulate on and in front of the sample, so the accumulated particles influence the contact force between particles and the sample, therefore increasing sliding wear.

For all simulations, the relative wear gradient decreases rapidly at the first 200 mm and goes into a transitional state until 1000 mm. Finally, all simulations obtain a steady state from 1000 mm to 1700 mm. Combining the two stability criteria, all simulations reach a steady state from 1000 mm to 1700 mm, and the wear results are closely related to the flow regimes; so, the analysis of results is performed at the steady state separately, based on the two flow regimes.

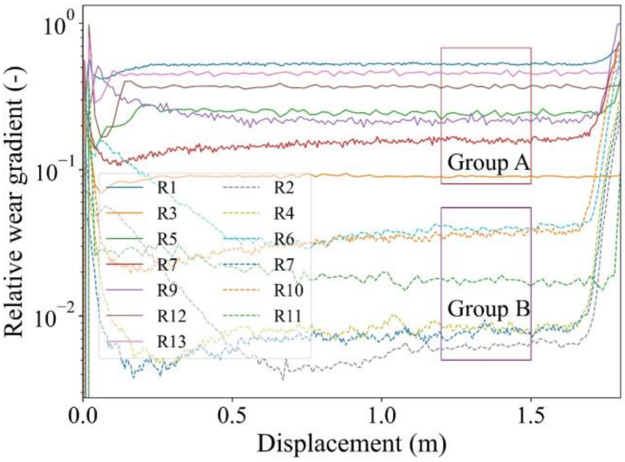

Figure 3.12 Relative wear gradient

3.5.2 Sliding wear

Figure 3.13 shows the relative wear rate of the two flow regimes indicated by Group A and B. Within the continuous flow regime of Group A, all convex surfaces except R12 can reduce the sliding wear, as shown in Figure 3.13 (a). The sample of the R12 is almost fully covered by the convexes based on Table 3.8, which indicates wrong combinations of the factors could increase the sliding wear. The rest designs show that the bases of the samples have higher proportions of the sliding wear compared with the convexes. R5 has the lowest relative wear rate and reduces the sliding wear by 66 % compared to the corresponding plain surface. Similarly, Figure 3.13 (b) indicates R2 has the lowest relative wear and reduces the sliding wear by 17 % compared with the corresponding plain surface. As the R5 (Group A) and R2 (Group B) have the lowest relative wear rates for these two flow regimes, they are selected for detailed analysis to reveal the bulk flow properties.

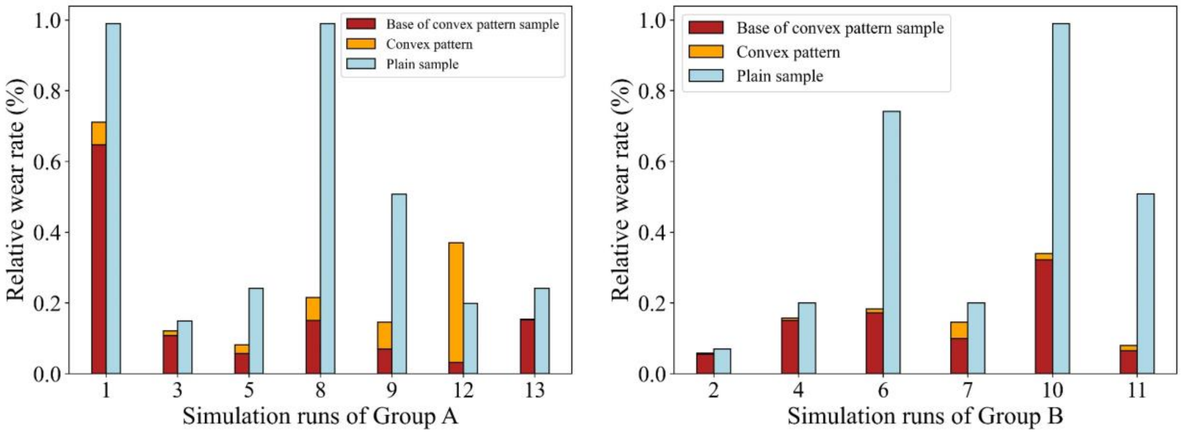

(a) (b)

Figure 3.13 Relative wear rate of convex pattern and plain surfaces, (a) continuous flow regime of Group A, (b) discontinuous flow regime of Group B

Figure 3.14 and Figure 3.15 illustrate the sliding wear distributions of the convex pattern and plain surfaces. Figure 3.14 demonstrates the wear distributions of the samples of R5 and the corresponding plain surface. For the base of the R5 in Figure 3.14 (a), the majority of the sliding wear appears at the front two rows of the convexes and the two sides of the sample as the first two rows alter the flow behaviour of particles. The wear path on the base indicates the guiding effect of the convex pattern. For the convex pattern, as shown in Figure 3.14 (a), the majority of wear appears at the front half part because contact between particles and the convex mainly takes place at this area. Figure 3.14 (b) shows the wear distribution of the corresponding plain surface. It is obvious that the sliding path is formed along the sample moving direction and the front part of the sample shows lower sliding wear than the back part. The reason lies in that the normal force in the front part is relatively lower than the rest of the part because of particle accumulation.

Figure 3.15 indicates the front and the side of the convex pattern and plain sample encounter the most severe wear because of particle accumulation at the front and wall effect at the side. It should be noted that the corresponding plain surfaces of the R2 and R5 have different flow regimes which influence the wear distribution.

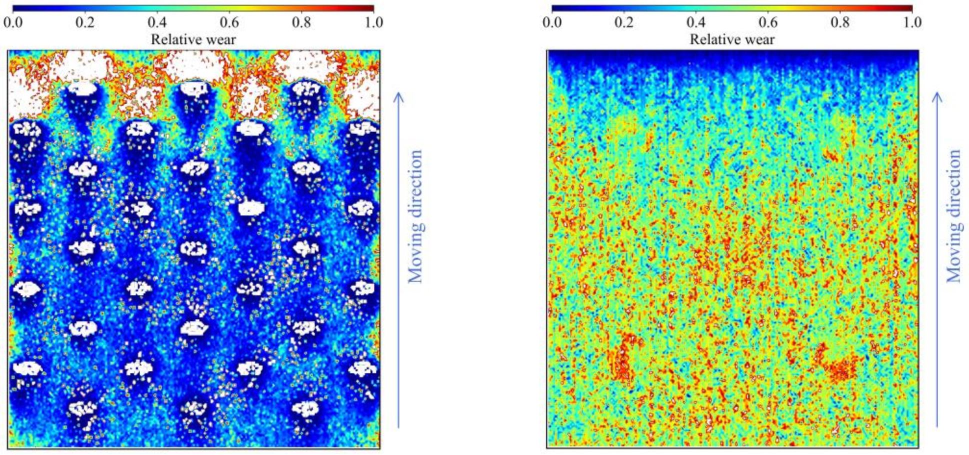

(a) (b)

Figure 3.14 Wear distribution of R5 and the corresponding plain surface (continuous flow regime), (a) Convex surface of R5, (b) Plain surface

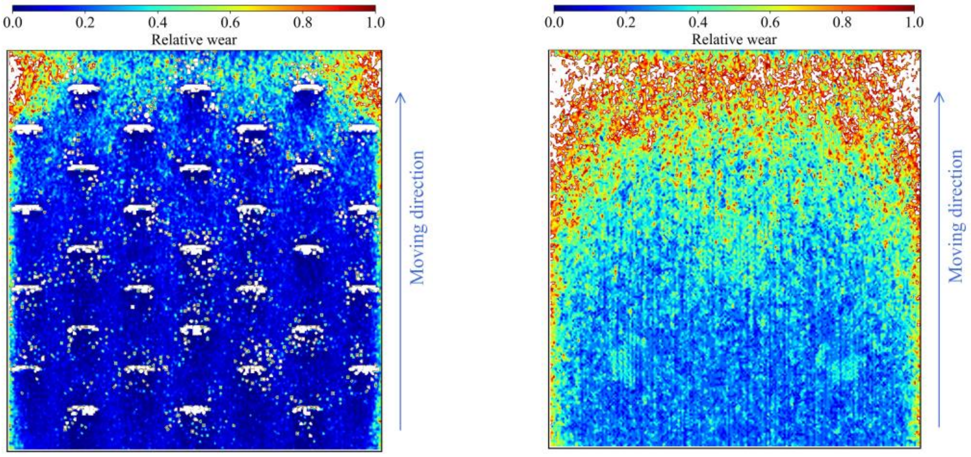

(a) (b)

Figure 3.15 Wear distribution of R2 and the corresponding plain surface (discontinuous flow regime), (a) Convex surface of R2, (b) Plain surface

Figure 3.16 compares the normal force of the samples and the error bars represent the standard deviation. For both the two flow regimes, the normal forces of the convex pattern samples are higher than that of the plain surfaces. Although the normal force of the convex pattern surfaces is higher than that of the plain surfaces, the relative wear rate is lower except run 12 shown in Figure 3.13. Considering the lower wear rate and a similar normal force, this means the sliding distance of the particles on the convex pattern sample is significantly reduced.

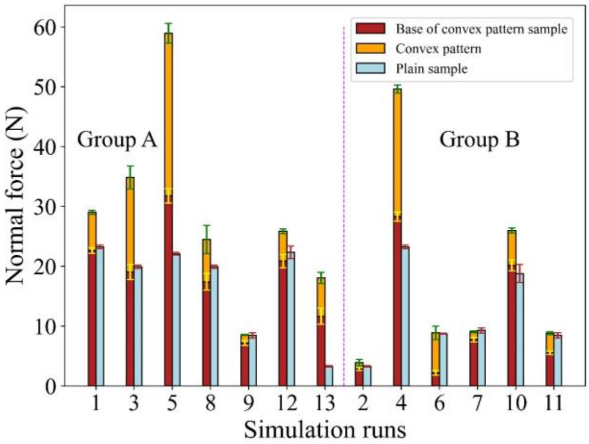

Figure 3.16 Normal force of samples

3.5.3 Bulk property analysis

3.5.3.1 Bulk flow regimes

The two bulk flow regimes mentioned before are indicated in Figure 3.17 and Figure 3.18. It should be noted that the colored particles represent the magnitude of angular velocity.

For the continuous flow regime of R5 as shown in Figure 3.17 (a), the side view indicates the particles accumulation at the back part of the sample. From the bottom view, it can be seen that the particles around and in front of the sample have higher angular velocity. The cross-section view demonstrates that the accumulated particles flow to the side and are then deposited in the shape. The same flow regime happens to the corresponding plain surface, and the particle bed profile is barely influenced by the plain surface, as shown in Figure 3.17 (b). Compared to the bottom view of the plain surface, R5 activates more particles with high angular velocity, which verifies that the convex pattern surface can facilitate the rolling of particles.

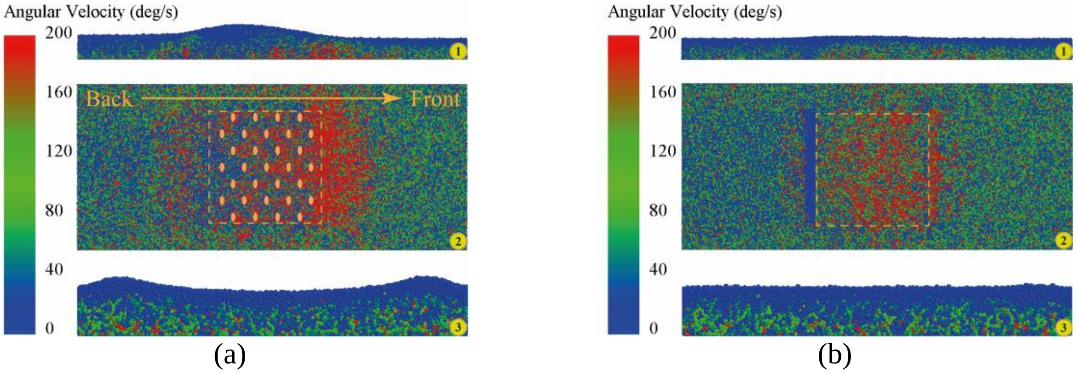

(a) (b)

Figure 3.17 Continuous flow regime with (1: side view clipped from the middle, 2: bottom view, 3: cross-section view) (a) convex surface of R5, (b) plain surface

Figure 3.18 shows the discontinuous flow regime of R2 and the corresponding plain surface. For R2 in Figure 3.18 (a), the accumulation of particles appears in front of the sample, as shown from the side view. The bottom view indicates that almost all particles over the sample travel with the sample at the same velocity, and only the particles in front of the sample have relatively high angular velocity. The cross-section view depicts that the particle bed with the side part covered with particles is formed. The corresponding plain surface shows the similar particle bed profile, as shown in Figure 3.18 (b). The main reason lies in the effect of the combination between the particle bed thickness and the sample velocity.

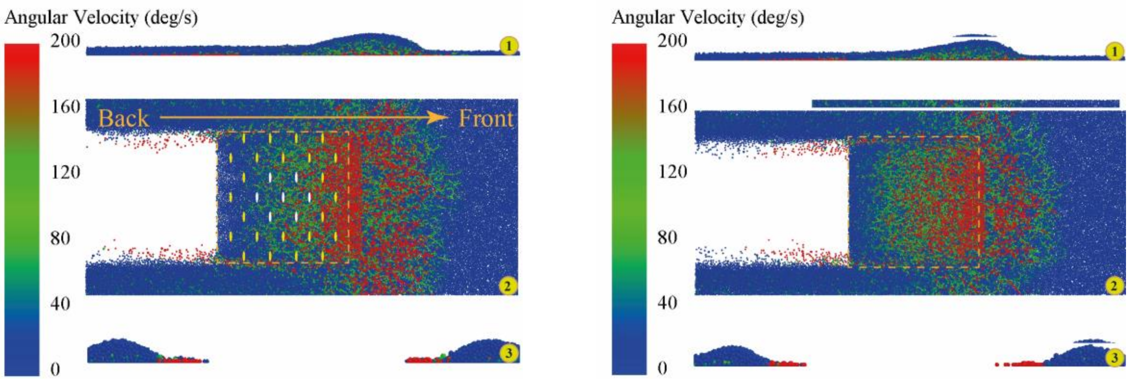

(a) (b)

Figure 3.18 Discontinuous flow regime (1: side view clipped from the middle, 2: bottom view, 3: cross-section view) (a) convex surface of R2, (b) plain surface

3.5.3.2 Particle velocity profile

Particle velocity profiles of R5 and R2 are used to investigate the influence of the sample on the movement of particles. The profiles include the averaged particle velocity in y-direction, the ratio of the averaged particle velocity in x-direction to that of in y-direction, and the ratio of the averaged particle velocity in z-direction to that of in y-direction. The profiles are based on the moving bins illustrated in Figure 3.9.

Figure 3.19 shows the particle velocity profile of the R5 and the corresponding plain surface. For the averaged particle velocity as shown in Figure 3.19 (a), R5 has higher velocity than the plain surface both in the central and side moving bins. For R5, the particle velocity decreases from about 1.5 m/s at layer 1 to 0.4 m/s at layer 8 and keeps around 0.4 m/s for the others. The side moving bins indicate the opposite trend that the averaged velocity lower than 0.1 m/s at the first 8 layers increases slowly, and the velocity reaches less than 0.25 m/s for the rest of the layers. For the plain surface, every layer shows a lower velocity than 0.2 m/s at the central bins, and the particles at the side bins are hardly influenced by the plain surface. It can be seen that the convex pattern sample can significantly influence the movement of particles at the bottom layer. Considering the sample velocity is 2 m/s, Figure 3.19 (a) indicates the majority of particles moves much slower than the sample and therefore stays behind the sample.

The ratio of the averaged particle velocity in x-direction to that of in y-direction reflects the trend of particles to move sideways. For the central moving bins of R5 as shown in Figure 3.19 (b), the velocity ratio is close to 0, which means the tendency of particles to move sideways is negligible. For the side moving bins, the ratio increases from 0.1 to 0.7 at the first 8 layers and decreases to 0.5 at layer 11. This indicates that the particles at the side bins have a strong tendency to move to the sides of the particle bed. The reason is that the accumulated particles over the sample are forced to move sideways, and the particles at the bottom layer close to the sides of the sample are pushed sideways. The plain surface has a similar tendency with R5 both in the central and side bins. For the R5 and the plain surface, all ratios are less than 0.7, which means the particles are more likely to move in the sample moving direction, especially at the central moving bins.

The ratio of the particle velocity in z-direction to that of in y-direction shows the trend of particles to move across layers, as shown in Figure 3.19 (c). For the central moving bins of R5, the ratio increases from 0 to near 0.3 at the first eight layers and then decreases to 0 at the top layer. The side bins show the ratio increases to 0.4 at the first eight layers and declines to below zero. It should be noted that the first eight layers form the original particle bed, and the particle accumulation forces the particles to move vertically, so the first eight layers show the increasing ratio both at the central and side bins. The influence of the sample on the accumulated particles decreases, so the ratio drops from the layer eight to the top layer. The corresponding plain surface shows the similar trends both at the central and side moving bins.

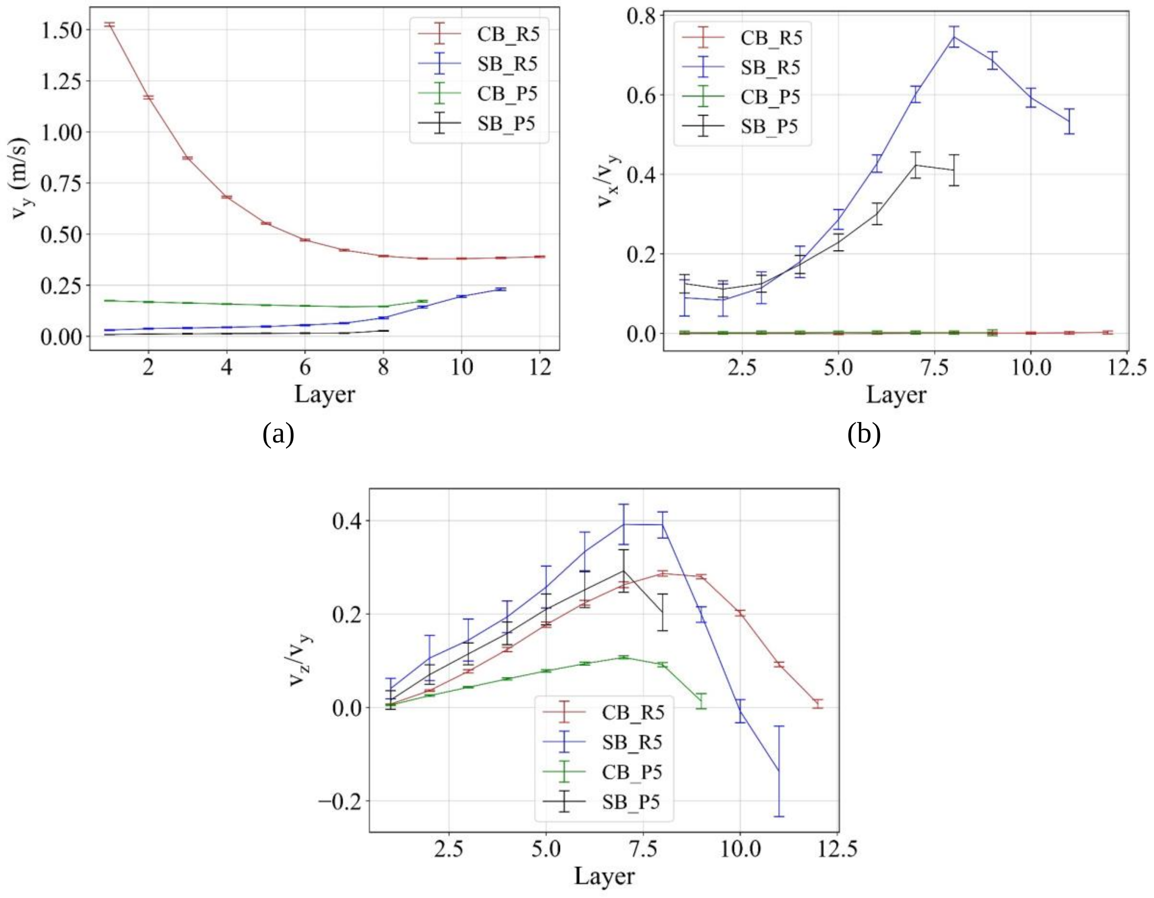

(a) (b)

(c)

Figure 3.19 Particle velocity profile of R5 and the corresponding plain surface (CB—central moving bins; SB—side moving bins; R5—run 5; P5—plain surface of R5), (a) average velocity in y-direction, (b) ratio of v_x to v_y, (c) ratio of v_z to v_y

Figure 3.20 shows a similar particle velocity profile of R2 and the corresponding plain surface. For the averaged velocity in y-direction as shown in Figure 3.20 (a), the central moving bins indicate high velocity close to 1 m/s. This means the particles are moving forward with the sample at the same velocity. For the side moving bins, the velocity increases slowly at the first two layers from 0.1 m/s to 0.15 m/s and rapidly to close to 0.7 m/s at the top layer. This is because the original particle bed height is 10 mm which fills two layers of the bins, while the other layers are filled by the accumulated particles with high velocity.

Figure 3.20 (b) shows the tendency of particles to move sideways. For the central moving bins, the velocity ratio is close to 0, which indicates the particles at the central moving bins do not tend to move sideways. For the side moving bins, the velocity ratio of the plain surface increases from 0.14 in layer 1 to 0.3 in the layer 4 and slightly decreases to 0.27. This shows that the particles in the side moving bins have the tendency to move sideways, and the trend is stronger at the top layers. For the R2, the ratio increases from 0.05 in the bottom layer to 0.14

in the top layer with a relatively high fluctuation. Although the particles tend to move sideways, the tendency is lower than that of the plain surface.

Figure 3.20 (c) shows the tendency of particles to move across layers. For the central moving bins of the R2, the ratio is close to zero, which is because the particles have high velocity in y-direction and make the ratio low. For the side moving bins, the ratio is negative and the absolute value of the ratio increases from 0.02 to 0.09 at the first three layers and decreases to 0.06. The negative value indicates the particles have the tendency to move downwards. The reason lies in that the accumulated particles at the central moving bins are forced to move sideways and downward to side moving bins. The corresponding plain surface shows the similar trend both at the central and side moving bins.

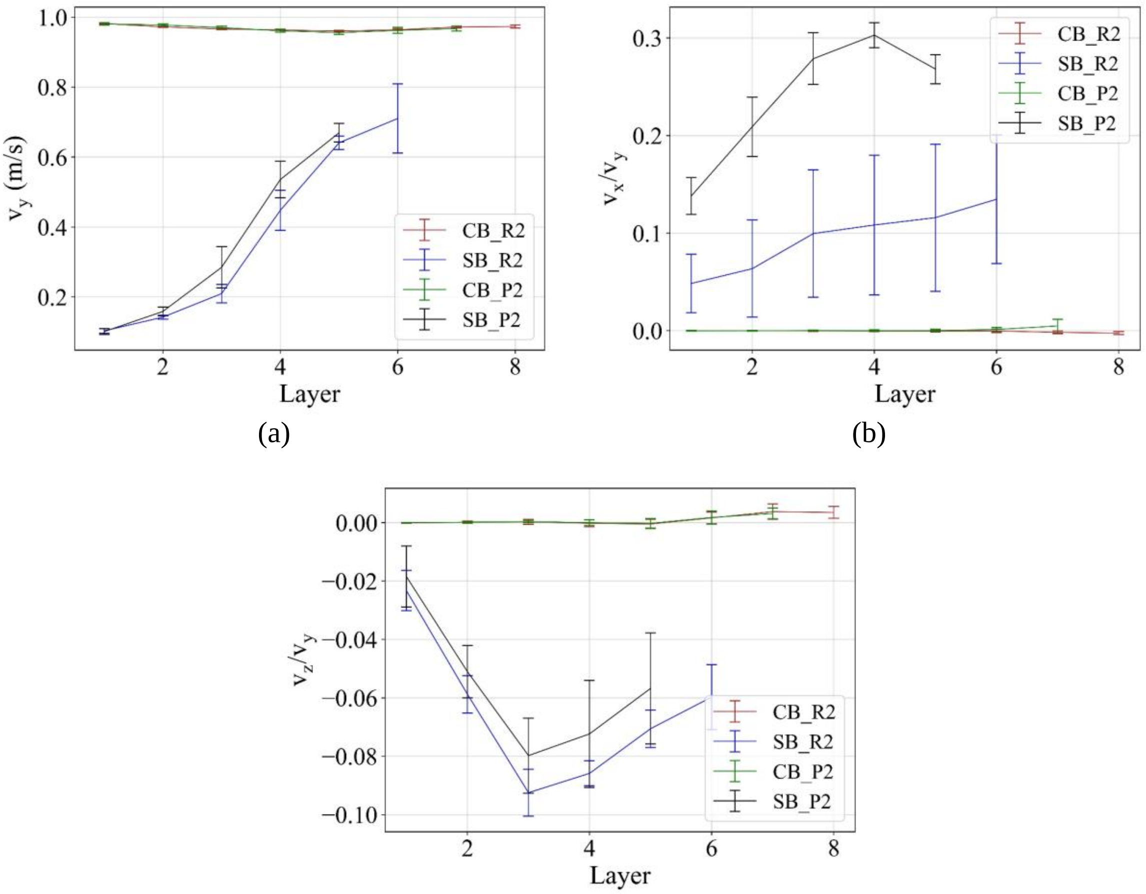

(a) (b)

(c)

Figure 3.20 Particle velocity profile of R2 and the corresponding plain surface (CB—central moving bins; SB—side moving bins; R2—run 2; F2—plain surface of R2), (a) average velocity in y-direction, (b) ratio of v_x to v_y, (c) ratio of v_z to v_y

3.5.3.3 Particle angular velocity profile

The particle angular velocity profile shows the magnitude of the averaged angular velocity and reflects the rolling effect of the convex pattern, as the rolling instead of sliding of particles is the main mechanism to reduce the sliding wear.

Figure 3.21 shows the similar trend of particle angular velocity of R5 and the corresponding plain surface. The angular velocity decreases from bottom layer to top layer and the particles at the central moving bins have higher angular velocities than those of at the side moving bins. The side moving bins for both the R5 and the plain surface have the angular velocity of lower than 120 deg/s. For the central moving bins, the top layer of the R5 has the highest value of higher than 320 deg/s which is more than two times higher than that of the plain surface. The angular velocity drops significantly to the second layer, which means the convex pattern surface can induce the rolling and reduce the sliding of particles contacting with the convex pattern.

R2 and the corresponding plain surface show the similar trend of the angular velocity for both the central and side moving bins. This indicates the convex pattern surface can hardly influence the motion of the particles at the discontinuous flow regime, and the flow regime dominates the motion of particles.

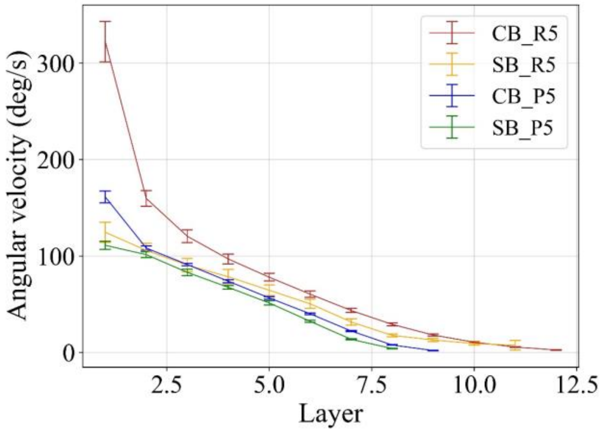

Figure 3.21 Angular velocity profile of R5 and the corresponding plain surface (CB—central moving bins; SB—side moving bins; R5—run 5; P5—plain surface of R5)

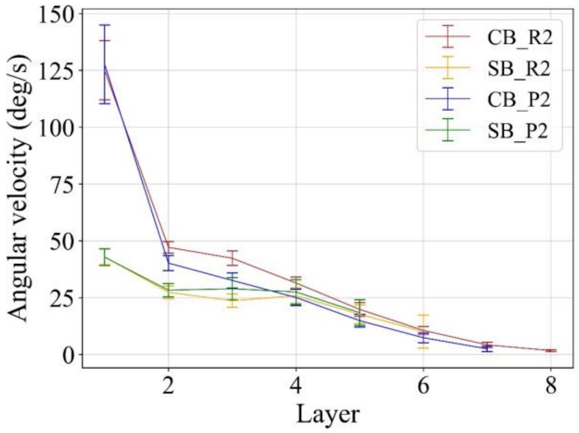

Figure 3.22 Angular velocity profile of R2 and the corresponding plain surface (CB—central moving bins; SB—side moving bins; R2—run 2; P2—plain surface of R2)

The bulk flow regimes have significant influence on the motion of particles and determine the mechanisms of the reduction of the sliding wear. The convex pattern surface can convert the sliding to the rolling of particles at the continuous flow regime. The discontinuous flow regime reduces the relative motion between particles and the sample and therefore leads to severe particle accumulation. Compared with the plain surface, the convex pattern has slight influence on the rolling of particles at the discontinuous flow regime.

3.5.4 DSD analysis

To quantify the effect of the factors, a regression equation is fitted based on the normalized wear results obtained by dividing the highest value of the wear volumes. Table 3.9 lists the fitted model and the corresponding R2. The fitted model is non-hierarchical because it does not contain all of the lower order terms (factor b and d) for each term (interaction b×d) in the model, so this model is fitted in coded unit logarithm ln(y). The model indicates that three main factors and one two-level interaction have significant influence on the sliding wear volume. The R2 value of more than 95 % indicates the goodness of the fit to the data points.

Table 3.9 Regression equation of fitted model

Response	Regression equation in coded units	R^2	R^2 (adj)	R^2 (pred)
ln(y)	$y=-1.859+0.449a+0.650v+$ $1.425t-0.629b\times d$	95 %	92 %	86 %

A significance level of 0.05 (α) is chosen in this design to assess the terms. As listed in Table 3.10, the p-values of the coefficients of the constant, a, v, t, and the interaction b×d are lower than 0.05, which means a statistically significant association between the sliding wear volume and the terms of the regression equation. The higher the coefficient of a factor is, the more important the factor is on the effect of the sliding wear. Therefore, the particle bed thickness has the most significant effect on the response, while the major radius has the least. In addition, the sample velocity and the interaction between the minor radius and the horizontal distance show a comparable influence on the sliding wear.

Table 3.10 Coefficients of the regression equation and the corresponding p-value

Term	Coefficient	p-value
Constant	-1.859	0.000
a	0.448	0.032
v	0.650	0.007
t	1.426	0.000
b×d	-0.633	0.013

A residual plot as shown in Figure 3.23 is used to determine whether the fitted model is adequate and meets the assumptions of the analysis. The normal probability plot of residuals, as shown in Figure 3.23 (a) displays the relation between residuals and the expected values when the distribution is normal and verifies that the residuals are normally distributed as the plot of the residuals approximately follow a straight line. Figure 3.23 (b) demonstrates the relation between residuals and fitted values of response (normalized wear volume), which is used to verify the assumption that the residuals are randomly distributed with a relatively constant variance. It can be seen that the points fall randomly on both sides of 0 with no recognizable patterns in the points. Based on the analysis of the residual plots, it can be concluded that the regression model meets the assumption as listed in Table 3.9.

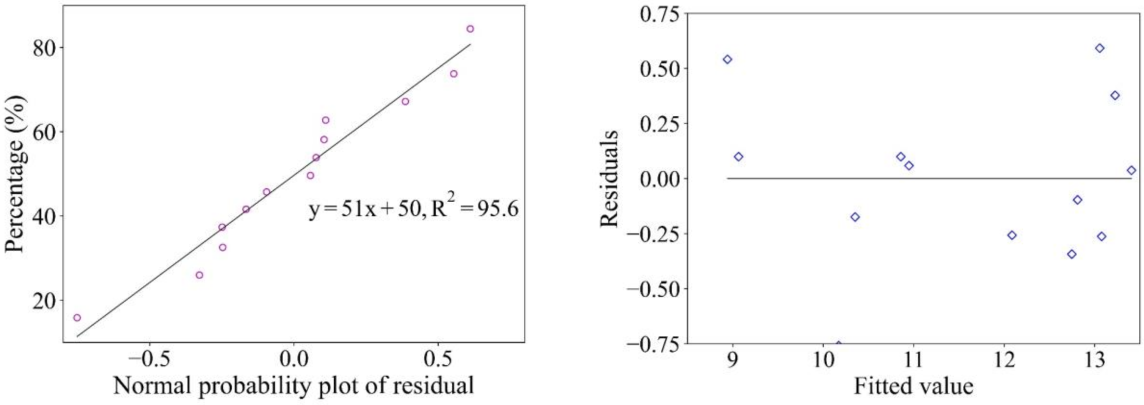

(a) (b)

Figure 3.23 Residual plot (a) normal probability plot, (b) fitted value vs residuals

A contour plot (Figure 3.24) is used to express the relationship between two factors and the normalized response values, while the other factors are kept at the middle level. For a specific wear volume, the three main factors show the negative linear correlations each other, which means the increase of one factor leads to the decrease of another factor. For Figure 3.24 (a), it can be seen that the major radius has a small effect on the sliding wear volume compared with the particle bed thickness. Figure 3.24 (b) shows that the influence of the major radius and the sample velocity is similar which is consistent with the analysis of model coefficients. Figure 3.24 (c) reveals that the sliding wear volume is linearly related to the particle bed thickness. The interaction between the minor radius and the horizontal distance is shown in Figure 3.24 (d). The curvature expresses the influence of one factor depends on another. As shown in Figure 3.24 (d), the sliding wear volume is low when both the minor radius and the horizontal distance have low or high levels at the same time.

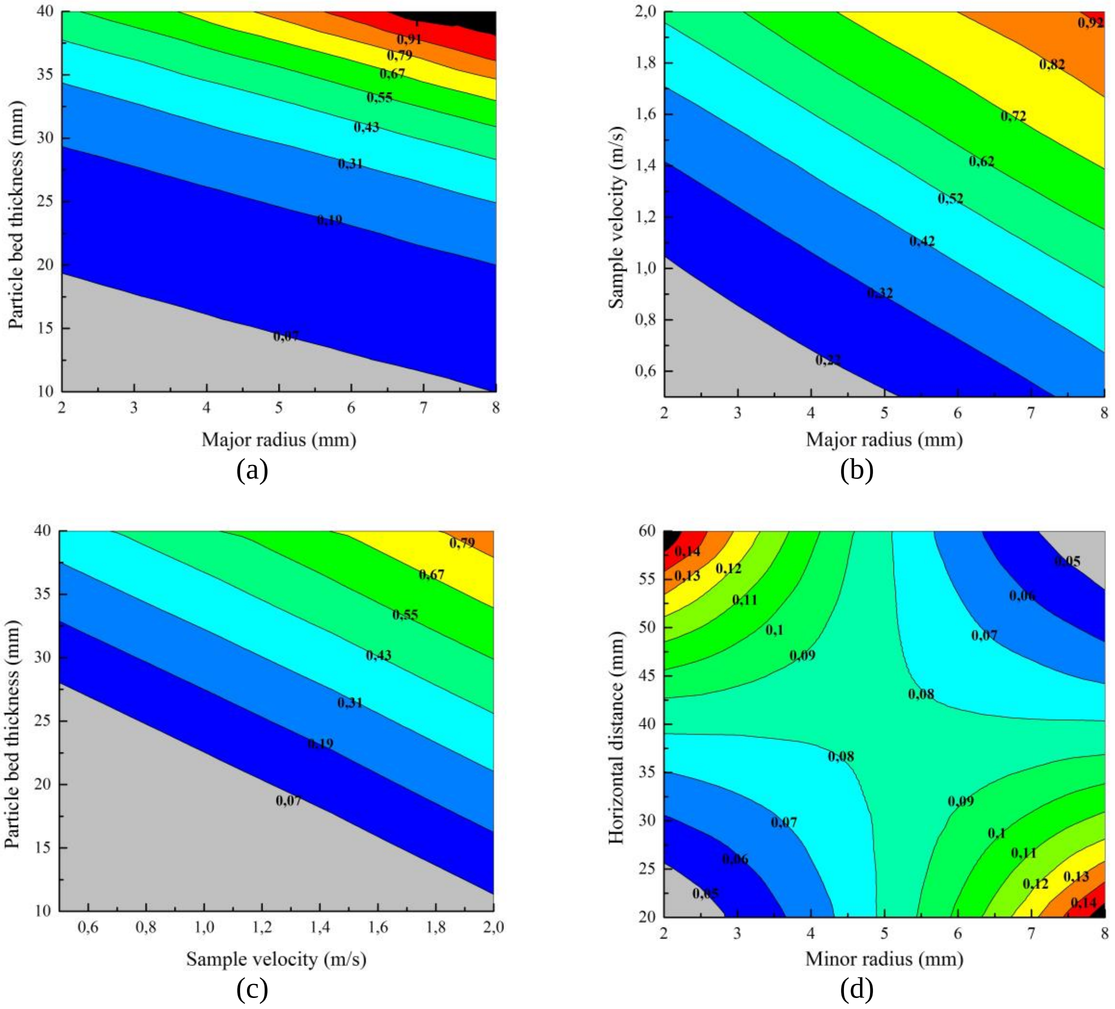

(a) (b)

(c) (d)

Figure 3.24 Normalized response contour plot (a) major radius and particle bed thickness, (b) major radius and sample velocity, (c) sample velocity and particle bed thickness, (d) minor radius and horizontal distance

3.6 Conclusions

This chapter addresses the question:

What is the effect of the parameters of the convex configuration on wear reduction performance of the convex pattern surface?

This chapter entails detailed investigations of bulk flow regimes and sliding wear mechanisms of the convex pattern surface. The aim of this work is to optimize a convex pattern surface to reduce the sliding wear caused by non-cohesive free flowing bulk material.

Two flow regimes are formed, namely, the continuous and discontinuous flow regime, and the mechanisms of the sliding wear reduction for the two flow regimes differ. For the continuous flow regime, the convex pattern surface can significantly facilitate the rolling of particles to reduce the sliding between particles and the sample. The discontinuous flow regime can reduce the relative sliding velocity and therefore decline the sliding distance. The continuous flow regime is preferred, as this flow regime induces less particle accumulation and more apparent rolling effect of particles.

Three main factors and one interaction have statistical significance based on the regression model. The particle bed thickness has the most significant influence on the sliding wear, and the flow regime is continuous when the particle bed thickness is 40 mm. The height and the minor radius of the convex have no significant influence on the sliding wear, which is consistent with the previous study.

R5 and R2 are the optimal design for the continuous and discontinuous flow regimes, respectively. The properties of the two runs hint to a design that is optimal in both regimes simultaneously. It should be noted that this optimal design is based on the specific dry bulk material with d_{50} of 2.65 mm, and it is suitable for bulk material with similar bulk properties.

4 The influence of particle size on sliding wear of a convex pattern surface*

Chapter 3 obtains an optimal convex pattern sample and the results indicate that the sample reduces the siding wear significantly by 66 % compared to a plain sample. However, as the bulk handling equipment deals with multiple materials with various particle size distributions, it is crucial to comprehend the effect of particle size on the sliding wear of the convex pattern sample. This chapter investigates the effect of particle size on sliding wear of the optimal sample by implementing a coarse graining technique. Section 4.2 demonstrates the particle upscaling theory for contact model and wear model. Section 4.3 verifies the scale invariance of the contact model and wear model through packing and pin-on-disc test, separately. Section 4.4 develops a numerical model and proposes analysis procedures. Section 4.5 compares the numerical results and builds the correlation between the particle size and wear volume of samples. Section 4.6 concludes the main findings.

---

*This chapter is based on Yan, Y., Helmons, R. L. J., & Schott, D. L. (2022). The Influence of Particle Size on Sliding Wear of a Convex Pattern Surface. Minerals, 12(2), [139]. https://doi.org/10.3390/min12020139.

4.1 Introduction

The handling of bulk solids plays an important role in a variety of industries, such as the mining, agricultural, chemical, and pharmacological industries [155]. For the mining industry, the process of transferring bulk solids leads to surface wear of shovel bucket [156]. The vertical stirred mills are applied widely in mineral industries and the liner wear plays a significant role in the maintenance and operational costs [119]. Severe wear has been found in several locations on bulk handling equipment, for example, silo walls and bottom sections of the transfer chute [7]. For transfer chute, studies show that approximately 82 % of the energy losses are attributed to the bulk material sliding along the bottom of the chute, and 9 % of the losses are due to sliding against the side walls [6]. To reduce the wear caused by the interaction between bulk material (e.g. soil and iron ore) and equipment surface (e.g. shovel bucket and transfer chute), scientists have proposed biological wear-resistant surfaces inspired by the contacts between biological surfaces and the corresponding living environments. Inspired by the bionic design method, a convex pattern surface is introduced [157] and optimized [158] to reduce the sliding wear of the surfaces of bulk solids handing equipment by using a discrete element method (DEM). Many works [91,117,118,143,159–163] have been completed on the investigation of sliding wear caused by bulk material based on the DEM method while studies seldom focus on the influence of particle size on sliding wear. Although the previous studies have shown that the convex pattern surface can significantly reduce sliding wear compared with the plain surface, the effect of particle size is still unknown. The effect of particle size is crucial as the bulk handling equipment transfers various materials with different particle sizes. To bridge this gap, the study aims at the effect of particle size on sliding wear of the bionic surface.

Based on the previous study [158], to investigate the influence of particle size on the sliding wear of the convex pattern surface, a particle scaling technique is applied. Various scaling techniques can be used for DEM, such as exact scaling [164,165], scalping [166], coarse graining [167], hybrid particle-geometric approach [168], and multi-level coarse graining [169].

The exact scaling aims at setting a numerical model that can reproduce the physical phenomena exactly. Three similarity principles, namely geometric, mechanical and dynamic, must be satisfied to meet exact scaling [165]. The system parameters, for instance the acceleration of gravity, can be determined by the basic quantities, for instance length L, density ρ, and time T. As the domain and the particle size scale up together, so the upscaled system has the same number of particles and the same computational costs. For example, the particles and equipment are scaled to experimentally investigate excavating motion characteristic for grabs, reclaimers, and bulldozers [170]. For the scalping technique, the real PSD is scalped at a specific particle diameter, and only the larger particle size fractions are considered in the simulation [171]. For example, the finer fractions of the particles are omitted by replacing them with larger particles.

Another approach is called coarse graining or non-exact scaling [171] and the objective of coarse graining is to reduce computational time by replacing physical particles with representative parcels [167], so upscaled particles can be treated as pseudo-particles [165] or "meso" particles [172]. The key limitation of the particle upscaling factor is the precise representation of a process and therefore difficult to determine in general [171]. For example, the coarse graining technique was used to demonstrate the effect of particle upscaling on material equipment interactions for tool penetration and sliding regimes, and scaling factors 3 and 5 are determined for Hertz-Mindlin with rolling model C and with restricted particle rolling [173]. Another example indicates that an angle of repose test using a lifting cylinder discovers that the repose angle is invariant with respect to the dimensions of the lifting cylinder and the particle size [171]. A confined compression and unconfined loading process revealed that the contact stiffness for loading and unloading scales linearly with particle size and the adhesive force scales very well with the square of the particle size [174]. In addition, coarse graining can also be applied to investigate silo flow [175], granular mixing [176], and the powder die-filling system [177].

The hybrid particle-geometric scaling approach was proposed to scale DEM simulations by isolating the effects of varying particle size and geometric dimensions on bulk properties [168]. This approach successfully extends the coarse graining technique to incorporate elastoplastic behaviour and cohesive forces [168]. Multi-level coarse graining allows the couple of multiple coarse grain levels to overcome the errors caused by the upscaling procedure of the conventional DEM coarse grain model [169] but is difficult to implement.

Although the scaling approach is widely applied to the granular systems mentioned above, the application of the approach on sliding wear caused by bulk material with different sizes is still unstudied. The coarse graining technique is chosen in this research as it is suitable for noncohesive and free-flowing material. The aim of this research is to investigate the influence of particle size on the sliding wear of the convex pattern surface based on the coarse graining approach. The structure of the article is outlined below. In Section 4.3, the effect of particle size on the contact behaviour among particles and wear behaviour for single particle-surface interactions is investigated through the coarse graining technique. Section 4.4 builds a simulation setup to conduct the sliding wear and clarifies the methods used to analyse the simulation results. The comparisons of the simulation results between the convex pattern surface and a plain surface are elaborated from three aspects in Section 4.5. Section 4.6 draws four main conclusions.

4.2 Particle upscaling theory

4.2.1 Contact model

In the coarse graining method, the original particles with radius R are replaced by larger particles with radius $R^{'}$. To guarantee the identical physical behaviour, the coarse-scaled system should keep the consistent energy density and energy density evolution with the original system. Therefore, the gravitational acceleration g, particle density ρ, and velocity v should be kept constant to retain the energy conservative. The motion of each particle follows Newton’s equations and the normal and tangential forces of spring-damping model in EDEM [137] can be denoted as Equations (4.1) and (4.2):

$$F_n = k_n \delta_n^{1/2} - \gamma_n \dot{\delta}_n \tag{4.1}$$

$$F_t = k_t \delta_t - \gamma_t \dot{\delta}_t \tag{4.2}$$

where $k_{n,t}$, $\gamma_{n,t}$, and $\delta_{n,t}$ are stiffness coefficients, damping coefficients, and overlap, respectively, and the subscripts n and t denote normal and tangential direction, respectively.

Applying the Hertzian and non-linear damping [169,178] theories, the stiffness and damping coefficients are formulated as in Equation (4.3):

$$
\begin{aligned}
k_n &= \frac{4}{3}E^*\sqrt{R^*\delta_n} \\
\gamma_n &= -\beta\sqrt{5m^*k_n} \\
k_t &= 8G^*\sqrt{R^*\delta_n} \\
\gamma_t &= -\beta\sqrt{\frac{10}{3}m^*k_t} \\
\beta &= \frac{\ln(e)}{\sqrt{\ln^2(e)+\pi^2}}
\end{aligned}
\tag{4.3}
$$

where E^*, G^*, R^*, and m^* are the equivalent Young's modulus, shear modulus, particle radius, and mass, respectively. e is the coefficient of restitution which is defined as the ratio of the relative particle velocity before and after the collision. Furthermore, a rolling model A, which depends on the relative rotational velocity of two particles, is applied to the motion of particles [146].

Assuming two particles with radii R_i, R_j contacting each other, the equivalent radius R^* can be identified at Equation (4.4):

$$
R^* = \frac{R_iR_j}{R_i+R_j} = \frac{\alpha R_i}{1+\alpha} \tag{4.4}
$$

where $\alpha = R_j/R_i$. Similarly, the equivalent mass is shown in Equation (4.5):

$$
m^* = \frac{m_im_j}{m_i+m_j} = \rho\frac{4\pi R_i^3\alpha^3}{3\left(1+\alpha^3\right)} \tag{4.5}
$$

To substitute Equation (4.1) with the dimensionless mass $m^{*\prime} = m^*/\rho R_i^3$, overlap $\delta'_n = \delta_n/R_i$, velocity $\dot{\delta}'_n = \dot{\delta}_n/v_0$, and acceleration $\ddot{\delta}'_n = \ddot{\delta}_nR_i/v_0^2$ with the reference velocity $v_0 = \sqrt{E^*/\rho}$, the Equation (4.1) can be denoted as Equation (4.6):

$$
m^{*\prime}\ddot{\delta}'_n = \frac{k_n\delta'_n}{R_iE^*} - \frac{\gamma_n\dot{\delta}'_n}{R_i^2\sqrt{\rho E^*}} \tag{4.6}
$$

Therefore, the scaling is based on dimensionless normal overlap for the translational motion of a particle [167] and the dimensional analysis of Equations (4.1) and (4.2) yield the invariant parameters shown in Equation (4.7):

$$
\begin{aligned}
\Pi_1 &= \frac{R_j}{R_i} \\
\Pi_2 &= \frac{k_{n(t)}}{R_iE^*} \\
\Pi_3 &= \frac{\gamma_{n(t)}}{R_i^2\sqrt{\rho E^*}}
\end{aligned}
\tag{4.7}
$$

where π_1 is related to geometric similarity and indicates that the particle needs to be scaled with the constant ratio and π_2 and π_3 require that the $k_{n(t)}/R_i$ and $\gamma_{n(t)}/R_i^2$ be constant, since the velocity and density are scale-invariant.

For the stiffness coefficients in Equation (4.3), it is observed that the stiffness is scaled with the scaling factor s, as $s = R_{CG}/R_o$. R_{CG} and R_o are the coarse grained and original particle radii. The damping coefficient is scaled with s^2 as the m^* and k_n are scaled with s^3 and s, respectively.

Therefore, the Hertz-Mindlin model is termed scale-invariant. Moreover, as the coarse grain has the same rotational energy as the original particles [26], the rolling model remains unchanged.

4.2.2 Archard wear model

Archard wear model [148] is applied to calculate the wear volume caused by the sliding of particles. This wear model has been used widely for bulk handling process, such as the prediction of the wear of mill lifters [179] and local failure prediction of abrasive wear on tipper bodies [150]. Equation (4.8) shows the generalized equation to calculate sliding wear volume:

$$W_v = k \frac{F_n}{H_s} l_s \tag{4.8}$$

where W_v (mm^3), H_s (N/mm^2), k, F_n (N), l_s (mm) indicate the wear volume, hardness of the surface, dimensionless wear coefficient, normal force applied to an equipment surface, and the sliding distance, respectively. Obviously, particle size has no influence on the sliding wear model, so the Archard wear model is scale-invariant to particle size.

4.3 Verification of model scale invariance

4.3.1 Packing

In order to guarantee similar contact behaviour between particles, the microstructure (e.g., particle density and coordination number) and macrostructure (e.g., bulk density and porosity) should be invariant to particle size. The coordination number and porosity are used to investigate the contact behaviour through a packing process [180]. In this process, the particle size is scaled up corresponding to the scale factor, while the dimensions of the simulation domain remain unchanged.

River gravel is used in this research and particle size distributions from scaling factor 1 to 8 are shown in Figure 4.1. For the parameters of the DEM model, please refer to the previous work [158].

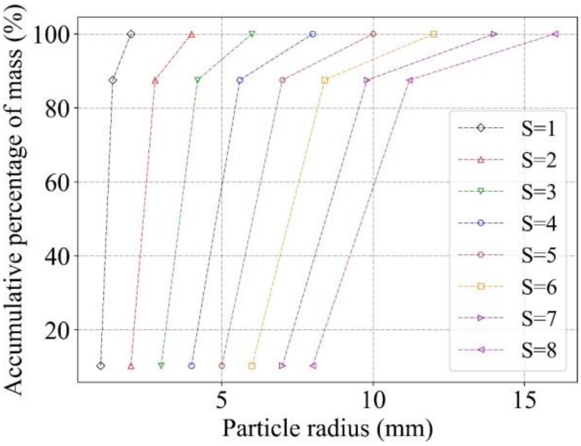

Figure 4.1 Particle size distribution

A square container with the dimension of 300 mm shown in Figure 4.2 is filled with particles to a height of 300 mm. To avoid the wall effect, periodic boundaries, where the particles moving out from one side re-entered into the wall at another side, represented by the dashed line ware used. A bin group with the dimensions of 250 × 250 × $300\ mm^3$ is set in the container, and the depth of each bin is four times of d_{50} (particle diameter corresponding to 50 % of cumulative mass). After being filled, the container is vibrated for 4 s in the y-direction following a formula shown in Equation (4.9) and kept still for 5 s:

$$y = A\sin(\omega t) \tag{4.9}$$

where $A = 0.1d_{50}$ and $\omega = 200$ rad/s.

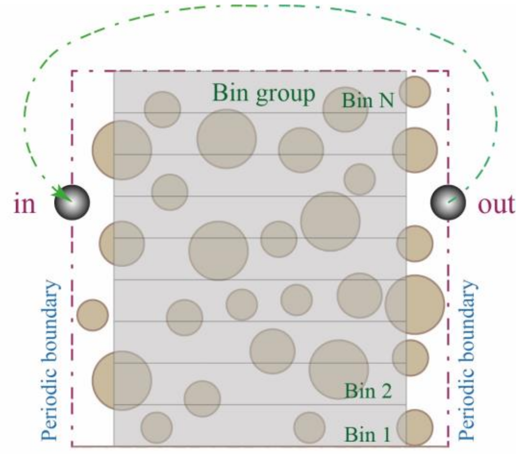

Figure 4.2 Packing container

The coordination number and porosity are investigated under the loose and dense packing states. Figure 4.3 shows the coordination number and the difference between the loose and dense packing. As shown in Figure 4.3 (a), the bottom and second bins indicate the lowest and highest coordination number because of the wall effect and the particle consolidation. The coordination number decreases slowly from the third bin and significantly at the last two bins. In order to eliminate the effect of the wall effect and bulk consolidation, the bottom and top bins are excluded in the following analyses. It can be seen from Figure 4.3 (a) that before vibration, the coordination number for all scaling factors is higher than 5 and lower than 5.6. After the vibration, as shown in Figure 4.3 (b), the coordination number increases by 0.1 to 0.4.

For the porosity, if the center of a particle is located inside a bin, the whole volume of the particle is included. Figure 4.4 depicts the opposite trend to the coordination number. Before vibration, as shown in Figure 4.4 (a), the porosity is lower for lower scaling factors and increases from the second bin to the top bin for each scaling factor. After the vibration indicated from Figure 4.4 (b), the porosity decreases by less than 4 %. The coordination number and porosity imply that the vibration has an obvious influence on the contact among particles, because vibration induced compressed and relaxed effects which are competing with each other on the particles [181].

For both before and after vibration, the coordination number and porosity demonstrate a more obvious fluctuation for a scaling factor higher than 4 compared with those of a scaling factor lower than 4. The reason is that the dimensions of each bin only changes in the depth direction, leading to the reduction of the particle numbers in each bin with the increase of the scaling factor, and therefore, the number of particles in each bin affects the particle contact behaviour.

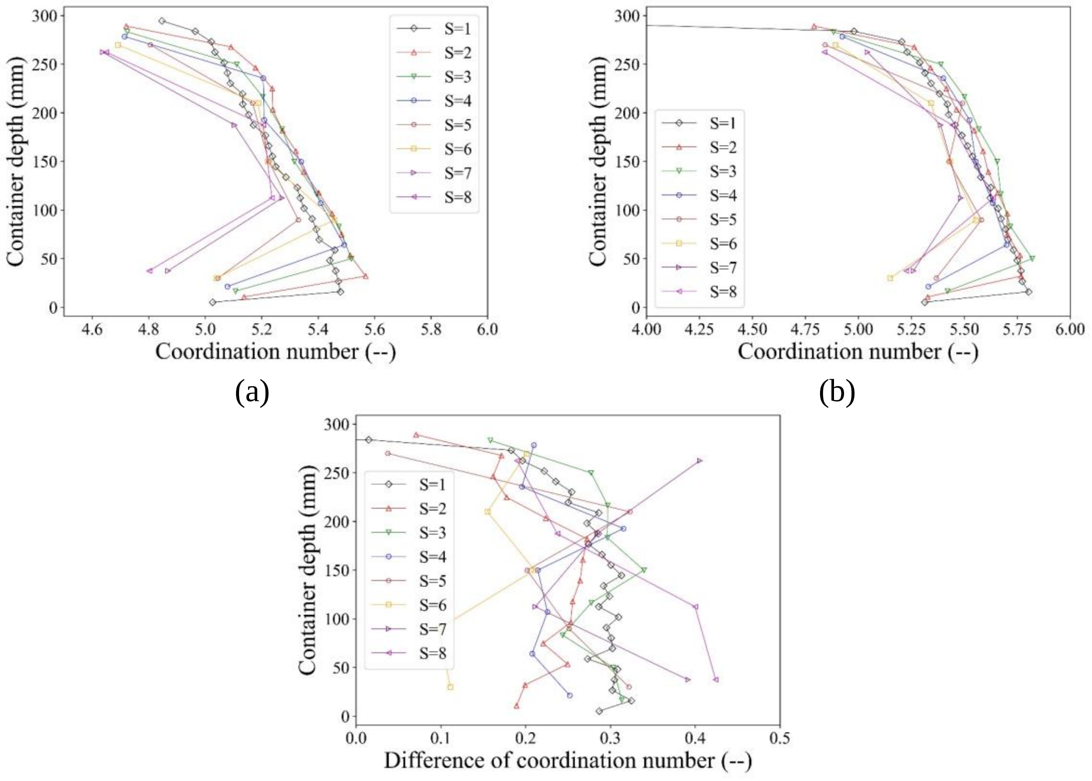

(a) (b)

(c)

Figure 4.3 Coordination number distribution (a) before vibration, (b) after vibration, (c) difference of coordination number after and before vibration

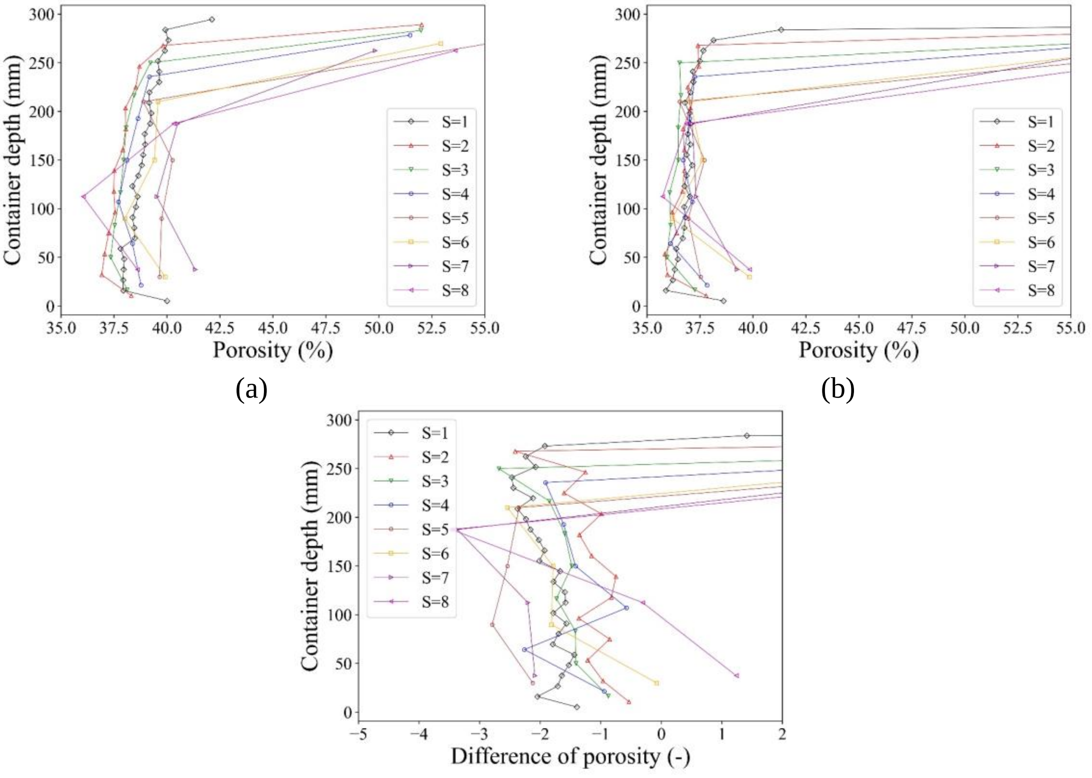

(a) (b)

(c)

Figure 4.4 Porosity distribution (a) before vibration, (b) after vibration, (c) difference of porosity after and before vibration

4.3.2 Pin-on-disc test

The pin-on-disc test, as shown in Figure 4.5, is used to investigate the influence of particle size on sliding wear. A disc with a radius of 100 mm is meshed with 1 mm triangular elements using ANSYS Workbench software package [182]. A particle body force (PBF) obtained by implementing an EDEM API model [137] is applied to the particle to generate the normal force. The particle is constrained with a cylindrical holder located above the disc with a distance of 80 mm from the center of the disc. To eliminate the influence of the gravitational force of the particle, the masses of particles with different radii keep constant by adjusting the particle density. A rotational velocity of 180 deg/s around the central axis is applied to the disc, and the total sliding wear volume is calculated after one round.

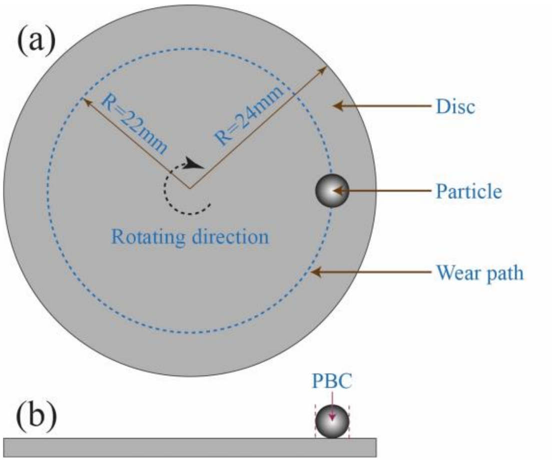

Figure 4.5 Pin-on-disc test setup (a) top view, (b) side view.

Figure 4.6 compares the simulation and theoretical results under the normal force of 1 N and the simulation result with scaling factor of 1 is taken as a reference. The result indicates that the simulation results are comparable with the analytical result with a difference less than 0.6 %. It implies that the particle size has an ignorable effect on sliding wear, which is consistent with a previous study [183].

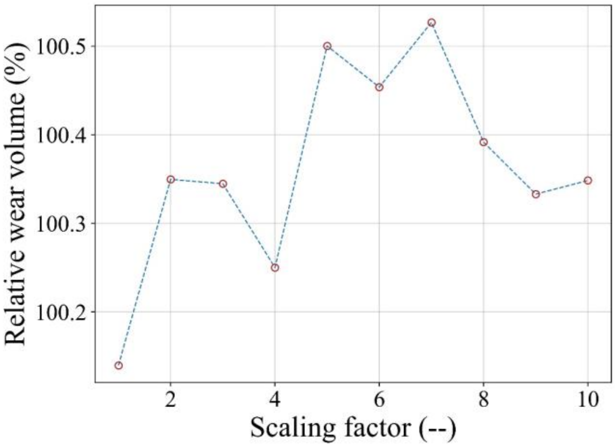

Figure 4.6 Comparison between the simulation results and Archard wear model

4.4 Simulation setup and analysis procedures

4.4.1 Simulation setup

Figure 4.7 shows a particle bed clipped in the sample moving direction. The particle bed contains bulk solids with 40 kg, and the dimensions of the bed are 2000 × 300 mm^2 (length and width). The sample is located at the left central side of the particle bed and traverses in the y-direction with a velocity of 2 m/s. To eliminate the wall effect, a periodic boundary condition is applied to the width direction. A bin group, which is used to investigate the contact behaviour among particles, is built at the particle bed.

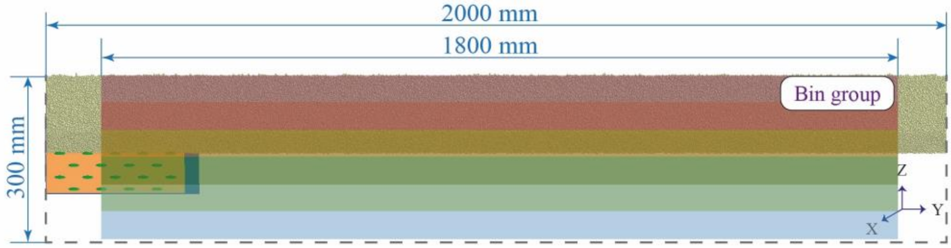

Figure 4.7 Original particle bed

Figure 4.8 illustrates the moving bins used to investigate the bulk flow behaviour. The bins, which are ordered from bottom to the top of the particle bed with the same dimensions of the sample, are attached to and move with the sample. The depth of the bin is related to scaling factor, as listed in Table 4.1. The ratio of bin depth to scaling factor is set as 5 to guarantee the layer of particles for different scaling factors constant. As the particle flow behaves differently, the layers of bins for different scaling factors varied.

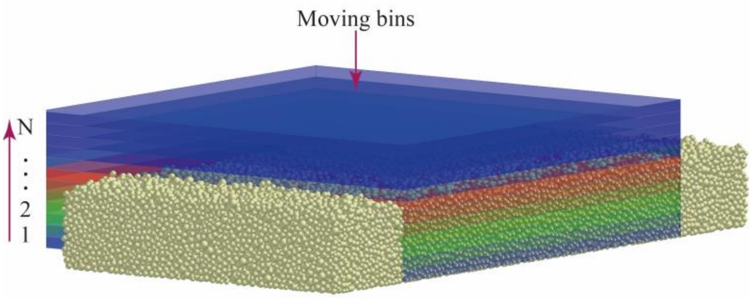

Figure 4.8 Moving bins

Table 4.1 Sizes and layers of the bins

Scaling Factor	d_{50} (mm)	Bin Group Height (mm)	Layers of Bins
1	2.65	60	12
2	5.3	60	6
3	7.95	60	4
4	10.6	80	4
5	13.25	75	3
6	15.9	90	3
7	18.55	105	3
8	21.2	80	2

4.4.2 Analysis procedures

The analysis of the wear results is related to the steady state of the simulation setup. Therefore, the stability of the simulation setup is first evaluated including two aspects, i.e., a stable state and dynamic state. The stable state focuses on the bulk contact behaviour when the sample is located at a specific position. The dynamic state is evaluated by two criteria, the relative velocity of the bulk material and the relative wear rate of the sample.

For the relative velocity of bulk material, it should be noted that only the particles in the moving bins (see Figure 4.8) with the original particle bed height are considered. The relative velocity η is defined as Equation (4.10):

$$\eta = \frac{\bar{v}_{p,y}}{v_s} \times 100\% \tag{4.10}$$

where η, $\overline{v_{p,y}}$ (mm/s), v_s (mm/s) denote the relative velocity, the averaged particle velocity in sample moving direction, and the velocity of the sample, respectively.

The wear rate φ is denoted by Equation (4.11):

$$\varphi = \frac{W_{v,s} - W_{v,s-\Delta s}}{\Delta s} \tag{4.11}$$

where φ (mm^2), Δl (mm), and $W_{v,s} – W_{v,s\text{-}\Delta s}$ (mm) are the wear rate, the displacement increment of the sample, and the wear volume increment, respectively.

The relative wear rate φ_R is used to evaluate the stability of the sliding wear process, which is denoted by Equation (4.12):

$$\varphi_R = \frac{\varphi}{\max(\varphi)} \times 100\% \tag{4.12}$$

where φ_R is the relative wear rate and max(φ) (mm^2) is the maximum wear rate of all simulations. For the convex pattern sample, Equations (4.11) and (4.12) can be used to calculate the wear results of the base and convex pattern, respectively.

After the analysis of the stability of the simulation setup, the sliding wear result is investigated. A relative wear γ is used to compare the wear result, as denoted by Equation (4.13):

$$\gamma = \frac{w_v}{w_{v,\,flat,s=1}} \times 100\% \tag{4.13}$$

where γ, w_v (mm^3), $w_{v,flat,s=1}$ are the relative wear, the wear volumes of the convex pattern sample, and a plain surface, respectively.

4.5 Results

This part consists of the steady-state evaluation, the sliding wear and bulk flow behaviour between the convex pattern and plain surfaces at a steady state.

4.5.1 Steady-state evaluation

4.5.1.1 Contact behaviour

The contact behaviour of the particles is consistent with the packing, including the coordination number and porosity, and the particle bed with a plain surface is taken as a reference. Figure 4.9 indicates that the coordination number of the original particle bed is higher than 5 for the scaling factor 1 to 5 and less than 5 for the rest. After the travel of the sample, the coordination number for all scaling factor is lower than that of the original particle bed. Porosity indicates an opposite trend to the coordination number shown in Figure 4.10, which rises with the increase of scaling factor. Combining both the coordination number and porosity, it implies that the plain surface can influence the contact behaviour among particles by forcing the particle bed to switch from a relative dense state to a loose state.

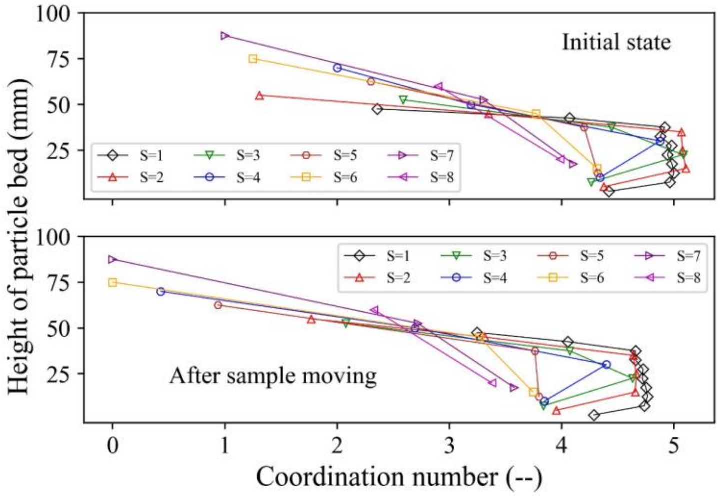

Figure 4.9 Coordination number distribution

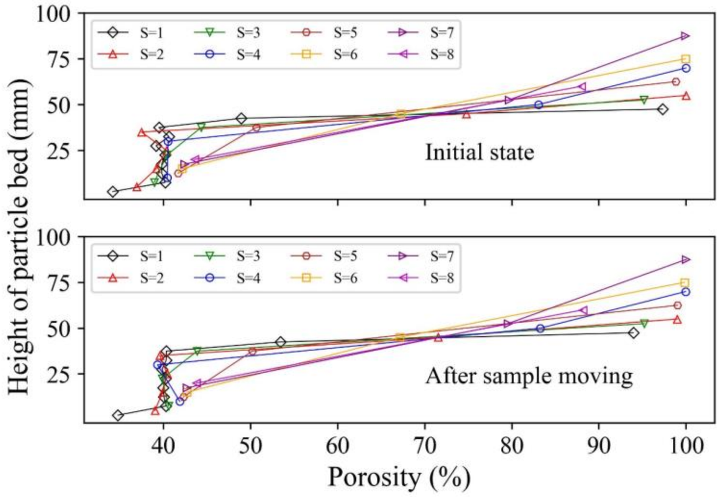

Figure 4.10 Porosity distribution

4.5.1.2 Bulk flow and sliding wear behaviour

The bulk flow and sliding wear behaviour, including the relative velocity of the particles and the relative wear rate, focuses on the moving process of the samples. The plain surface with the original particle bed (scaling factor is 1) is taken as a reference. It should be noted that Figure 4.11 and Figure 4.12 only present four scaling factors (1, 3, 5, and 7) to improve the visibility. As shown in Figure 4.11, the relative velocity, as indicated in Equation (4.10), increases rapidly for the first 700 mm and reaches a steady state until 1700 mm. For the relative wear rate (Equation (4.12)), as shown in Figure 4.12, a periodic fluctuation appears from 100 mm to 1700 mm, and this phenomenon is magnified with the increase of the scaling factor. Combining both

Figure 4.11 and Figure 4.12, the state of the simulations is considered to be stable in the range between 700 mm and 1700 mm.

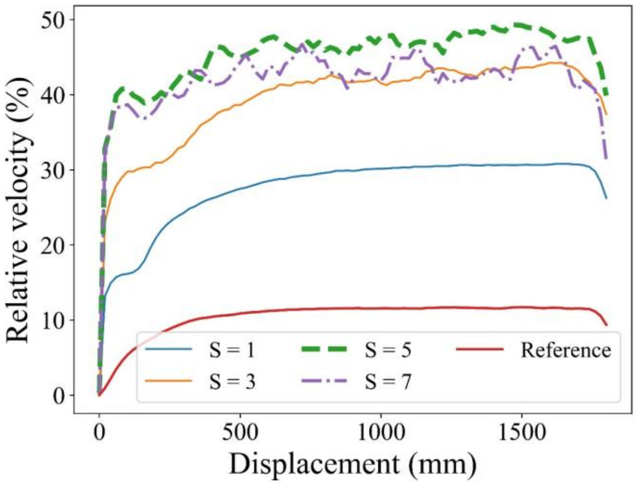

Figure 4.11 Relative velocity of the particles for the convex pattern surface

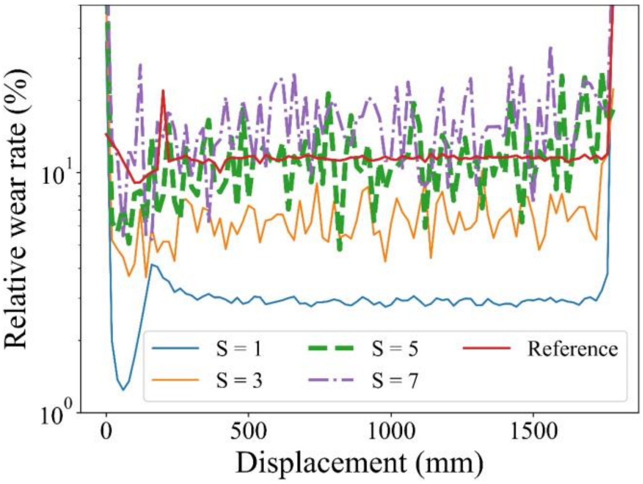

Figure 4.12 Relative wear rate of the convex pattern surface

Figure 4.13 (a) indicates the average relative velocity of the particles. For the particle bed with a plain surface, the relative velocity ranges between 10 % and 15 % of the sample velocity with deviation of ±1.5 %, which means the particle size has a minor effect on bulk flow behaviour. For the convex pattern surface, the relative velocity is higher than that of the plain surface, increasing from 30 % to 45 % from scaling factor 1 to 5 and decreasing to 40 % from 5 to 8, and the standard deviation increases with the increase of the scaling factor from ±0.4 % to ±3.2 %.

Figure 4.13 (b) compares the relative wear rate between the convex pattern and plain surfaces. For the plain surface, the relative wear rate has a similar trend to the relative velocity and the standard deviation increased with the increase of the scaling factor. For the surface of the convex pattern, both the relative wear rate and standard deviation increase with the scaling factor, and the deviation is below than ±5.5 % for all scaling factors.

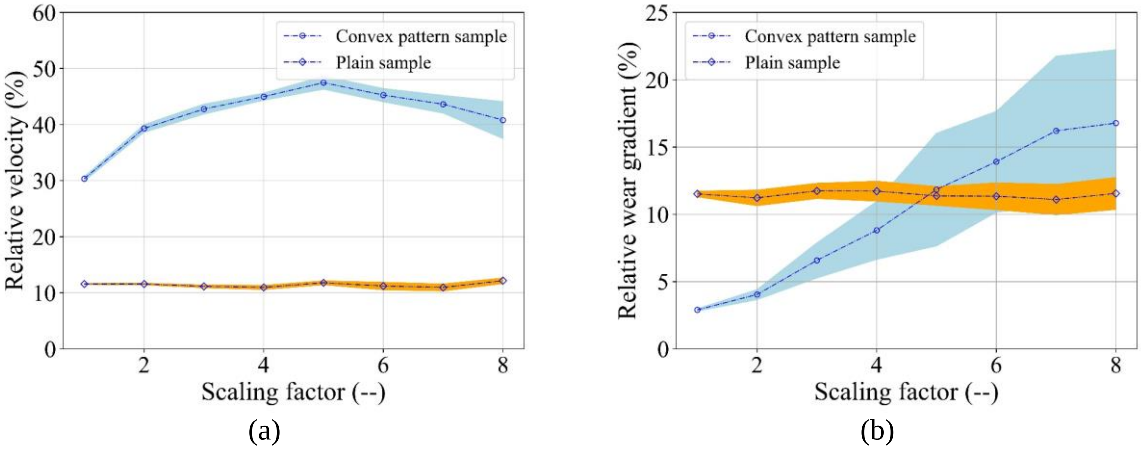

(a) (b)

Figure 4.13 Comparison of the relative velocity and wear rate
(a) relative velocity, (b) relative wear rate

4.5.2 Sliding wear volume

The sliding wear volume is related to the wear volume of a plain surface caused by the original particles. Figure 4.14 shows the relative wear results, and the corresponding fitted models are listed in Equations (4.14) – (4.17). For the plain surface, the particle size hardly affects the sliding wear, as indicated by Equation (4.14). For the convex pattern surface, the total wear has a linear correlation to the particle size, as indicated by Equation (4.15). It can be seen that the convex pattern surface reduces wear compared to the plain surface when the scaling factor is lower than 4. This indicates that the effectiveness of convex pattern surface on wear reduction is related to the particle size.

To analyze the wear distribution, the convex pattern surface is separated into two parts: the base and the convex pattern. As shown in Figure 4.14, the base of the sample, as denoted by Equation (4.16), has a similar trend to the plain surface and the wear is much lower than that of the plain surface. The convex pattern, denoted by Equation (4.17), contains the majority of the sliding wear and linearly relates to the particle size. This means that the base is protected by transferring the sliding wear into the convex pattern.

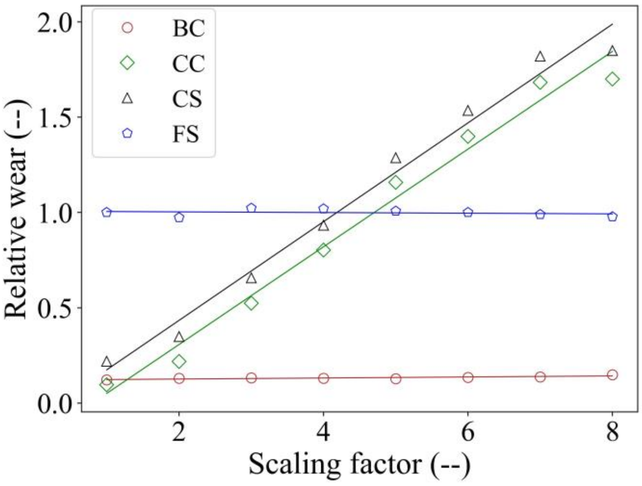

Figure 4.14 Relative wear in relation with scaling factor
(CS: convex pattern surface, FS: plain surface, BC: base of CS, CC: convex part of CS)

$$y_{FS} = 1.01 - 0.002x, R^2 = 0.96 \quad (4.14)$$

$$y_{CS} = -0.08 + 0.26x, R^2 = 0.98 \quad (4.15)$$

$$y_{BC} = 0.12 + 0.003x, R^2 = 0.72 \quad (4.16)$$

$$y_{FS} = 1.01 - 0.002x, R^2 = 0.96 \quad (4.17)$$

Figure 4.15 compares the wear distributions between the plain and convex pattern surfaces for scaling factors 1 and 5. For scaling factor of 1, the wear distribution shown in Figure 4.15 (a) clearly demonstrates that the scratches caused by the sliding of the particles are formed on the plain surface. For the convex pattern surface shown in Figure 4.15 (b), the majority of wear appears at the front part. Wear paths among the convex pattern from front to the back part can be visualized obviously, which indicates that the convex pattern can guide the particles to flow along specific paths. For detailed analysis of the wear distribution, please see the previous study [7].

For a scaling factor of 5, the front part of the plain surface shown in Figure 4.16 (a) displays a larger area with less wear distributed compared to Figure 4.15 (a). For the convex pattern surface, the guiding effect of the convex pattern disappears and the sliding wear is distributed on the whole sample. These phenomena are elaborated based on the particle velocity and angular velocity profiles in Section 5.3.

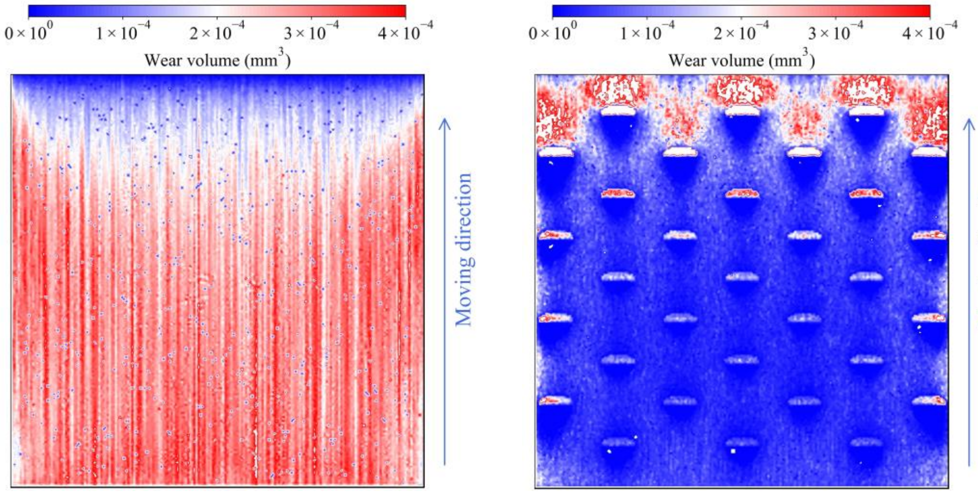

(a) (b)

Figure 4.15 Wear distribution of samples for a scaling factor of 1
(a) plain surface, (b) convex pattern surface

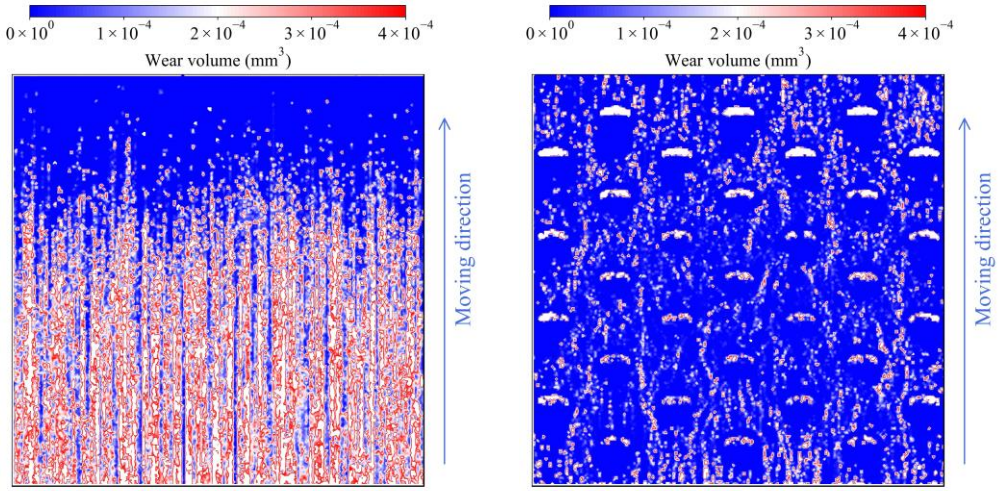

(a) (b)

Figure 4.16 Wear distribution of samples for a scaling factor of 5
(a) plain surface, (b) convex pattern surface

To study the relation between the particle size and the dimensions of the convex, four ratios, which are the projected area, surface area, volume, and equivalent radius, are investigated. For convex, the projected area is defined as the area of a convex projected vertically. The equivalent radius is obtained when taking the convex as a half-sphere. It should be noted that these parameters of particles are based on the values of R_{50} (particle radius corresponding to 50 % of cumulative mass). The four ratios are denoted in Equations (4.18) – (4.21):

$$\alpha_{ER} = R_p \Big/ \sqrt[3]{abh/2} \tag{4.18}$$

$$\alpha_{PA} = R_p^2 \big/ (ab) \tag{4.19}$$

$$\alpha_{SA} = 6R_p^2 \big/ (ab + ah + bh) \tag{4.20}$$

$$\alpha_V = 2R_p^3 \big/ (abh) \tag{4.21}$$

where R_p, a, b, and h are the radius of particle, major radius, minor radius, and height of the convex pattern, respectively. α_{ER}, α_{PA}, α_{SA}, and α_V are the ratios of the equivalent radius, projected area, surface area, and volume of particle to that of the convex pattern, respectively.

Figure 4.17 demonstrates that a scaling factor of 4 is a critical value where the wear results for the plain and convex pattern surfaces are comparable. It can be seen that α_{SA} and α_V have no direct relationship with the sliding wear. α_{ER} and α_{PA} present an obvious correlation with the wear result, which shows that the convex pattern surface can reduce the sliding wear when the ratios are less than 1 and increase the sliding wear when they are higher than 1. Taking the linear relationship between the relative wear and the scaling factor shown in Figure 4.14 into account, it can be seen that the α_{ER} determines the effect of the convex pattern surface on the sliding wear reduction. When α_{ER} is lower than 1, the convex pattern promotes the rolling effect on particles. Otherwise, the particles travel over the convex pattern, becoming the resistance of the movement of particles.

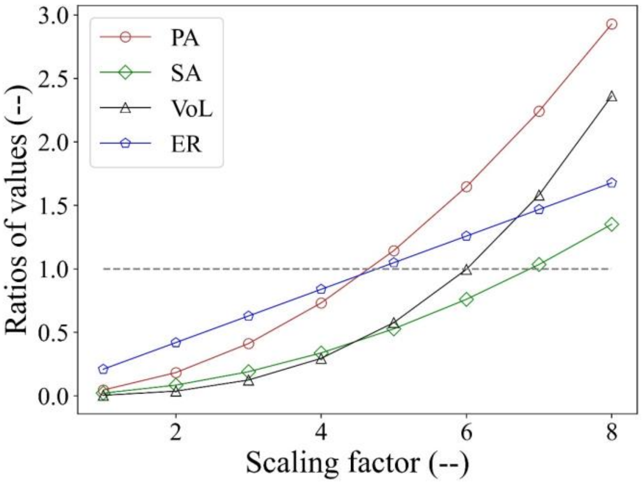

Figure 4.17 Ratios of values between d_{50} related to convex pattern related (PA: projected area, SA: surface area, Vol: volume, ER: equivalent radius)

4.5.3 Bulk flow behaviour

The velocity and angular velocity of the particles are used to indicate the effect of the convex pattern on bulk flow behaviour. It should be noted that the bulk flow behaviour only focuses on the particles in the moving bins shown in Figure 4.8.

4.5.3.1 Velocity behaviour

The velocity profile is displayed by spider charts where the values outside the charts and in the radius direction are the particle bed height and velocity or angular velocity of particles. As the particle size varies, the layer depth listed in Table 4.1, differs for different scaling factors.

The particle velocity in the y-direction indicates the tendency of particles to move with the sample. For a plain surface, as shown in Figure 4.18 (a), the particle velocity for all scaling factors is less than 0.35 m/s and much lower than the sample velocity 2 m/s. This means that the particle size has a minor influence on the particle velocity in the y-direction. Moreover, the particle velocity decreases with the increase in the height of the particle bed as the effect of the sample weakens.

For the convex pattern surface shown in Figure 4.18 (b), the velocity in the bottom bin is higher than 0.9 m/s for all scaling factors. This indicates that the particles at the bottom of the particle bed tend to move with the sample to reduce the sliding distance. This tendency is more obvious for low scaling factors because smaller particles are easier to be guided by the convex pattern. In addition, the effect drops abruptly with the increase of particle bed height.

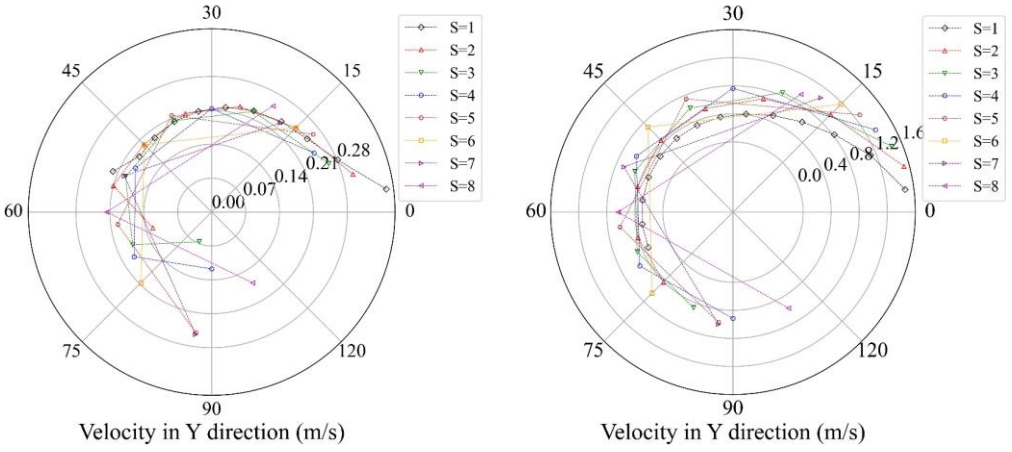

(a) (b)

Figure 4.18 Particle velocity in the y-direction (a) plain surface, (b) convex pattern surface

The velocity of the particles in the Z direction indicates the tendency of the particles to move across layers. For the plain surface shown in Figure 4.19 (a), the velocity of the particles is much lower than that of the surface of the convex pattern shown in Figure 4.19 (b). This means that the plain surface has a weak effect on the movement of particles across bins. For the convex pattern surface, Figure 4.19 (b) demonstrates that the particle velocity increases to a maximum value from the bottom layer and decreases to the top layer for all scaling factors. The velocity at the bottom layer rises with the increase of the scaling factor. This indicates that the larger particles could travel over the convex pattern, while the smaller particles moved around the convex pattern.

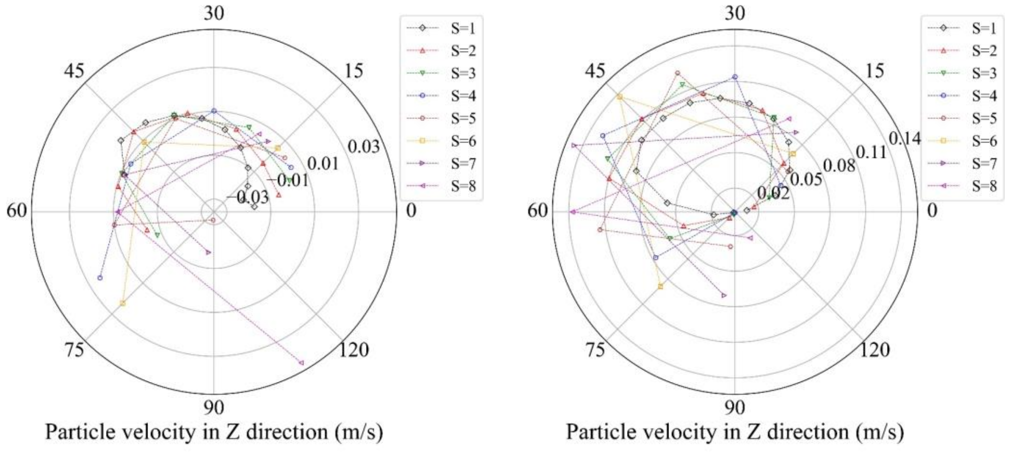

(a) (b)

Figure 4.19 Particle velocity in Z direction (a) plain surface, (b) convex pattern surface

The particle velocity in the X direction showed a tendency of the particles to move sideways. For both the plain and convex pattern surfaces, as shown in Figure 4.20, the particles have no obvious tendency to move sideways for all scaling factors. For each scaling factor, the particles have comparable velocity at all layers, so the effect of the samples on the movement of particles in the X direction can be ignored.

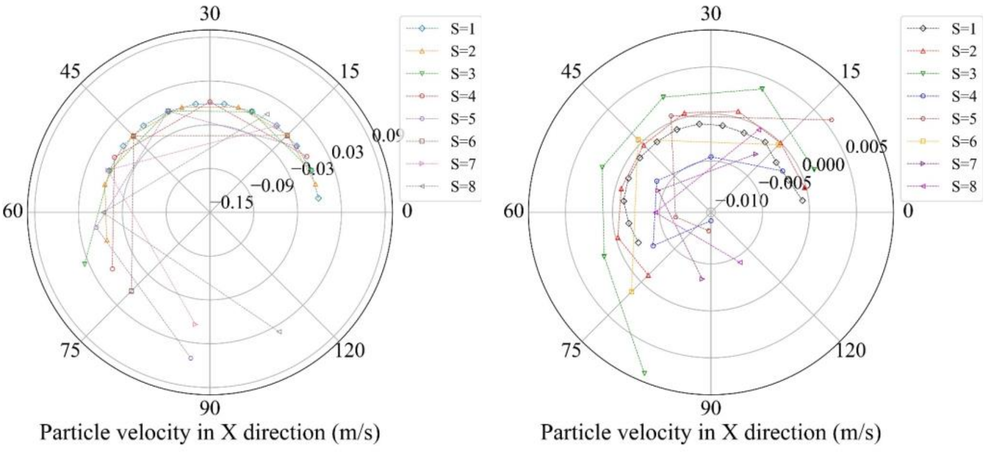

(a) (b)

Figure 4.20 Particle velocity in the X direction (a) plain surface, (b) convex pattern surface

4.5.3.2 Angular velocity behaviour

As the bottom layer reflects the rolling and guiding effect of the convex pattern, the angular velocity focuses on the bottom layer of particles with a bin group shown in Figure 4.21. The depth and width of each bin are related to the scaling factor indicated in Figure 4.8.

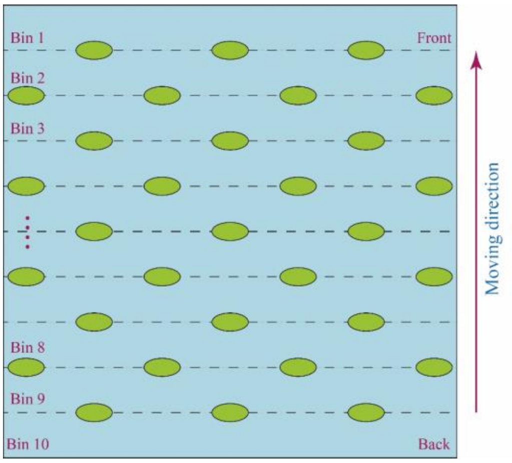

Figure 4.21 Bin groups for the angular velocity

For the plain sample, Figure 4.22 (a) demonstrates that the angular velocity of the particles decreases significantly with the increase of the scaling factor. For each scaling factor, the angular velocity displays two increase-drop periods. First, the angular velocity has a high value at the first bin and drops to a low value at the second. Second, the angular velocity ascends from the second bin to the maximum value and gradually descends to the lowest value until the last bin. The reason relies on that the initial contact between the particles and the sample facilities the rotation of particles. As high angular velocity tends to generate less sliding wear, this phenomenon can explain the lower wear distribution in the front part of the plain sample.

For the convex pattern surface shown in Figure 4.22 (b), the angular velocity is much higher than that of the corresponding plain surface and decreases with the increase of scaling factor. This indicates that the rolling effect of the convex pattern weakens with the increase of particle size. Furthermore, the particles at the front part of the sample have a higher angular velocity compared with those at the back part for all scaling factors, leading to the decreasing rolling effect.

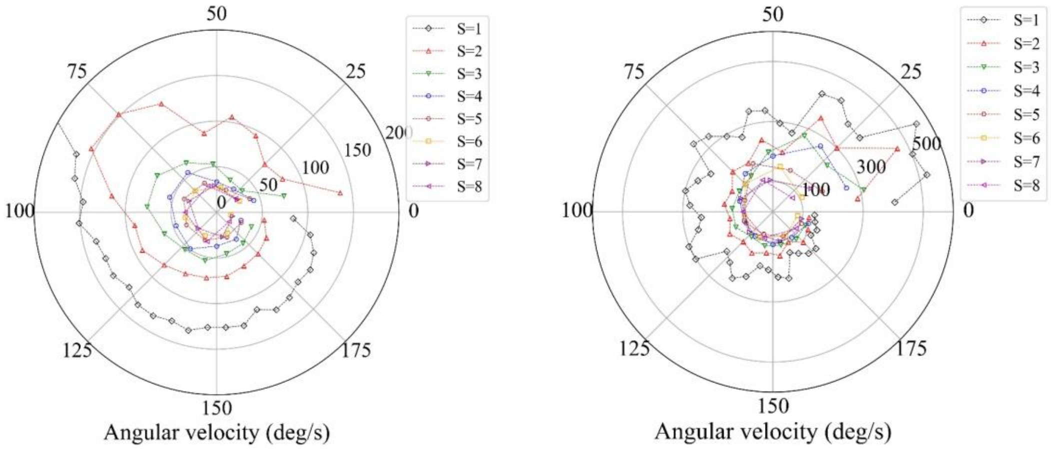

(a) (b)

Figure 4.22 Angular velocity (a) plain surface, (b) convex pattern surface

4.6 Conclusions

This chapter addresses the question:

To what extent can the convex pattern sample reduce wear for different particle size distributions?

This chapter investigates the effect of the particle size on the sliding wear of a convex pattern surface. On the basis of the coarse graining technique, the relationship between the dimensions of the convex pattern and the particle size is clarified and the effect of the convex pattern on the flow behaviour of particles is elaborated.

The simulation system reaches a steady state from 700 mm to 1700 mm. For a plain surface, the particle relative velocity and relative wear rate of the sample are comparable and the corresponding deviations are less than ±0.65 % and ±0.33 %, respectively. For the convex pattern surface, the particle size affects the bulk flow behaviour and relative wear, while the corresponding deviations are less than ±1.2 % and ±5.5 %, respectively.

The particle size has no effect on the sliding wear of the plain surface, while it has a linear correlation with for the convex pattern surface. The majority of the sliding wear of the convex pattern surface occurs on the convex part, and the base of the sample is protected by transferring the sliding wear to the convex.

The convex pattern surface enables to reduce the sliding wear compared with the plain surface when the scaling factor is lower than 4. The ratio (α_{ER}) of the equivalent radius of the convex to the particle radius determines the effect of the convex pattern surface. When α_{ER} is lower than 1, the convex pattern can reduce the sliding wear by altering the flow behaviour of particles. When α_{ER} is higher than 1, particles can traverse across the convex pattern, leading to the resistance of the particles.

The investigated convex pattern surfaces can, in some cases, significantly accelerate the flowing and rolling of particles compared with the plain surface. It should be noted that only the flow behaviour cannot fully reflect the effect of the convex pattern on the sliding wear.

In conclusion, when the relationship between particle size and the dimensions of the convex pattern is carefully considered, the convex pattern surface can reduce the sliding wear significantly. Future research including sliding wear experiments on a circular wear tester to verify the simulation results will be conducted.

5 Pin-on-disc modelling with mesh deformation using DEM*

Chapter 3 obtains an optimal convex pattern sample for the sliding wear reduction and chapter 4 reveals a relation between particle size and wear volume of the sample. However, the study is performed without the consideration of surface deformation. To study the surface deformation, as a benchmark, this chapter models a long-term pin-on-disc test with a short-term numerical model by combining a deformable geometry technique with a discrete element method. This chapter consists of five main sections. Section 5.2 elaborates a geometrical deformation technique integrated with Archard wear model. Section 5.3 clarifies the pin-on-disc test procedures and corresponding results. Section 5.4 obtains a wear coefficient by a scaling technique. Section 5.5 verifies the simulation results by comparing the test results. Section 5.6 draws main conclusions.

---

*This chapter is based on Yan, Y., Helmons, R. L. J., & Schott, D. L. (2022). Pin-on-Disc Modelling with Mesh Deformation Using Discrete Element Method. Materials, 15(5), [1813]. https://doi.org/10.3390/ma15051813.

5.1 Introduction

Bulk solids handling plays a significant role in a range of industries, such as the mining, agricultural, chemical and pharmacology industries [155]. For the mining industry, the process of transferring bulk solids, e.g., iron ore, leads to surface wear of handling equipment. Studies show that approximately 82 % of the energy loss is attributed to the bulk material sliding along the chute bottom and 9 % of the losses due to sliding against the side walls [6]. The sliding wear can be characterised as a relative motion between two solid surfaces in contact under load [184], and long-term wear leads to surface deformation and accelerates the damage of the equipment, resulting in a reduction in lifespan. To reduce the sliding wear of the surfaces of bulk solids handling equipment, a convex pattern surface is proposed [5] and optimised [158] by using the discrete element method (DEM) [185]. However, the deformation of the surface caused by the sliding wear is still unstudied. It is essential to investigate the deformation behaviour of the surface caused by the sliding wear because surface deformation might affect the flow, in turn influencing the wear behaviour of the geometry. Before the analysis of the deformation of the surface caused by bulk material, it is necessary to achieve the modelling of the surface deformation caused by a single particle, so a pin-on-disc test, which is a standard sliding wear test, is applied to the analysis of the surface deformation [184].

In the context of wear evaluation, DEM is a useful approach to predict the wear of equipment caused by bulk material. DEM was developed by Cundall and Strack to model particle systems by tracking the movement of each particle and its interaction with its surroundings over time [185], and it is widely used to design, analyse and optimise bulk material handling systems and equipment for granular materials [135].

On one hand, DEM simulates the wear process without the consideration of geometrical deformation. Cleary et al. [186] first proposed an approach based on DEM to predict the liner wear and distribution of a ball mill using a 2D model for different conditions of rotational velocity. Similarly, Cleary et al. [9,10] evaluated wear in a 3D slice of a mill and performed an evaluation and comparison between wear in tower and pin mills. Recently, Xu et al. [11–13] studied the liner wear of a tumbling mill based on a multiple-level approach, and the numerical model was validated by experimental data. Rojas et al. [190] studied the wear in mining hoppers and obtained comparable results with the measurements. In addition, Kalácska et al. [159], Katinas et al. [163] and Powell et al. [143] studied the wear behaviour of steel used in agricultural tines, wear of soil rapper tin, high speed steel and liner revolution in ball mills based on the discrete element method, respectively. On the other hand, some researchers are interested in surface deformation caused by wear. Kalala et al. [191] applied DEM to estimate adhesion, abrasion and impact wear in dry ball mills with further validation with industrial wear measurement. Esteves et al. [119] compared the industrial vertical stirred mills screw liner wear profile to the measurements after more than 3000 h by using scaling-up procedures for rotational velocities. The predicted wear volumes obtained from the DEM model have a good agreement with the measured results when using a specific velocity. Boemer et al. [142] proposed a generic wear prediction procedure based on the discrete element method for ball mill liners in the cement industry. By obtaining a global wear constant and analysing the mesh size sensitivity, the predicted wear profile can match the measurement through a mesh smoothing technique. Additionally, Schramm et al. [118] modelled a scratch test to study the abrasive material loss at soil tillage and compared it with a cross-section profile.

Although these studies pay attention to the deformation of geometry, the detailed analyses, such as mesh size sensitivity, wear contour matching and wear depth distribution, are still lacking, and these aspects determine the accuracy of the numerical model. Therefore, a pin-on-disc test as a benchmark is applied to this study to compare the long-term laboratory test with a short-term numerical model. Four steps are built to complete the research. First, the geometrical deformation technique combined with a sliding wear model named the Archard wear model is introduced. Second, the procedures and the results of the pin-on-disc test are clarified. Third, the wear coefficient is calibrated, including the mesh size sensitivity, wear depth and wear width distribution analysis and wear contour reconstruction. Fourth, the simulation results including wear contour and wear volume analysis are verified by the test results.

5.2 Materials and methods

5.2.1 DEM with geometrical deformation technique

The surface deformation is modelled by a geometrical deformation technique [117] in EDEM [137] combined with the Archard wear model [148] shown in Figure 5.1. The highlighted part demonstrates the process of calculating wear volume and updating the mesh position of the geometry, as explained below.

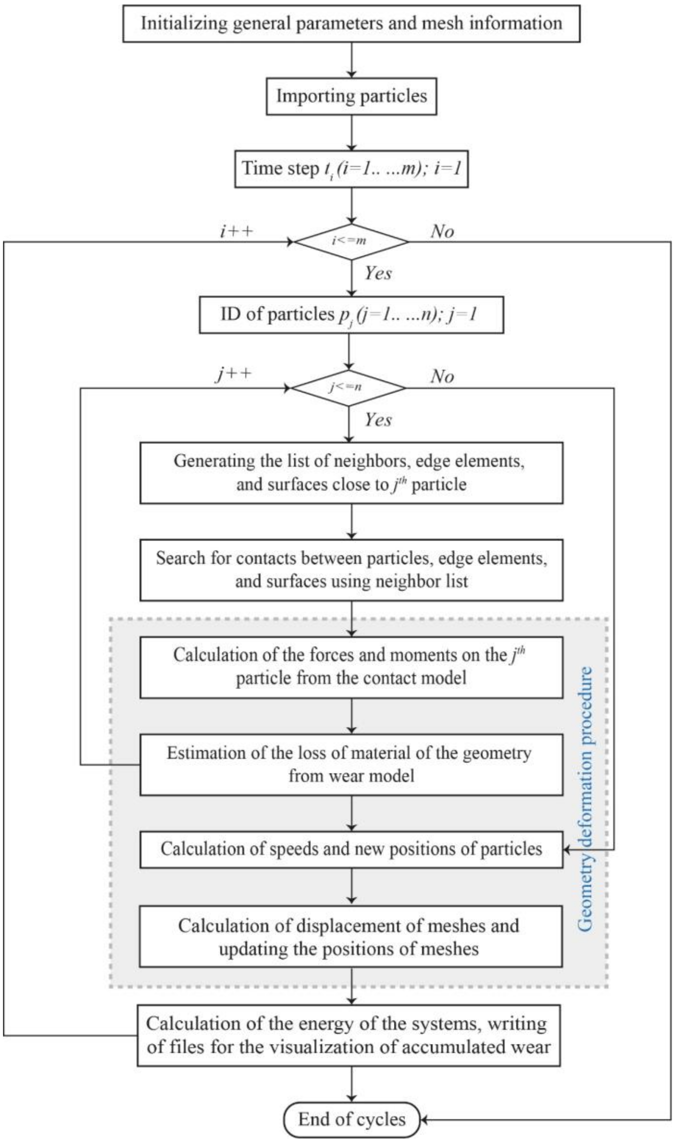

Figure 5.1 Flow chart for calculating wear volume and updating deformation

The Archard wear model is integrated into this technique, as this model is widely used both for particles and geometries, e.g. for evaluating the wear of ballast and abrasive grain [192,193], for predicting the wear of mill lifters [179], and for predicting local failures caused by abrasive wear on tipper bodies [150]. This model has also been successfully applied to evaluate the wear behaviour of the convex pattern surface [158]. It is worth mentioning that particle size is independent from the model and that the particle is considered rigid. The Archard wear model is shown in Equation (5.1):

$$V = k\frac{F_n}{H_s}l_s \tag{5.1}$$

where V (mm^3), H_s (N/mm^2), k, F_n (N), and l_s (mm) are the wear volume, the hardness of the surface, dimensionless wear coefficient, normal force applied to an equipment surface, and is the sliding distance.

Equation (5.1) can be expressed by a derivative formula denoted as Equation (5.2),

$$dV = \frac{kF_n\|v_t\|dt}{H_s} = \alpha_s F_n\|v_t\|dt \tag{5.2}$$

where $\alpha_s = k/H_s$ represents the wear coefficient. dV, $\|v_t\|$, and dt denote the increment of wear volume of the material removed, relative tangential velocity, and time increment, respectively.

The geometry is meshed by triangular meshes using ANSYS Workbench 18.2 software and the sequence of mesh deformation is illustrated in Figure 5.2.

1) The contact between the particle and the mesh elements is detected and the forces are calculated based on the contact model.
2) The loss of the material is evaluated based on the Archard wear model.
3) The new positions of the elements and velocity of the particle are recalculated.
4) The element is displaced in its normal direction.

Therefore, wear loss can be represented by deforming the triangular meshes subjected to abrasive wear.

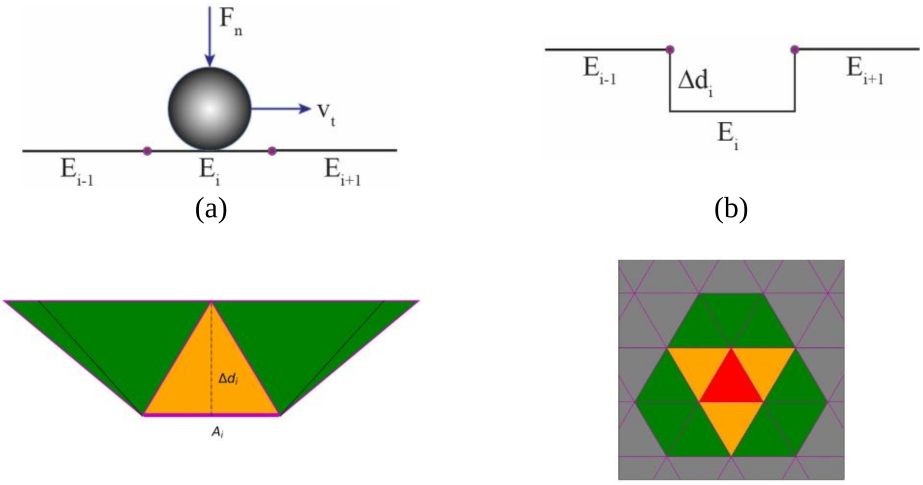

(a) (b)

(c) (d)

Figure 5.2 Mesh deformation procedure (a) particle in contact with the surface E_i of the mesh element, (b) displacement of the mesh element, (c) side view of the interconnection between nodes, and (d) top view of the wear representation

The wear volume of the i^th element at each time step Δt is expressed by Equation (5.3).

$$\Delta V_i = \int_t^{t+h} \alpha_s F_n\|v_t\|dt \approx \alpha_s F_n\|v_t\|\Delta t \tag{5.3}$$

The differential displacement (wear depth) Δd_i for the i^{th} element is related to the element area and the relations are denoted as Equations (5.4) and (5.5),

$$\Delta d_i = \frac{\Delta V_i}{A_i} \tag{5.4}$$

$$A_i = \frac{\left|(p_1 - p_2)\times(p_1 - p_3)\right|}{2} \tag{5.5}$$

where p_1, p_2, p_3, are the positions of a node of a triangular element.

The wear depth $d_i^{t+\Delta t}$ and the new position of nodes of the mesh element $p_k^{t+\Delta t}$ at time $t+\Delta t$ are obtained through Equations (5.6) and (5.7),

$$d_i^{t+\Delta t} = d_i^t + \Delta d_i^t \cdot n_i \tag{5.6}$$

$$p_k^{t+\Delta t} = p_k^t + \Delta d_i^t \cdot n_i \; (k = 1, 2, 3) \tag{5.7}$$

where $\hat{n}_i$ is the normal vector of the element. By interconnecting the common nodes of the element faces, it is possible to obtain continuity in the deformation of the surface, generating a smoothed wear pattern [117]. As the mesh element is in motion, the coordinates of the central point p_c, which represents the position of the i^{th} element, is calculated before obtaining the accumulated wear V_i of the mesh element, as expressed by Equation (5.8).

$$p_{ci} = \frac{p_{1,i} + p_{2,i} + p_{3,i}}{3} \tag{5.8}$$

Then, the wear volume of each element is integrated through Equation (5.9).

$$V_i = V_i + \left|p_{cj}^{t+h} - p_{cj}^t\right| A_i \tag{5.9}$$

The total volume loss of the whole surface is obtained by adding the volume of each element together, as expressed by Equation (5.10).

$$V = \sum_i^n V_i \tag{5.10}$$

5.2.2 Pin-on-disc test setup

Figure 5.3 illustrates a pin-on-disc tribometer [5] that is used to obtain sliding wear loss of a sample by a single particle. The device consists of three main parts: the load which generates normal force over the pin, the pin mounted in a holder and a disc sample which encounters the sliding wear. The pin is located at a position with a distance of 22 mm from the center of the disc, and the radius of which is 40 mm.

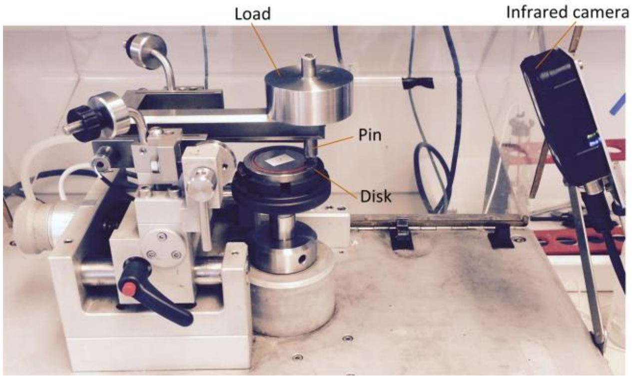

Figure 5.3 Pin-on-disc apparatus [194]

The materials of the disc and the pin are mild steel with 0.3 % carbon and iron ore, respectively, and the parameters of the test are listed in Table 5.1. During particle indentation, the disc surface deforms when the hardness ratio (H_p/H_s) of particle to the surface is higher than 1.2 and approximately maintains a constant when the ratio is higher than 1.9 [48]. Based on a statistical analysis of the hardness [4], the Vickers hardness of the particle and mild steel are 476 ± 9 H_v and 143 ± 4 H_v, respectively, so the ratio is higher than 1.9 and therefore the disc is considered to be deformed with a relatively constant rate. As listed in Table 5.1, the rotational speed is 390.8 deg/s under the normal load of 5 N, so the corresponding sliding distance after 1302.5 revolutions is 180m.

Table 5.1 Parameters of samples and tests

Categories	Parameters	Values
Iron ore	radius (mm)	3
	hardness (H_v)	476 ± 9
	hardness (H_m)	4 – 4.5
	density (kg/mm^3)	4850
Mild steel	density (kg/mm^3)	7932
	hardness (H_v)	143 ± 4
Test	indentation force (N)	5
	rotational speed (deg/s)	390.8
	sliding distance (m)	180
	revolutions (-)	1302.5
	rotational radius (mm)	22

5.3 Pin-on-disc test

Figure 5.4 illustrates the prepared particle, worn disc and obtained wear contours. The polished particle fixed in a metal holder as shown in Figure 5.4 (a) is mounted to the tribometer. Figure 5.4 (b) displays an example of the cross-sectional wear morphology on the mild steel disc after test. During the sliding process, grooves are formed as a result of the removal and displacement of the mild steel. To analyze the wear profile specifically, Figure 5.4 (c) demonstrates three inhomogeneous wear morphologies obtained from three random positions of the wear path. It can be seen that the wear depth and width have ranges of 0.01 – 0.014 mm and 0.65 – 0.8 mm respectively. The wear volume obtained is 0.565 ± 0.089 mm^3 and the corresponding wear coefficient is (6.3 ± 1) × 10^{-13} Pa^{-1}.

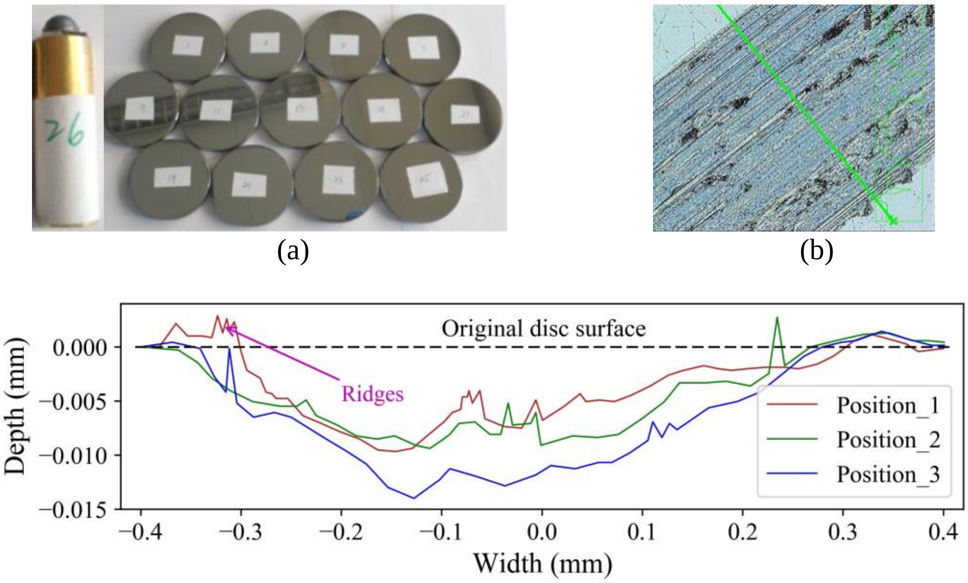

(a) (b)

(c)

Figure 5.4 Wear contour extraction (a) an iron ore with a spherical head, (b) measuring of the cross-section [31], and (c) three wear contours based on the measurement after test

It should be noted that the main mechanisms of the sliding wear on the disc include micro-ploughing and micro-cutting, as mild steel is a ductile material [48]. The micro-ploughing generates ridges of deformed material which are pushed along ahead of the particle, as shown in Figure 5.4 (c). The micro-cutting deflects the material which flows up the front face of the particle to form a chip, so all the material displaced by the particle is removed in the form of chips and generates grooves [17]. Therefore, it should be clarified that the abrasive particle can deform the material in ways that lead to the removal of only part of the material displaced from the groove.

5.4 Calibration of wear coefficient

The coefficient calibration consists of the establishment of the simulation setup, mesh size sensitivity, and the wear result analysis.

5.4.1 Simulation setup

A simplified pin-on-disc modelling setup is illustrated in Figure 5.5. The disc with the radius of 24 mm is meshed by unstructured triangular meshes with specific size. A particle is located at the disc with a distance of 22 mm from the center. A cylindrical holder is used to restrict the movement of the particle in horizontal directions. The normal force of 5 N on the particle is generated by applying a particle body force (PBC) through an API model [137].

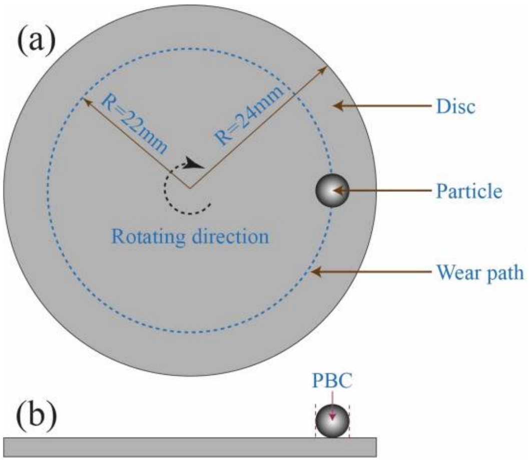

Figure 5.5 Pin-on-disc setup (a) top view, (b) side view

Table 5.2 lists the simulation parameters. The simulation conditions are consistent with the test conditions, except the wear coefficient and rotational speed, which are set as 5×10^{-11} Pa^{-1} and 180 deg/s in the reference simulations.

Table 5.2 Parameters for DEM simulations

Categories	Parameters	Values
Iron ore	radius (mm)	3
	density (kg/mm^3)	4850
	Poisson's ratio	0.24
	shear modulus (GPa)	0.1
Mild steel	density (kg/mm^3)	7932
	Poisson's ratio	0.3
	shear modulus (GPa)	78
	mesh size (mm)	0.1
Contact	coefficient of restitution e	0.4
	coefficient of static friction μ_s	1.0
	coefficient of rolling friction μ_r	0
Conditions	indentation force (N)	5
	rotational speed (deg/s)	180
	rotating radius (mm)	22
	coefficient of sliding wear α_s ($\times 10^{-11}$ Pa^{-1})	5
	time step Δt ($\times 10^{-5}$ s)	1.4

5.4.2 Mesh size sensitivity

Before conducting the mesh size sensitivity analysis, it is essential to clarify the establishment of the wear contours and calculation of the wear volume. To analyze the wear depth and wear width distribution over the wear path, as shown in Figure 5.6 the disc is divided into 360 subparts corresponding to 360 wear contours. The establishment of each contour includes 3 steps. First, the disc is reconstructed based on the coordinates of elements. Second, the disc is sliced into 360 subparts with $\Delta\theta = 0.5$ deg in radian direction of the disc. Third, the coordinates of elements at each subpart are sorted from inner side to outer side of the disc and the sorted coordinates finally form a contour at each position. The contour depth is defined as the maximum displacement of meshes in vertical direction in each wear contour, and the wear width is defined as the width of the opening of each wear contour.

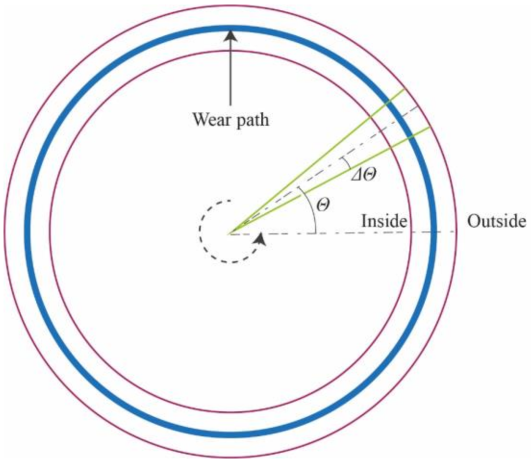

Figure 5.6 Illustration of data extraction

A range of mesh size from 0.1 mm to 1 mm with an increment of 0.1 mm is investigated and the wear coefficient is set as 5×10^{-11} Pa^{-1} as a reference. Figure 5.7 shows the statistical analysis of the wear depth and width of the 360 contours for different mesh size and the error bar denotes the standard deviation. It can be seen that the contour depth decreases with the increase in mesh size, while the wear width shows the opposite trend and increases with the increase in mesh size.

Figure 5.8 shows an example of wear contours after one revolution. To make it more visible, the figure lists six wear contours. Figure 5.8 indicates that the smaller the mesh size, the narrower and deeper the contour. The reason is that the small meshes indicate a fine meshed surface, and the contact between particle and disc involves more meshes as the contact area is constant, so the deformation of the disc influences more meshes and generates a more precise contour. As the test results shown in Figure 5.4 indicate the width of wear contour is around 0.8 mm, to obtain a more precise wear contour, the mesh size is set as 0.1 mm for the following analysis.

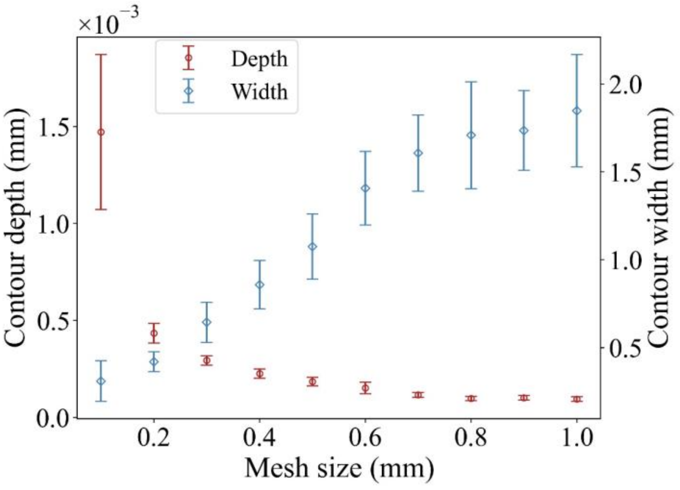

Figure 5.7 Statistical analysis of wear depth and width

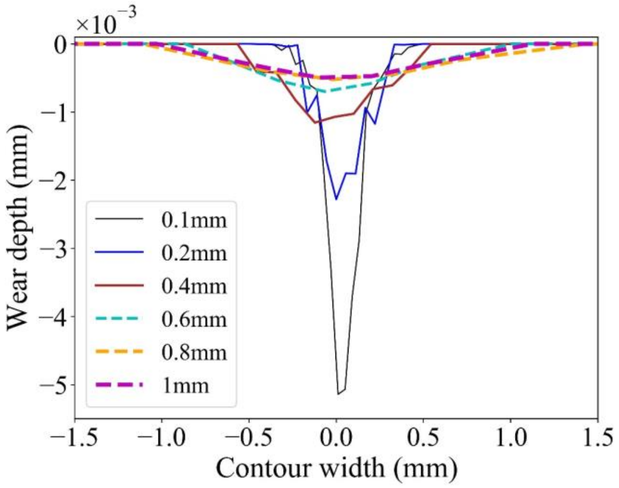

Figure 5.8 Effect of mesh size on wear contour

5.4.3 Calibration analysis

Ten revolutions are used to analyze the wear results of the calibration process, including normal force, wear depth, wear width and wear volume. Figure 5.9 depicts the summary of the distribution of normal force between the particle and disc. The box shows the middle portion of the normal force (first quartile to third quartile). Although the normal forces of the 10 revolutions show different distributions from minimum to maximum values, the mean values are all close to 5 N, as represented by the green marker which means the cumulative force of each revolution is nearly constant. In addition, the normal force contains outliers with high values represented by the circlers. The outliers are caused by the arrangement and deformation of meshes as the deformed meshes influence the contact with particles at the following time steps.

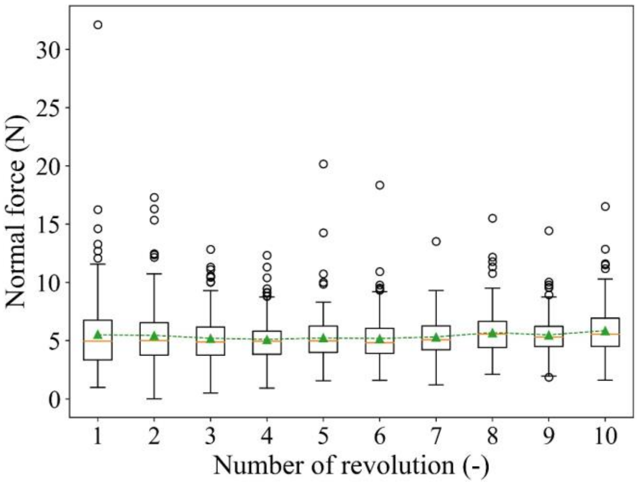

Figure 5.9 Normal force of ten revolutions

Figure 5.10 and Figure 5.11 illustrate the wear depth and wear width distribution of the 360 wear contours of revolution 10, respectively. It can be seen that wear depth and wear width are randomly distributed at a relatively narrow range. The wear depth is at a range from 0.042 mm to 0.07 mm, and the majority of the contours have depths from around 0.05 mm to 0.065 mm. For the wear width distribution, it has a range from 0.8 mm to 1.6 mm and is mainly distributed at a range of 1–1.5 mm.

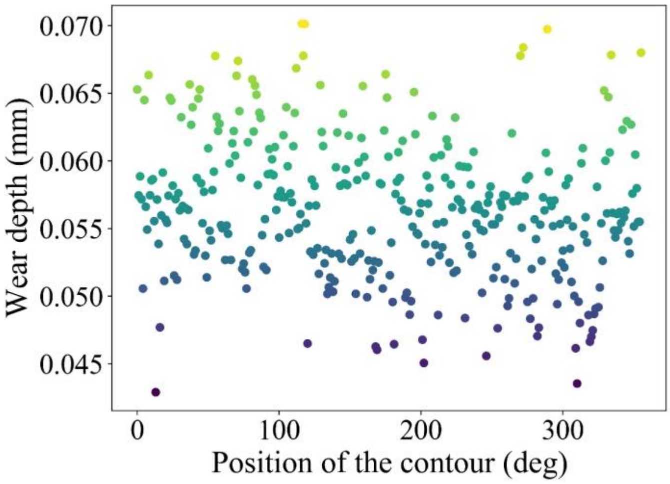

Figure 5.10 Wear depth distribution after 10 revolutions

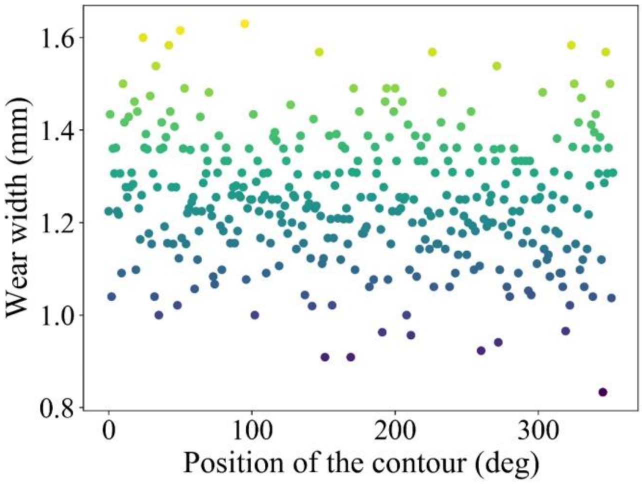

Figure 5.11 Wear width distribution after 10 revolutions

To better understand the distribution of wear depth and wear width, the total 10 revolutions are summarized together based on a normality analysis as shown in Figure 5.12 and Figure 5.13. The Chi-squared test is used to evaluate the normality of the wear depth and wear width distribution based on a 95 % confidence interval. The corresponding p-value is summarized in Table 5.3. If the p-value is high than 0.05, it is assumed that the distribution of the variables is normal.

For both the wear depth and wear width, one outlier appears at the first four and two revolutions with the maximum value as shown in Figure 5.12 and Figure 5.13 and the corresponding p-values are close to 0. The reason is that the initial indentation of the particle causes severe deformation which therefore leads to extreme wear depth and wear width. Starting from revolution 8, the p-value is higher than 0.05 for both the distributions of wear depth and width, which means the wear depth and wear width follow a normal distribution from revolution 8, so it is considered the simulation is at a run-in phase at the first 7 revolutions. This is because with the continuity of the deformation of the surface, the interconnected common nodes have the tendency to generate a smoothed wear pattern after multiple contacts between a particle and meshes [25]. It should be noted that the wear depth increases linearly from R1 to R10 as shown in Figure 5.12 while the increase rate of wear width becomes slow gradually.

This phenomenon can be illustrated by the analysis of the wear contour as shown in Figure 5.14.

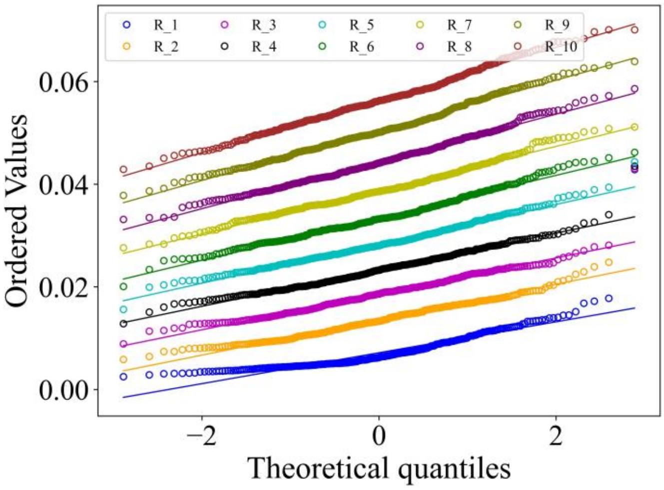

Figure 5.12 Normality analysis of wear depth

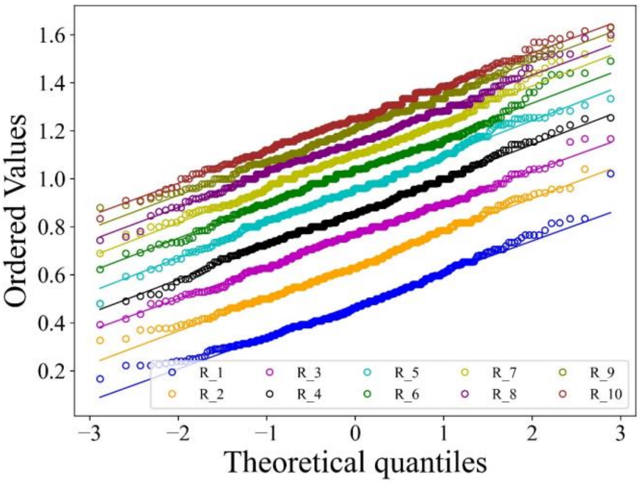

Figure 5.13 Normality analysis of wear width

Table 5.3 Summary of p-value based on Chi-squared test

	R1	R2	R3	R4	R5	R6	R7	R8	R9	R10
Depth	0	0	0	0	0	0.03	0.01	0.11	0.33	0.54
Width	0	0	0.001	0.02	0.04	0.001	0.02	0.21	0.29	0.15

Figure 5.14 shows 24 contours of the last three revolutions at 8 random positions. For the 8 positions, it can be seen that the wear contours extend both in vertical and horizontal directions with the continuation of the revolution. The wear depth and wear width of R10 are at ranges 0.046 – 0.057 mm and 1.0 – 1.5 mm, respectively. For each position, the three wear depths behave similarly from revolution 8 to revolution 10. This is because the relative positions of mesh elements are relatively fixed as a result of the interconnection among nodes, so the deformation of each contour follows a consistent pattern. However, the change in the wear width is not obvious, as the structure of the wear contour as a whole extends in a horizontal

direction, and this means the relation between the number of revolutions and the cross-sectional area or wear volume should be described by a nonlinear relation.

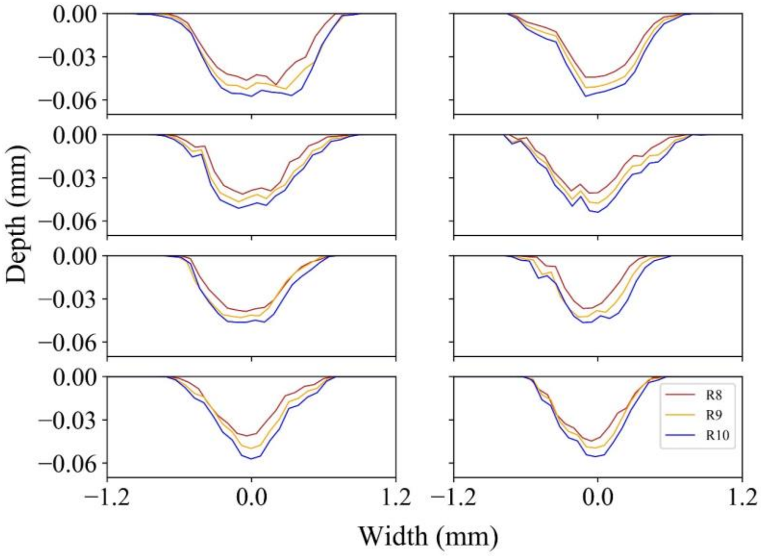

Figure 5.14 Examples of wear contour

Figure 5.15 indicates the correlation between the cumulative wear volume and amount of revolutions corresponding to Equations (5.11) – (5.15). The equations indicate that the wear volume has a quadratic relation with the wear revolution. This can be explained by analyzing the normal force over the disc before and after deformation. For the original surface, as shown in Figure 5.16 (a), the normal force on the original surface exists only in the vertical direction. After deformation, as shown in Figure 5.16 (b), the normal force has a portion in horizontal direction and the horizontal portion generates no influence on the total normal force between particle and disc. As indicated in Figure 5.9 the normal force of each revolution is close to a constant, so the increased wear volume is caused by the horizontal portion. With the wear contour getting wider, the increasing trend of the normal force is enhanced and therefore generates more wear.

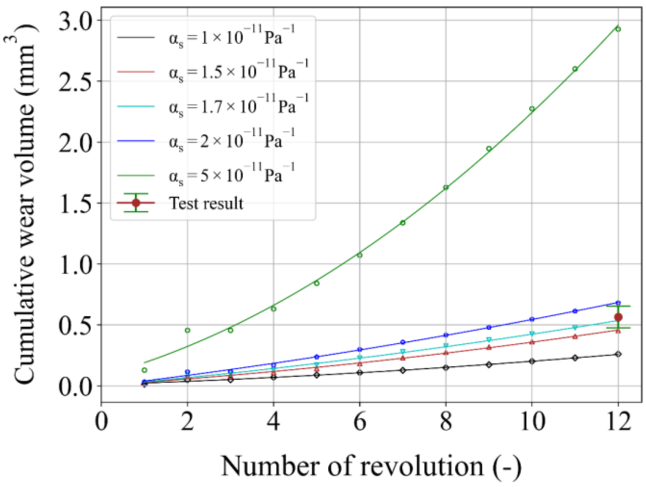

Figure 5.15 Wear volume as a function of revolution

$$y = 0.012x + 0.0008x^2 + 0.001, R^2 = 0.996, \ (\alpha_s = 1 \times 10^{-11} Pa^{-1}) \tag{5.11}$$

$$y = 0.023x + 0.001x^2 + 0.006, R^2 = 0.995, \ (\alpha_s = 1.5 \times 10^{-11} Pa^{-1}) \tag{5.12}$$

$$y = 0.03x + 0.001x^2 + 0.006, R^2 = 0.995, \ (\alpha_s = 1.7 \times 10^{-11} Pa^{-1}) \tag{5.13}$$

$$y = 0.042x + 0.0012x^2 - 0.03, R^2 = 0.997, \ (\alpha_s = 2 \times 10^{-11} Pa^{-1}) \tag{5.14}$$

$$y = 0.098x + 0.011x^2 + 0.08, R^2 = 0.997, \ (\alpha_s = 5 \times 10^{-11} Pa^{-1}) \tag{5.15}$$

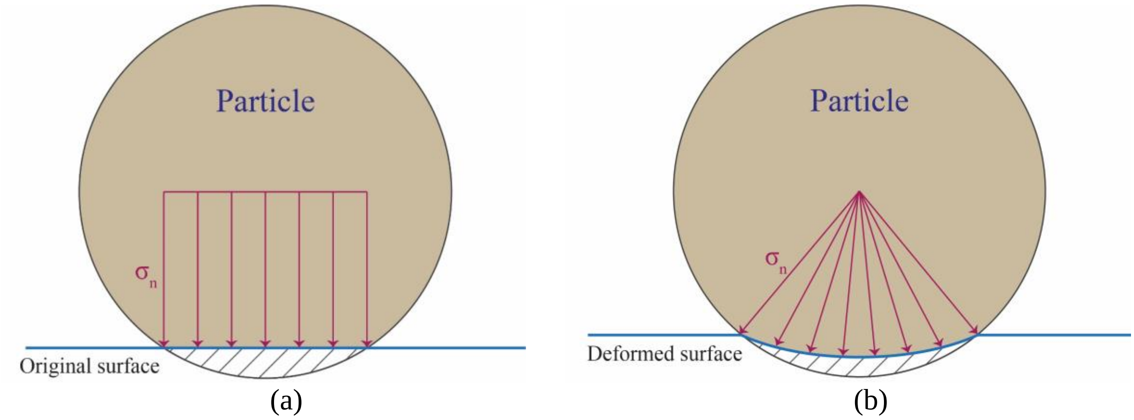

Figure 5.16 Illustration of stress over disc (a) original surface, (b) deformed surface

As presented above, the pin-on-disc numerical model needs 8 revolutions (run-in period) to reach a steady state, so the total 1302.5 revolutions of the test are determined to be modelled with 12 revolutions. As shown in Figure 5.15 , the wear coefficient is changed systematically, and finally the value of 1.7×10^{-11} Pa^{-1} can reach the range of the test volume. It should be noted that with the increase in the wear coefficient, the relation between wear volume and the number of revolutions presents a more obvious accelerating tendency. This is because a higher wear coefficient means a larger surface deformation, and the deformed surface in turn increases the normal force in horizontal direction as shown in Figure 5.16, so that the wear volume of each revolution increases faster.

Furthermore, the other wear coefficient lower than 2×10^{-11} Pa^{-1} can also be selected when the different revolutions are chosen to represent the total test revolutions. For example, 2×10^{-11} Pa^{-1} can be applied when the number of revolutions determined is higher than 12. In total, 9 – 11 revolutions can also represent the total test revolutions when 2×10^{-11} Pa^{-1} is selected. Therefore, the scaling factor, which is defined as the ratio of the number of test revolutions to that of the modelling revolutions, depends on the match of the amount of revolution and the wear coefficient.

5.5 Verification of numerical results

After obtaining the wear coefficient, the simulation results can be verified by comparing the test results, including wear depth and width of the wear contour, wear volume, and wear profile. The corresponding simulation and test results are summarized in Table 5.4. The difference is calculated as the ratio of the absolute difference between the numerical and test results to the test result. The wear depth and wear width of the test results are obtained based on the previous study [4], and the simulation results are based on the statistical analysis of 360 contours as explained in Figure 5.6. It can be seen that the numerical wear volume is close to the test result, with a difference of 6 %.

For the average wear depth and wear width, the numerical results depict 36 % and 34 % differences, respectively. The differences can be explained from four factors [31]: wear volume calculation in model and experiment, wear mechanism, number of samples from experiments, and wear of particle tip in the experiment. First, the calculation of the wear volume is different. For the test, the wear mass is obtained by calculating the wear mass loss. This means the wear volume only counts the dispersed portion. However, the wear process also leads to plastic deformation, and the plastic deformed portion directly affects the wear profile. For the numerical model, the wear volume is directly calculated from the wear profile. Second, the wear mechanisms are different. For the test, the geometry is mainly deformed by micro-cutting and micro-ploughing (plastic deformation), so a portion of the deformed geometry generates wear loss. This is why the ridges are formed as shown in Figure 5.4 (c). For the numerical model, the deformation of the meshes only occurs in the normal direction of mesh element and all the deformation is considered as wear loss. Third, the number of samples for the calculation of wear depth and width has enormous difference. The test results of the wear depth and wear width are only based on three contours and the randomness of the sample selection causes deviation when compared with the whole wear profile. However, 360 wear contours are extracted from the numerical model. Fourth, the tip of the iron ore in the test is worn off and therefore the contact area changes, so the corresponding wear width and depth changes. This situation is avoided in the simulations.

Table 5.4 Summary of numerical and test results

	Wear Depth (mm)	Wear Width (mm)	Wear Volume (mm^3)
Test result	0.014	0.8	0.565
Numerical result	0.019	1.07	0.532
Difference	36 %	34 %	6 %

Figure 5.17 presents the reconstructed deformed disc. It can be seen that the sliding of the particle forms a relatively smooth profile around the disc, except for several highly deformed spots ranging 90° - 120°. The reason is that the normal force at each revolution appears to be high value shown in Figure 5.9 and these normal forces lead to extreme deformation. For the cross-section of the wear profile at each degree, the wear depth has the highest value at the middle and decreases toward the two sides gradually. Figure 5.17 shows that an extremely deformed contour presents at the original position of the disc, which is because the initial indentation of the particle causes the severe deformation. This is reasonable, as this extreme deformation verifies the appearance of an outlier in the distribution of wear depth and wear area, as shown in Figure 5.12 and Figure 5.13.

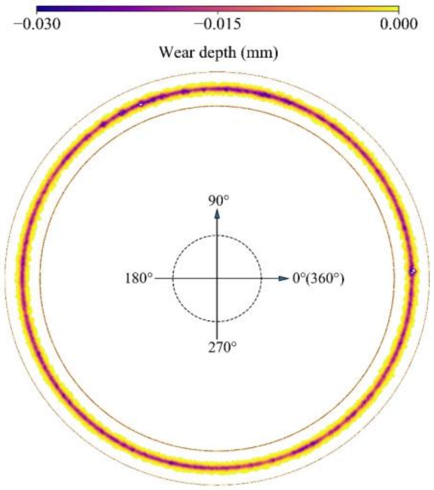

Figure 5.17 Wear profile

To compare the wear contour with the test, three wear contours are extracted randomly from the wear profile, as shown in Figure 5.18. It indicates that the width and depth of the contours are higher and deeper than those of the test contours, while the contours are similar in shape. The results show that by properly scaling up the wear coefficient and selecting the mesh size, the long-term or long-distance laboratory test can be modelled by a short-term or short-distance numerical model with an acceptable deviation.

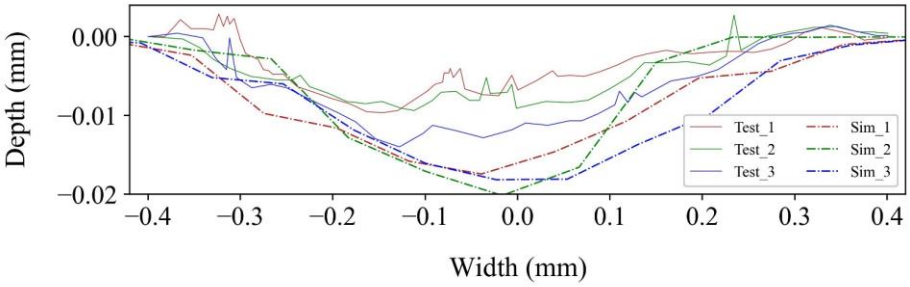

Figure 5.18 Wear contour comparison

5.6 Conclusions

This chapter addresses the question:

In what way can the surface deformation caused by sliding of a single particle be modelled?

A standard sliding wear process, pin-on-disc test, is investigated to indicate that a long-term or long-distance laboratory test can be modelled by a short-term or short-distance numerical model. This numerical model is built by combining the Archard wear model with a deformable geometry technique. The wear results, including wear contour and wear volume, are evaluated statistically with different mesh sizes. Three wear properties (i.e., wear depth, wear width and wear volume) are compared with the test results.

For the sliding of a particle with the radius of 3 mm, the mesh size of the disc is set as 0.1 mm. The wear contour indicates that the mesh size from 0.1 mm to 1 mm has a significant effect on the wear profile. The coarser mesh generates wider and shallower contours, while a fine mesh can obtain comparable wear contour with test results. This is because the contact between particle and disc involves more meshes for the surface with fine meshes, so the deformation of the disc evolves more meshes and generates a more precise contour.

For the geometrical deformation technique, the wear path reaches a relatively steady state from the eighth revolutions. It is verified that the wear depths and wear widths of the wear contours follow normal distributions after a run-in phase because of the self-smoothing effect of the interconnected common nodes of the mesh elements.

The wear coefficient is calibrated by comparing the wear volume between simulation and test results, and the wear volume has a quadratic relation with the number of revolutions. The wear volume of the test accurately predicts the simulation results with the minimum number of revolutions when the wear coefficient is lower than 2×10^{-11} Pa^{-1}. For different wear coefficients, the wear volumes correspond to different quadratic relations. The lower the wear coefficient, the weaker the tendency of the quadratic relation.

To obtain comparable wear results, the minimum number of revolutions is determined as eight, and the corresponding maximum scaling factor, which is defined as the ratio of the number of test revolutions to that of the modelling revolution, is 162.8. By scaling up the wear coefficient and properly selecting the mesh size, the long-term laboratory pin-on-disc test can be modelled by a short-term numerical model. This scaling effect can significantly save computational time and improve efficiency with promising calculation precision.

In this chapter, the presented methodology was successfully demonstrated on a single material combination and can be used for different material combinations. To establish a numerical model for the deformation of other material combinations, the corresponding tests and simulations should be performed.

6 Surface deformation of a convex pattern surface*

Chapter 5 indicates that a long-term single particle-surface contact, namely pin-on-disc test, can be modelled by a short-term numerical model when implementing a scaling factor. This chapter applies the scaling factor to predict the deformation of a convex pattern sample due to bulk material. Section 6.2 describes the wear experiment procedures and compares the wear behaviour between a plain and a convex pattern sample. Section 6.3 introduces the numerical model and evaluates the stability of the model. Section 6.4 investigates the wear behaviour of the sample, including the wear volume, wear distribution, and surface deformation reconstruction, and contact behaviour, including particle flow behaviour and normal force distribution. Section 6.5 concludes the main findings.

---

*This chapter is based on Yan, Y., Helmons, R., Carr, M., Wheeler, C., & Schott, D. “Surface deformation of A Convex Pattern Surface Using DEM with Deformable Geometry Technique”. Submitted to Powder Technology.

6.1 Introduction

Bulk solids handling plays a significant role in many different industries, such as the mining, agricultural, chemical, and pharmaceutical industries [155]. In the mining industry, the process of transferring bulk solids such as iron ore leads to surface wear of handling equipment. Studies show that approximately 82 % of the energy loss is attributed to the bulk material sliding along the bottom of the chute, while 9 % of the loss is due to the material sliding against the side walls [6]. Sliding wear can be characterized as a relative motion between two solid surfaces in contact under load [184], and long-term wear leads to surface deformation and accelerates damage to the equipment, reducing its lifespan. To reduce sliding wear affecting the surfaces of bulk solids handling equipment, a convex pattern surface is proposed [157] and optimized [158] by using the discrete element method (DEM) [134].

In the context of wear evaluation, DEM is a useful approach to predicting equipment wear caused by bulk material. On the one hand, DEM models predicted wear without considering geometrical deformation. This method is widely used to predict the linear wear and distribution of a ball mill [186–188], tumbling mill [141,189,195], mining hoppers [190], agricultural tines [159], and soil rapper tin [163]. On the other hand, many researchers are interested in surface deformation caused by the contact with bulk material. Kalala and Moys [191] applied DEM to estimate adhesion, abrasion, and impact wear in dry ball mills, using industrial wear measurements for further validation. Esteves et al. [119] compared the wear profile of the screw liner used in industrial vertical stirred mills to the measurements after more than 3000 h by using scaling-up procedures. The simulation was performed for a 1:10 reduced scale geometry and applied different scale-up methodologies for rotational velocity. The wear volumes obtained from the DEM model agree closely with the measured results at a specific velocity. Boemer and Ponthot [142] proposed a generic wear prediction procedure based on DEM for ball mill liners in the cement industry. By obtaining a global wear constant and analysing the mesh size sensitivity both in 1D and 2D, the predicted wear profile can be matched to measurements through a mesh smoothing technique. Additionally, Schramm et al. [118] modelled a scratch test to study abrasive material loss caused by soil tillage and compared it with a cross-section profile.

It must be noted, however, that these surface deformation studies are limited to smooth or regular geometrical shapes. For a non-smooth convex pattern surface used to reduce sliding wear, it is essential to model the deformation of this sample, as this may influence its ability to reduce sliding wear. To study the deformation caused by sliding wear, a pin-on-disc test was performed [5] as a benchmark and modelled [196] using DEM by implementing a geometrical deformation technique [117]. This test was used to verify the numerical results by comparing wear contour and wear volume with the test results, which implies that the geometrical deformation technique makes it possible model the surface deformation caused by a single contact. However, the deformation of the convex pattern sample due to wear is not revealed at the bulk level.

The aim of this study is to investigate to what extent the convex pattern sample continues to reduce sliding wear compared to a plain sample. The study consists of five steps. First, the wear experiment is performed in a circular wear tester. Second, a numerical DEM model is developed and the stability of the model is evaluated. Third, the numerical model is benchmarked with the result of the experiment, and the wear behaviour and contact behaviour with particles of the convex pattern sample are analyzed. Besides, the main findings and conclusions are shared.

6.2 Wear experiments

6.2.1 Experiment setup

It should be noted that the sample is distinct to the optimal obtained in Chapter 3. As the dimensions of the test sample is limited to 100 mm by 100 mm, the optimal sample would only present two columns, which hardly alters the flow behaviour of particle. Therefore, the second best design R9 from Table 3.8 is selected as a reference. To analyse the wear distribution, the sample is split into 5 columns (with Col_1 indicating column 1) along the bulk flow direction, and each convex element is labelled separately, moving from the inner side to the outer side of the sample. For example, the first convex element in the first column is labelled as C11.

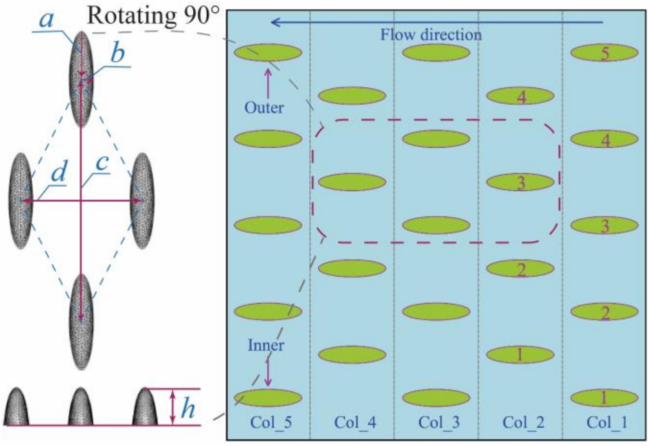

Figure 6.1 Convex pattern sample (a=8 mm, b=2 mm, c=40 mm, d=20 mm, h=6 mm)

The convex pattern and plain samples are tested in an improved circular wear tester to make it possible to test a submerged sample in addition to the traditional face-down sample. The test rig is shown in Figure 6.2 and has the following features:

1) The outer and inner radii of the rotating annular bed are 500 mm and 290 mm, respectively.
2) By inclining the test specimen at a small angle in the bulk flow direction, evenly distributed wear over the entire surface of the test specimen can be obtained.
3) A test specimen holder for easy placement of a standard sample (Figure 6.2 (b)).
4) A consolidator is used to level the surface of the wear media before they are presented to the test specimen.
5) Two wear samples (face-down and submerged), representing two wear scenarios, can be tested at the same time.

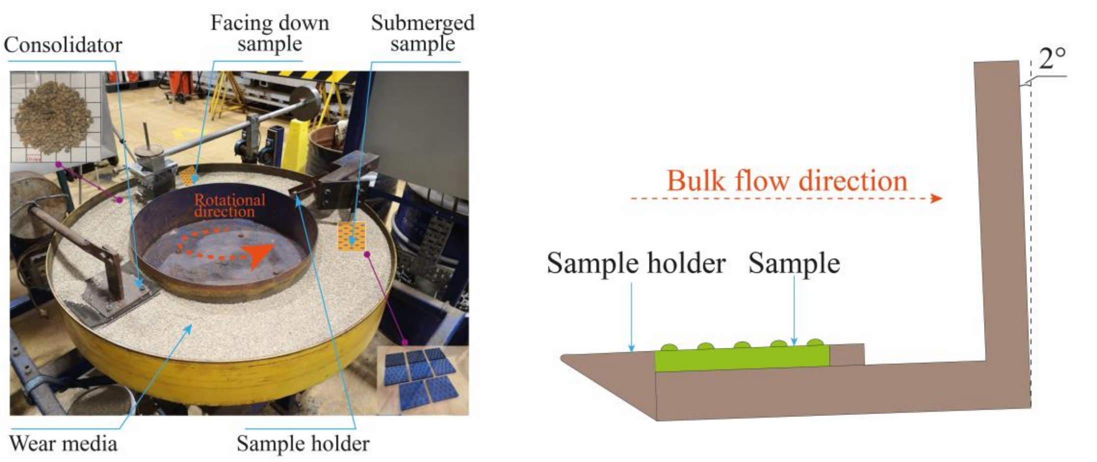

(a) (b)

Figure 6.2 Wear tester (a) Improved circular wear tester holding a traditional face-down sample and a submerged sample [197], (b) submerged sample holder with inclined sample

Table 6.1 lists the test parameters and sample properties. The test specimen is made from polyethylene (PE), which is designed to meet the full range of material flow, friction and wear challenges associated with bulk material. In addition, this material makes it possible to achieve sufficient material wear within a reasonable testing period. The specimen is mounted at a depth of 85 mm with an incline angle of 2 degrees.

The tester has a rotational velocity of 1.52 rad/s. Based on the dimensions of the tester, the speed at the centre of the sample is 0.6 m/s, resulting in test distance of 2.16 km per hour. The specimen is weighed by an electronic balance with 0.001g precision and is scanned every 8 hours by the Creaform HandySCAN 300 laser scanner with 0.02 mm accuracy. As the wear loss of the plain sample follows a linear correlation with the test period [197], the plain sample is tested 56 hours to cut experimental time. To ensure sufficient deformation on the convexes, the convex pattern sample is continued to be tested to 184 hours.

Table 6.1 Summary of test parameters

Categories	Parameters	Values
Wear medium	Bulk density (kg/m^3)	1455
	Particle size d_{50} (mm)	2.65
	Particle shape	Irregular
	Moisture content	0.6 %
Wear sample properties	Material type	SIMONA PE1000
	Ductility	ductile
	Density (kg/m^3)	930
	Shore hardness (D scale)	62
Operational conditions	Submerged depth (mm)	85
	Normal pressure (kPa)	1.2
	Inclination angle (deg)	2
	Rotational velocity (rad/s)	1.52
	Test interval (h)	8

6.2.2 Wear contour reconstruction

To analyse the deformation of the sample, the wear contours are reconstructed based on point clouds from 3D scanning and the detailed procedures are demonstrated in Figure 6.3.

1) The sample is scanned to formulate a point cloud where the coordinates of each point are saved.
2) The orientation of the sample is confirmed based on a marker on the sample by importing the point cloud into Meshlab.
3) The point cloud of individual convex are extracted based on the location of the convex at the sample, and Python is used to process the data points from this step.
4) The data points of wear contour are extracted from the point cloud of individual convex.
5) The data points are visualized by rotating 2 degrees to consist with the inclination of the sample on the tester.

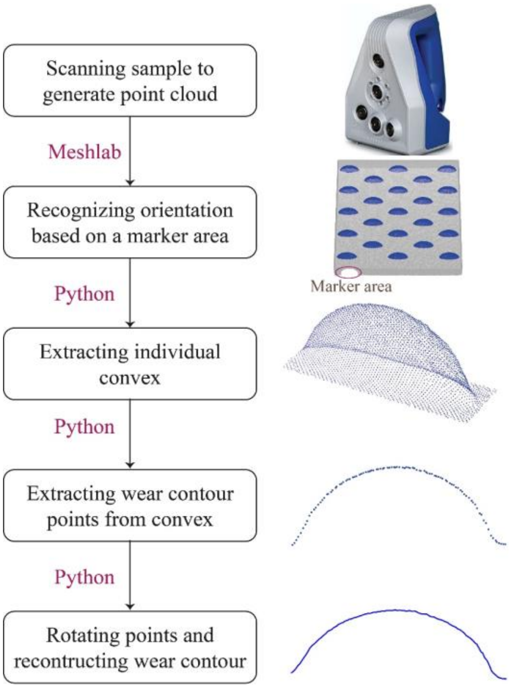

Figure 6.3 Procedure of wear contour reconstruction

6.2.3 Experimental results

Continuing on from the previous study [158], this study focuses on the submerged sample. Figure 6.4 compares the wear volume loss of a plain and convex pattern sample. After 56 hours of testing, the plain and the convex pattern sample generated 145.2 mm^3 and 82.8 mm^3 of volume loss, respectively. Compared to the plain sample, the convex pattern sample reduces wear by 43 %. There is a linear correlation between wear volume and test time for both the plain sample and the convex pattern sample and the corresponding regression models have high coefficient of determination ($R^2 > 0.99$), as shown in Figure 6.4. The wear volume is fitted with a linear equation, as wear volume increases by 17.9 ± 1.7 mm^3 and 10.2 ± 1.2 mm^3 at each time interval for the plain and convex pattern sample, respectively. Besides, operational conditions are kept consistent and the deformation of the sample has a minor effect on flow behaviour, so it is reasonable to assume that the wear rate is constant in this time period.

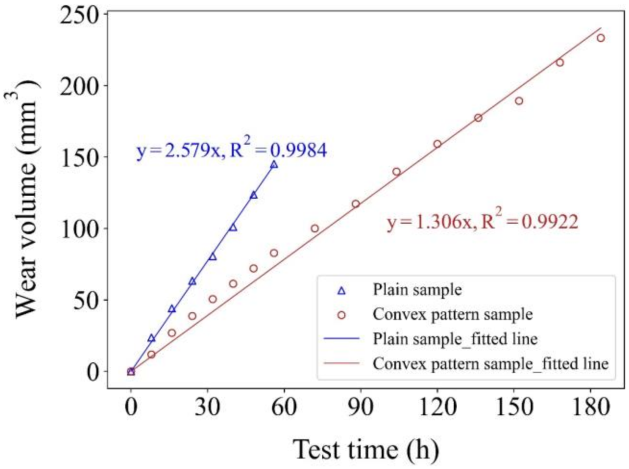

Figure 6.4 Wear volume comparison between plain and convex pattern samples from experiments

Furthermore, the wear contour was reconstructed to evaluate the deformation behaviour of the convex pattern. Figure 6.5 compares the extracted wear contours from the point clouds. The C11, C13, and C15 are taken as references and the reasons are explained in Section 6.4.2.2. The maximum deformations in vertical direction are 0.34 mm, 0.30 mm, and 0.35 mm for these three convexes, respectively. From the side view, it can be seen that the three convex elements deform in similar ways where the front part of the convex displays more obvious deformation than the back part as the front part initializes the contact with particles. From the front view, the deformations are manifested differently depending on the location of the convex element on the sample. For C11, the inner side deforms more heavily than the outer side, while C15, on the other hand, shows more severe deformation on the outer side. Overall, C11 and C15 indicate severer deformation than C13 as these convexes are located at the sides of the sample.

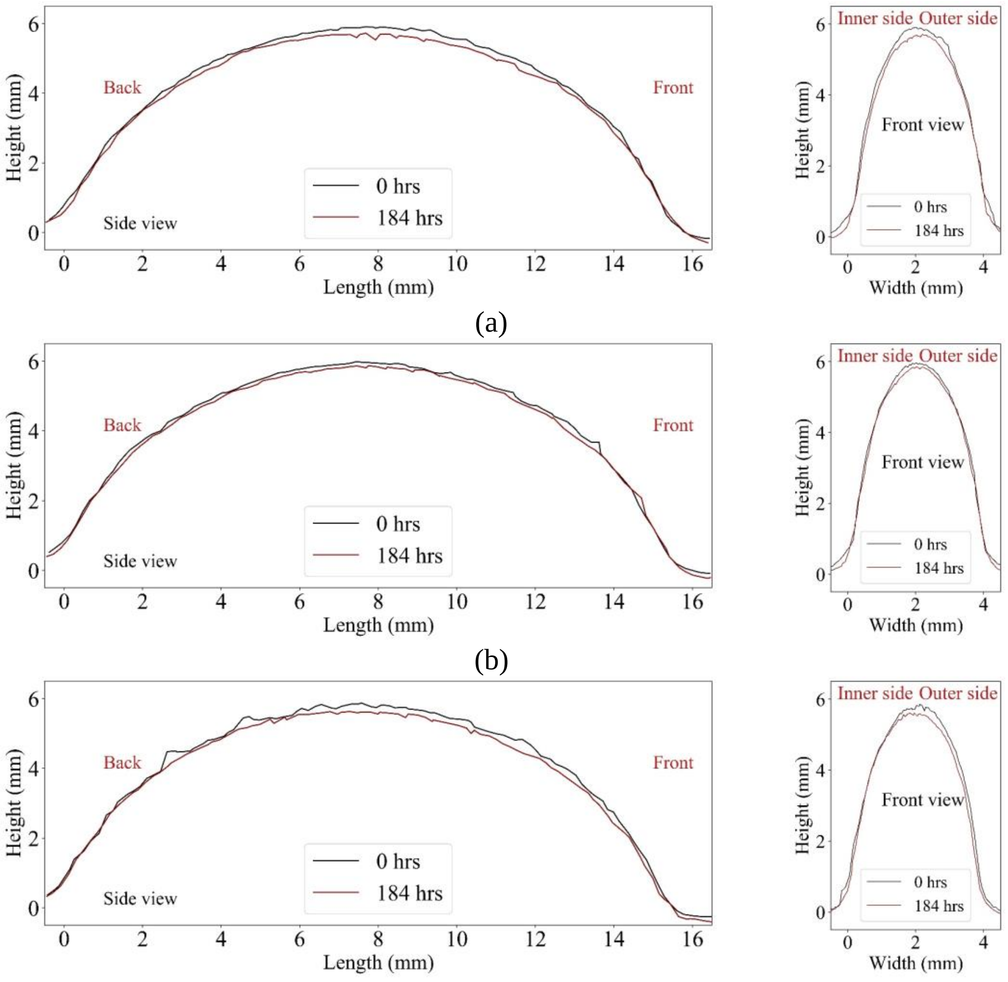

(a)

(b)

(c)

Figure 6.5 Convex deformation from experiments (a) C11, (b) C13, (c) C15

6.3 Numerical model

6.3.1 Numerical model setup

The DEM simulation setup is shown in Figure 6.6. To cut computational costs, cylindrical boundaries with 150 degrees are used which allow particles flowing out from one side to re-enter from another side at the corresponding locations. The particle size is scaled up by 3, as the previous study shows that particle size has a minor effect on the sliding wear of the plain sample [198]. A consolidator similar to the one used in the experiment setup is applied to flatten the particle bed. The test sample is located at a depth of 90 mm in the particle bed at a 2-degree incline. The particle bed has a rotational rate of 90 deg/s, which means that a 150-degree revolution takes 1.67 seconds. For other parameters used in the numerical model, see the previous study [158].

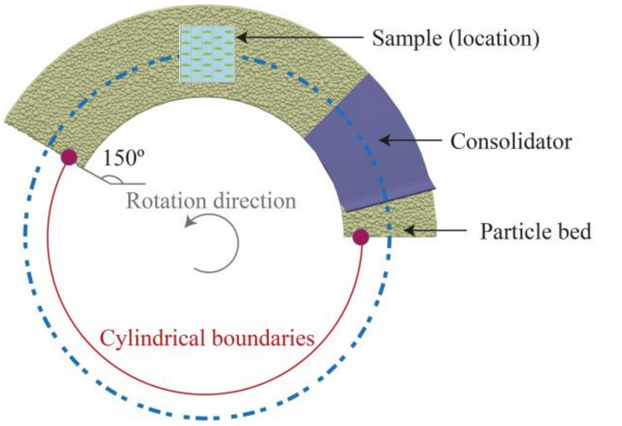

(a)

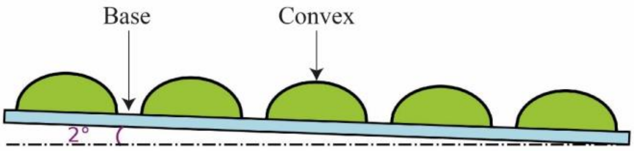

(b)

Figure 6.6 Simulation setup
(a) particle bed settings, (b) inclination angle of sample

6.3.2 Stability evaluation

The material flow in the numerical model should reach a stable state before the sample deformation is modelled. The stability of the system is evaluated by three criteria, including particle velocity, particle bed height, and wear rate. The particle velocity and particle bed height demonstrate the particle flow behaviour and the wear rate indicates the wear behaviour of a sample. The coefficient of variation (CoV), as expressed by Equation (6.1), is used to estimate the variability of the criteria:

$$C_V = \frac{\sigma}{\mu} \tag{6.1}$$

where C_V, σ, and μ are coefficient of variation, standard deviation of each revolution, and the mean value at each revolution, respectively.

Figure 6.7 depicts the CoV of the three evaluation criteria. It should be noted that the particle flow behaviour is based on the particles over the sample. The coefficients of the three criteria drop after the first revolution before stabilizing. For the particle flow behaviour, the particle bed height and particle velocity demonstrate a small fluctuation, which indicates that the particles flow smoothly after a transition period. For the wear rate, the convex pattern sample shows relatively high variation, which remains between 5.7 % and 8.0 % from revolution 6 onwards. Based on the evaluation of the coefficients, the numerical system reaches a stable state after 6 revolutions.

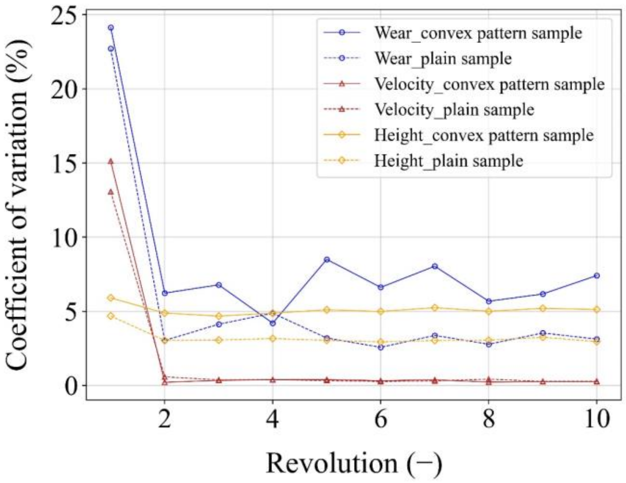

Figure 6.7 Stability evaluation of the numerical model (Wear, velocity, and height represent sample wear rate, particle velocity, and particle bed height, respectively.)

6.4 Numerical result analysis

6.4.1 Benchmark of numerical model

Based on previous study [196], the finer the mesh, the more precisely we can estimate surface deformation. However, if the convex pattern sample is meshed with fine mesh (e.g., 0.1 mm), the total amount of elements exceeds 2.5 million, leading to unpractical computation times. To help cut computation time, the effect of mesh size on wear behaviour is investigated.

Figure 6.8 compares the relative wear volumes of the samples with mesh size from 0.1mm to 1mm after two revolutions. The wear volume of the plain sample with mesh size of 0.1mm is set as a reference value. The average relative wear volumes are 97.9 ± 1.8 % and 56.9 ± 2.8 % for the plain and convex pattern samples, respectively. Quantitatively, the mesh size has a negligible effect on wear volume.

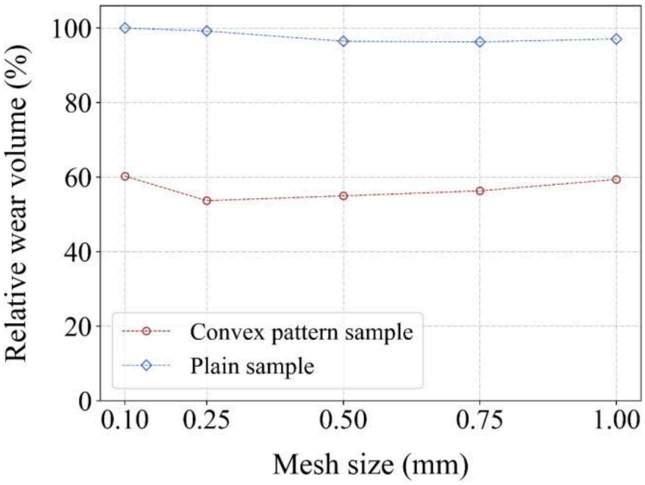

Figure 6.8 Effect of mesh size on wear volume

For the wear contour, convex element C15 is selected, as shown in Figure 6.1, since it suffers the most severe wear, as mentioned in Section 6.4.2.1. Figure 6.9 shows the effect of mesh size on surface deformation of the convex element after two revolutions. As can be seen from the side view, the deformation is concentrated mainly around the front part of the convex, since this part is in direct contact with the bulk flow. The front view shows that the outer side of the convex element undergoes severe deformation. Combining the side and front views of the wear contours, it demonstrates that the surface undergoes similar deformations with different mesh sizes. As mesh size has a minor effect on wear in both quantitative and qualitative terms, it is set at 1mm.

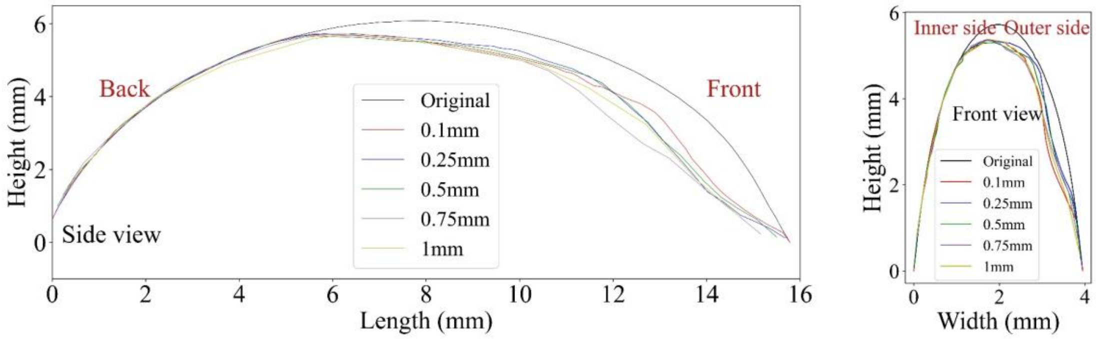

(a) (b)

Figure 6.9 Effect of mesh size on surface deformation (a) side view, (b) front view

It is assumed that, after the material flow reaches a stable state, the total 56 hours (8 intervals) of laboratory testing can be modelled in 2 revolutions by applying a scaling factor [196]. As a benchmark, the wear volume of a plain sample with particle scaling factor is set at 3 and compared with the wear volume of the test result. If the wear volume of the plain sample is comparable to that of the test result, the wear coefficient can be determined [196]. Figure 6.10 compares the wear volume between the experimental and the numerical results for a wear coefficient of 5×10^{-9} Pa^{-1} in the numerical model. For the plain sample, the wear volumes of the test and the numerical model are 145.16 mm^3 and 154.06 mm^3, respectively, with a difference of 5.8 %. Because of this small difference, the wear coefficient is chosen for the following simulations.

Particles with scaling factor 1, 2, and 4 are investigated to test the validity of the numerical model. Figure 6.10 shows that particle size has a minor effect on the wear volume of the plain sample, with a fluctuation of 14 %, because of the wall effect that occurs when applying a coarse graining technique. The wear volume of the convex pattern sample is lower than that of the plain sample and it increases with particle size. The relation between particle size and wear volume of both the plain and convex pattern samples is consistent with the previous study [198].

For a particle scaling factor of 1, the convex pattern sample reduces wear volume by 68.9 % and 43.0 % in the simulation and the experiments, respectively. There are two reasons for this. First, the numerical model only applies a sliding wear model, while the experiment comprises multiple coexistent wear modes, such as wear caused by rolling particles. Second, the particles are irregular in the experiments, but they are simplified and spherical in simulations. The angular particles tend to accelerate surface deformation, as stress is concentrated at the corners of the particles.

A scaling factor is defined by the ratio of the total distance of the experiment to that of the simulation. Based on the operational testing conditions listed in Table 6.1, the total sliding distances of the experiment and the simulation are 84.6 km and 2.142 m, so the scaling factor is set at 40000.

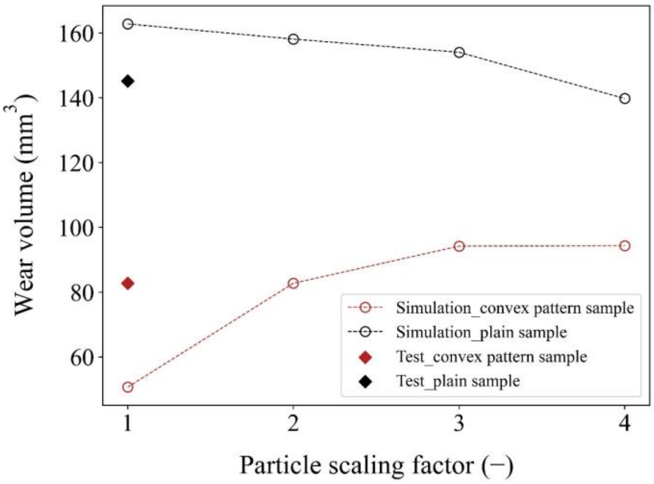

Figure 6.10 Benchmark test comparison

6.4.2 Wear behaviour comparison

6.4.2.1 Wear volume

To demonstrate to what extent the deformed convex sample continues to reduce sliding wear compared to a plain sample, the deformation model does not terminate until it encounters a convergence problem due to mesh distortion [142]. With the wear coefficient of 5×10^{-9} Pa^{-1}, the model is valid for the first 17 revolutions, with the corresponding wear result being shown in Figure 6.11. The wear volume of a plain sample with a particle scaling factor of 1 is set as a reference. Figure 6.11 indicates that the wear volume of the plain sample is higher than that of the convex pattern sample and increases linearly, while the convex pattern sample has a quadratic trend. The equations under Equations (6.2) - (6.6) indicate that the higher the particle scaling factor, the more obvious the quadratic trend becomes.

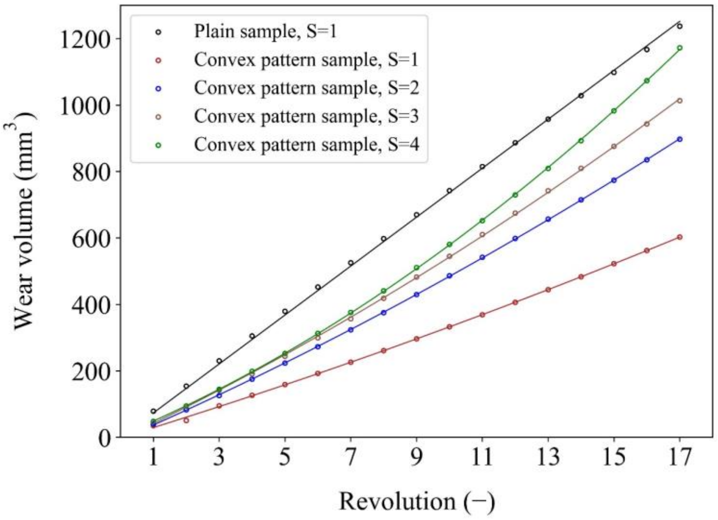

Figure 6.11 Wear volume in relation to revolution (S indicates particle scaling factor)

$$y_{P1} = 73.64x, R^2 = 0.9994 \tag{6.2}$$

$$y_{C1} = 0.31x^2 + 30.29x, R^2 = 0.9997 \tag{6.3}$$

$$y_{C2} = 0.59x^2 + 43.21x, R^2 = 0.99997 \tag{6.4}$$

$$y_{C3} = 0.78x^2 + 47.12x, R^2 = 0.99998 \tag{6.5}$$

$$y_{C4} = 1.57x^2 + 41.62x, R^2 = 0.99996 \tag{6.6}$$

where the subscripts P and C represent the plain and convex pattern sample, respectively. The number indicates the particle scaling factor.

As the experiment of 56 hours is represented by 2 numerical revolutions, the 184 hours are equal to 6.57 revolutions. Based on the Equation (6.2) and (6.3), the wear volumes of the plain and convex pattern samples are 474.5 and 240.3 mm^3, respectively, showing a 56 % wear reduction. Similarly, the experimental result shown in Figure 6.4 indicates 483.9 and 212.9 mm^3 volume losses for the plain and convex pattern sample, leading to a 51 % wear reduction. Quantitatively, the numerical model demonstrates 5 % difference with the experimental results.

To better understand the relation between wear volume and number of revolutions, the average wear volume increment of individual elements shown in Figure 6.12 is defined. It is denoted as the average wear volume increment of individual meshes between two revolutions. Equation (6.7) is used to calculate wear volume increment:

$$\Delta v(j) = \frac{\sum_{i=1}^{n} \left[h(j+1)_i - h(j)_i \right] \cdot A_i}{n} \tag{6.7}$$

where j, n, and subscript i denote the number of revolutions, the number of elements, and the ith element, respectively. The Δv(j), h(j)$_i$, and A$_i$ represent the wear volume increment of jth revolution, wear depth of element i for j revolutions, and the area of mesh element j, respectively.

For the plain sample, the wear volume increment decreases from 0.0022 mm^3 to 0.002 mm^3. For the convex patten sample, it has a increasing trend for different particle scaling factors. The wear volume increases more slowly with a lower particle scaling factor than with a higher scaling factor. For a particle scaling factor of 4, the wear volume increment surpasses that of the plain sample at revolution 15, which means the wear volume of the sample increases faster than that of the plain sample. Moreover, it implies that the total wear volume of the sample can exceed the total wear volume of the plain sample after one specific revolution.

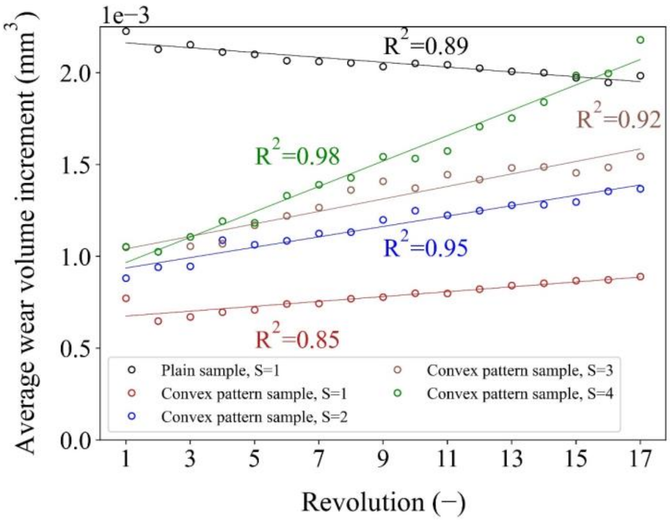

Figure 6.12 Average wear volume increment for each revolution

Figure 6.13 depicts the wear volume of each column for both the convex and plain samples. For the plain sample, the wear volume increases from column 1 to 5. For the convex pattern sample, the convex pattern accounts for 56 % of the total wear volume of the sample. Column 1 shows the highest wear volume, as it guides and initializes the movement of particles when they come into contact with the sample. Besides, columns 1 and 5 see greater wear volume levels than columns 2 and 4, because the surface area of columns 2 and 4 is lower than the other 3 columns.

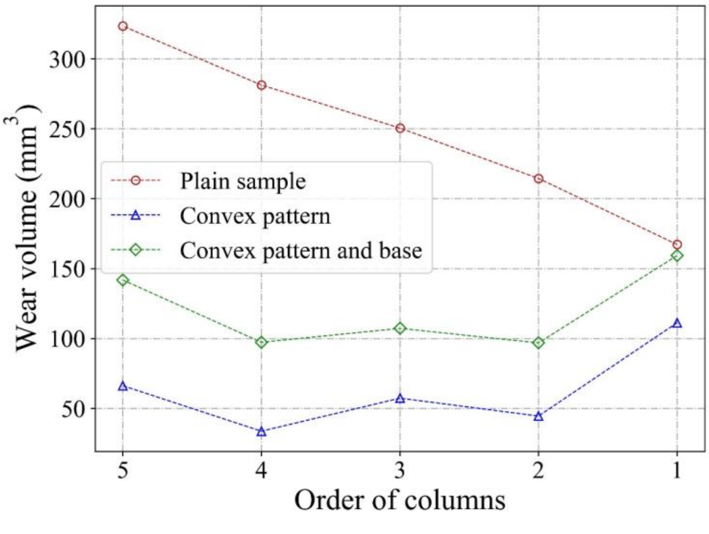

Figure 6.13 Wear volume distribution of each column

Figure 6.14 compares the wear volume of individual convex elements as labelled in Figure 6.1. Columns 1, 3, and 5 show a wide range of wear volumes from 7.6 to 31.6 mm^3, while columns 2 and 4 show a relatively narrow range from 6.9 to 14.1 mm^3. The convex elements located at the two sides of the sample demonstrate the maximum level of wear volume. This is because the convex elements located at the two outer ends of the sample have a weak effect on guiding and rolling particles. For a detailed explanation, see the previous study [158].

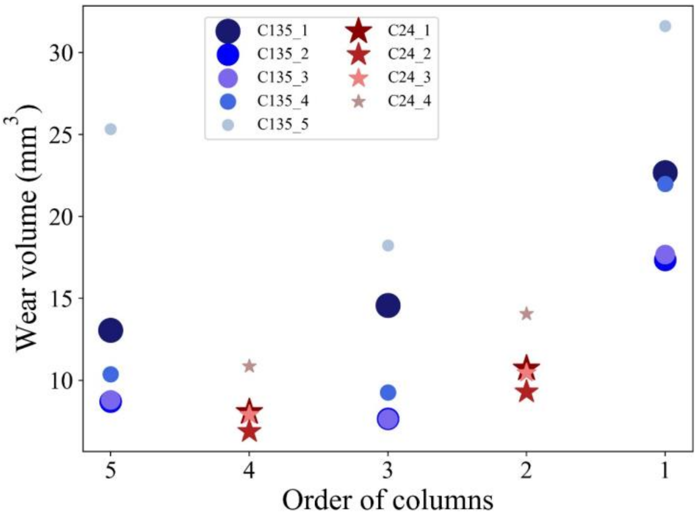

Figure 6.14 Wear volume distribution of individual convex elements

6.4.2.2 Wear distribution and reconstruction

Figure 6.15 displays the wear distribution in two samples after 17 revolutions. For the plain sample shown in Figure 6.15 (a), the wear is almost evenly distributed over the full sample. For the convex pattern sample shown in Figure 6.15 (b), wear paths are formed among the convex elements because of the flow behaviour of particles. In addition, the majority of wear is transferred to the convex pattern, thus protecting the base.

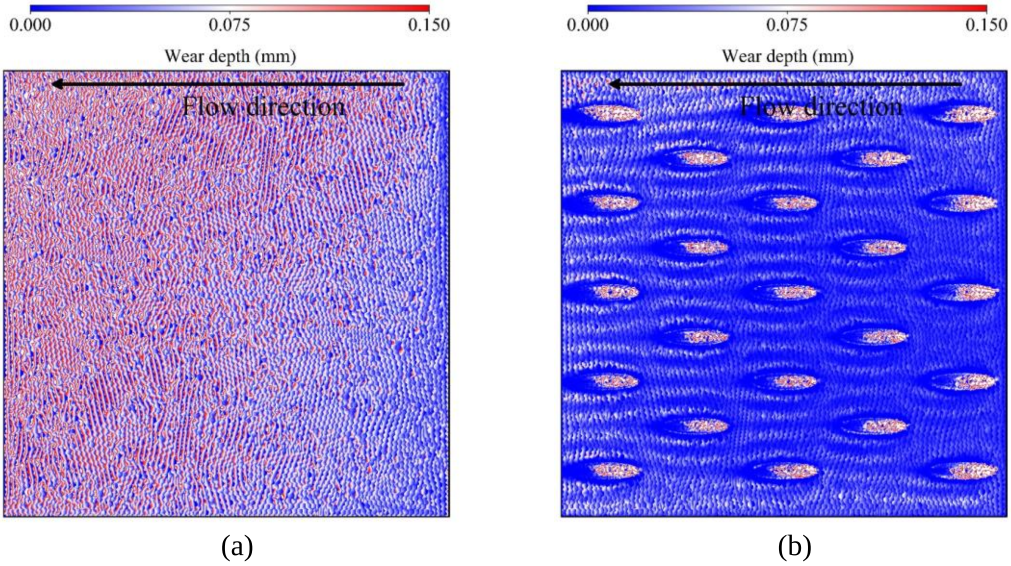

(a) (b)

Figure 6.15 Wear distribution (a) plain sample, (b) convex pattern sample

Figure 6.16 compares the deformation process of three convex elements in column 1, since this column suffers the most severe deformation, as shown in Figure 6.13. C11 and C15 are located at the two ends of the sample and C13 is in the middle of column 1, as illustrated in Figure 6.1. From the side view, these three convex elements follow a similar deformation trend. The front part of the convex elements suffers the most severe deformation, since this part comes into direct contact with particles. From the front view, it can be seen that the inner side of C11 and outer side of C15 show greater deformation. This implies that the convex pattern hardly affects the flow behaviour of particles at the two sides [158]. Furthermore, C15 is subject to the greatest degree of deformation because the particles at the outer end of a circular wear tester slide longer distances. Overall, the numerical model indicates a similar deformation trend with the experiment. As the effect of the coarse mesh on the reconstruction, the wear contour is rougher compared to that of the experiment.

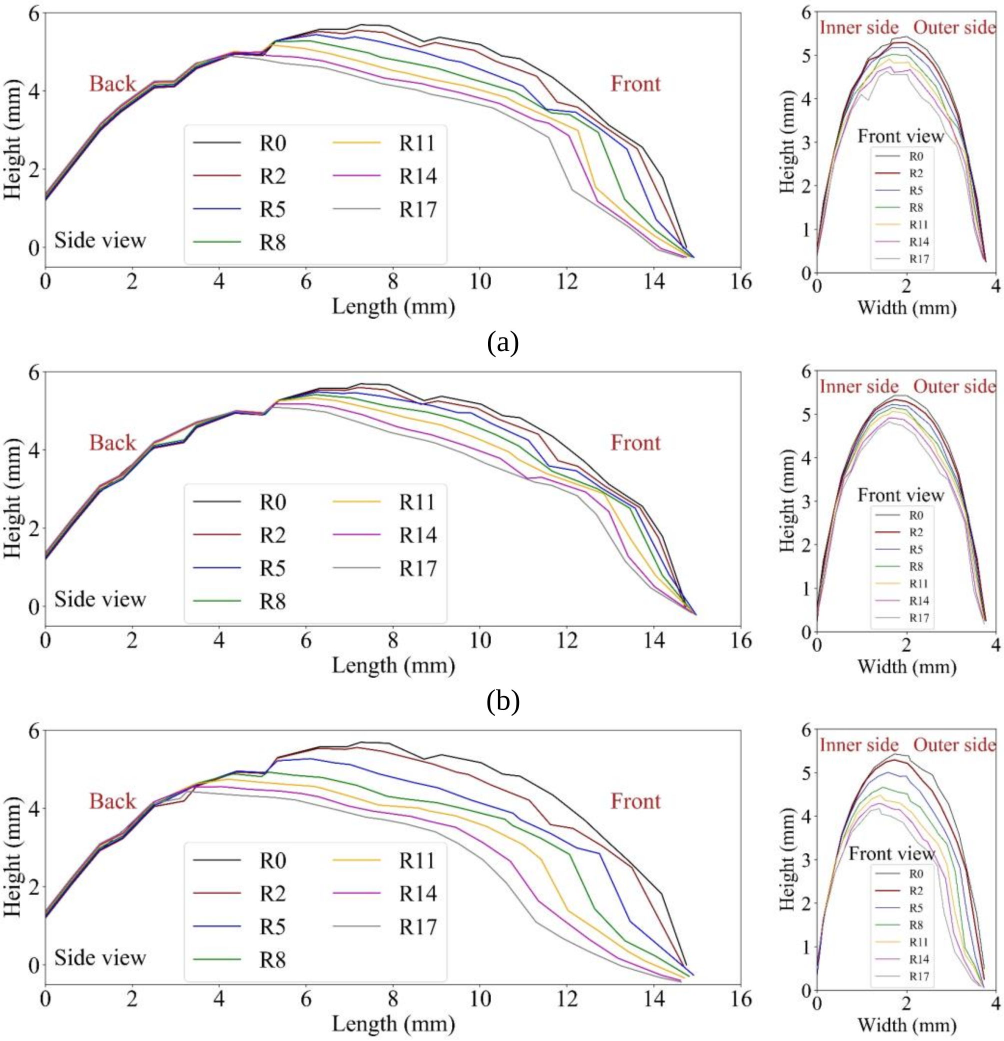

(a)

(b)

(c)

Figure 6.16 Sample deformation from simulations
(a) C11 (1st column 1st convex element), (b) C13 (1st column 3rd convex element), (c) C15 (1st column 5th convex element)

6.4.3 Contact behaviour

6.4.3.1 Particle flow behaviour

Particle flow behaviour consists of the angular and transitional velocity of particles at the bottom layer, where the particles are directly affected by the convex pattern. Figure 6.17 shows the angular velocity of particles. For the plain sample, the angular velocity stays within a relatively small range from 75 ± 16 deg/s to 95 ± 34 deg/s. The convex pattern sample displays a decreasing trend as revolutions increase, from 198 ± 56 deg/s to 100 ± 26 deg/s. The angular velocity indicates that the plain sample has a minor effect on particle rolling behaviour, while the convex pattern sample facilitates rolling and therefore reduces sliding. As the convex pattern continues to deform, particles roll less readily due to sample deformation. Although angular velocity decreases for the convex pattern sample, it is still higher than for the plain sample.

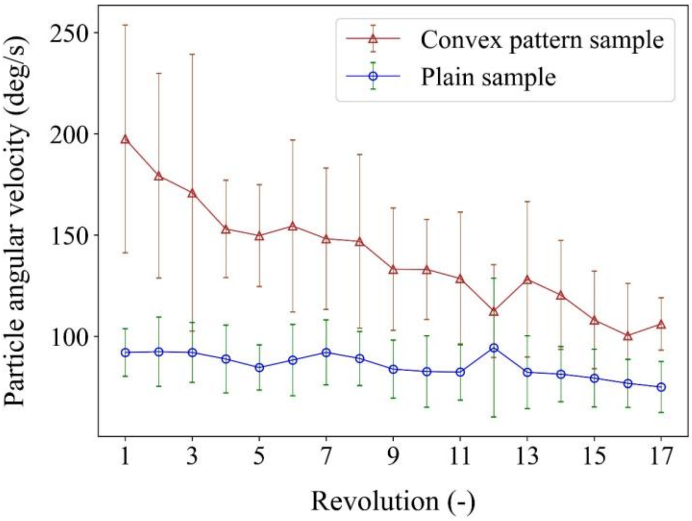

Figure 6.17 Angular velocity of particles (Error bar indicates standard deviation)

Figure 6.18 indicates the particle velocity at the bottom layer. Particle velocity shows an opposite trend to angular velocity. The particles in the plain sample exhibit velocities exceeding 500 mm/s, while the convex pattern sample sees much lower velocities of less than 250 mm/s. As particle velocity is related to sliding distance, this means that particles slide less far in the convex pattern sample than in the plain sample, resulting in less wear. The particle flow behaviour is consistent with the previous studies. For a detailed explanation, please refer to [198].

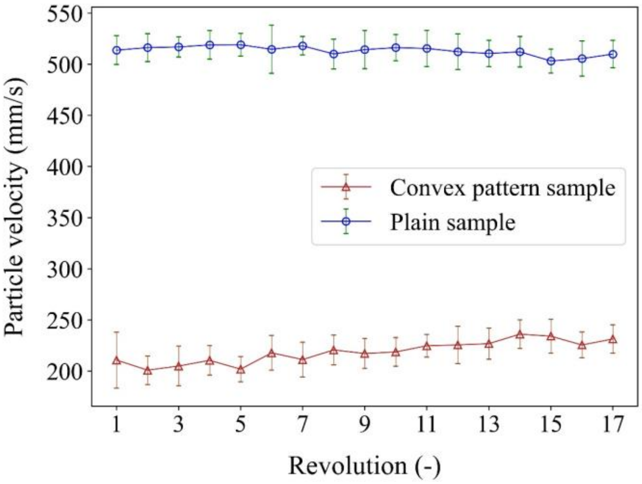

Figure 6.18 Particle velocity (Error bar indicates standard deviation)

To explicitly demonstrate particle flow behaviour, the relative particle angular and transitional velocity distributions at the 5th revolution are constructed as shown in Figure 6.19 and Figure 6.20. It should be noted that the relative velocity is based on the average value for the plain sample. For the angular velocity, Figure 6.19 shows that the particles have a greater tendency to roll on the convex pattern sample (Figure 6.19 (b)) than on the plain sample (Figure 6.19 (a)). This indicates that the convex pattern sample facilitates the rolling of particles.

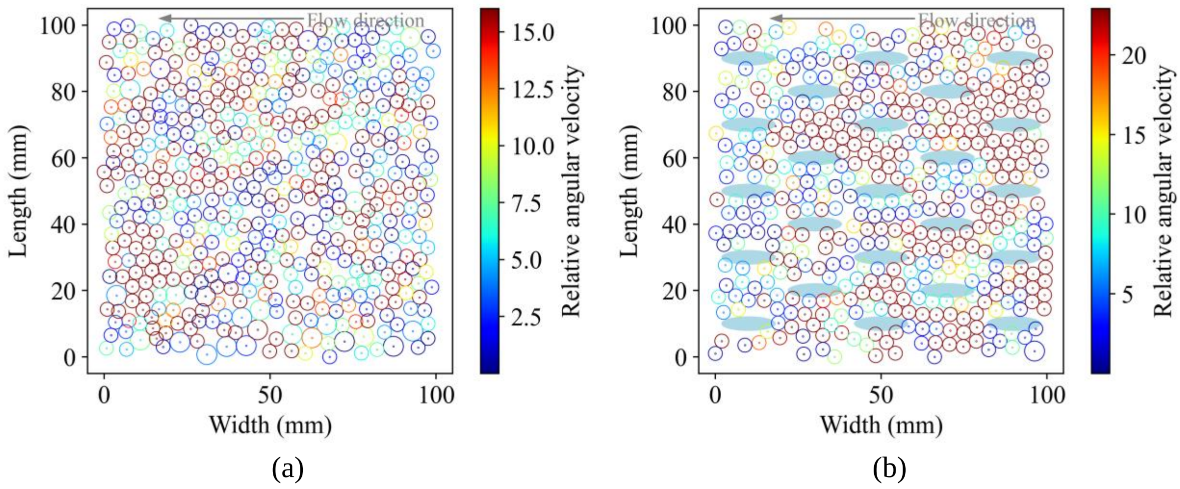

(a)

(b)

Figure 6.19 Relative angular velocity distribution of particles in the (a) plain sample, (b) convex pattern sample (The circles represent the positions and diameters of particles. The colors indicate the relative angular velocities of particles.)

Figure 6.20 illustrates relative particle transitional velocity. The arrows in the circles represent the directions of particle velocity. For the plain sample shown in Figure 6.20 (a), the particles flow in a consistent pattern over the whole sample. The particles at the outside have higher velocities because of the rotating effect of the circle wear tester. For the convex pattern sample shown in Figure 6.20 (b), the particles have a lower transitional velocity compared to that of the plain sample, leading to a shorter sliding distance. After contact with the convex pattern, the moving direction of the particles alters and weakens the direct contact with the convex pattern. In addition, the convex pattern has a guiding effect on particles and forces them to move among the convex elements.

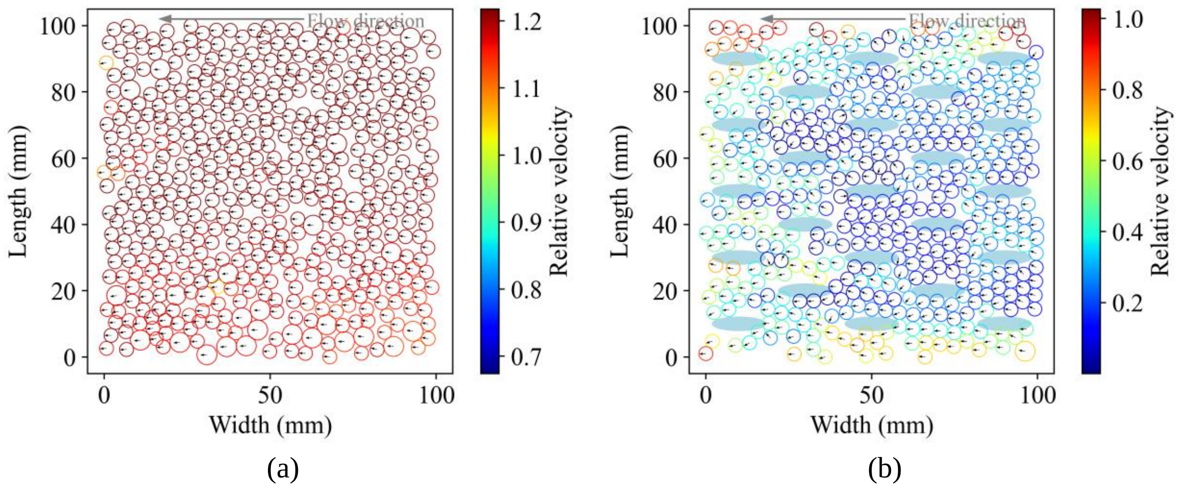

(a)

(b)

Figure 6.20 Relative transitional velocity distribution of particles in the (a) plain sample, (b) convex pattern sample (The circles represent the positions and diameters of particles. The colors indicate the relative velocities of particles. The arrows in the circles indicate the direction of the particle velocities.)

6.4.3.2 Normal force

Figure 6.21 compares the normal force in the convex pattern and plain samples. The normal force has a similar tendency to the angular velocity shown in Figure 6.19. For the plain sample, the normal force has a relatively narrow range from 15 ± 3 N to 18 ± 2 N with minor fluctuation, which means that the deformation of the plain sample has a minor effect on the contact between particles and the sample. For the convex pattern sample, the normal force displays a decreasing trend from 28 ± 7 N to 18 ± 4 N. This indicates that the deformation of the convex pattern weakens the normal contact with particles and that deformation alters the contact between the sample and the particles.

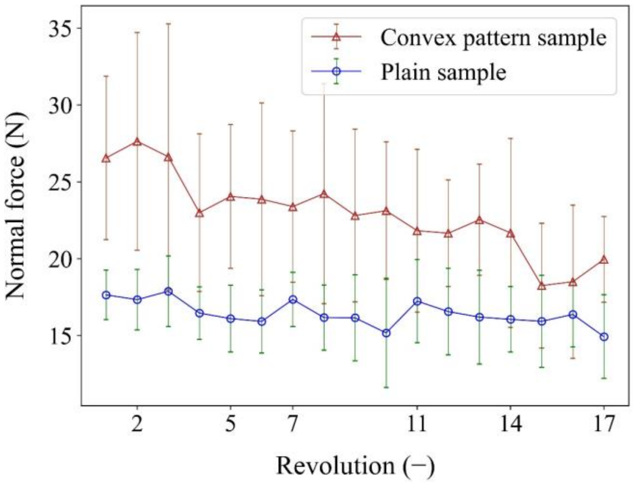

Figure 6.21 Normal force as a function of revolution (Error bar indicates standard deviation)

Figure 6.22 indicates the normal force distribution based on the division of the sample shown in Figure 6.1. The plain sample exhibits an increasing trend due to particle accumulation, as explained in the previous study [158]. For the convex pattern sample, the normal force is higher than that of the plain sample over the five columns. Since the first column of the convex pattern initializes the bulk flow behaviour, it takes up the majority of the total force (more than 65 %) of the column. Therefore, the first column of the convex pattern sample presents the highest wear volume and the most severe surface deformation.

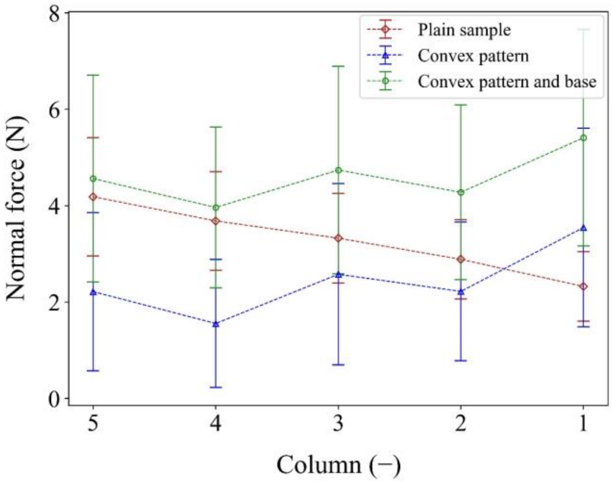

Figure 6.22 Normal force distribution (Error bar indicates standard deviation)

6.5 Conclusions

This chapter addresses the question:

To what extent does the deformed convex pattern sample continue to reduce sliding wear caused by bulk material?

This chapter investigates the deformation of a convex pattern sample caused by sliding wear with respect to different particle size distributions. The aim is to provide clarity on how effectively the deformed sample reduces sliding wear compared to a plain sample.

The wear experiments indicate that the convex pattern sample reduces wear by 43 % compared to a plain sample and that there is a linear relation between wear volume loss and test time for both the plain and convex pattern samples. The sample deformation shows that the sides of the convex pattern sample are subjected to more severe wear.

The numerical model is validated by comparing the wear volume of a plain sample, which showed wear reduction rates of 68.9 % and 43.0 % for the simulation and experiments, respectively. As the 56-hour experiment can be reliably represented by 2 revolutions, a scaling factor is calculated as 4.0×10^4 by comparing the effective distance travelled in the experiment and simulation.

The numerical model indicates a linear and quadratic relation between wear volume and the number of revolutions for the plain and convex pattern sample, correspondingly. This implies that the trend of wear reduction weakens as a result of the deformation. Particle size also has a significant effect on the effectiveness of wear reduction of the convex pattern sample, with smaller particles corresponding to less wear.

The deformation distribution of the convex pattern depends on the contact behaviour of the particle flow, and the deformation accelerates as the rolling of particles weakens. The convex elements at the sides of the sample experience more severe deformation, similar to what was observed in the experiment.

The contact behaviour of particles at the bottom layer shows that the convex pattern decelerates the transitional velocity of particles and facilitates rolling, leading to a shorter sliding distance than a plain sample.

Future work will focus on two aspects. First, the mesh distortion issue should be solved to fully wear out the convex pattern, so the entire deformation behaviour of the convex pattern can be evaluated. Second, the wear experiments should continue to generate sufficient wear to compare the wear behaviour of the sample with the numerical model. To accelerate the deformation of the convex pattern sample, a deeper particle bed will be used.

7 Conclusions and recommendations

7.1 Conclusions

This thesis aims to model and predict the deformation of a convex pattern surface proposed to reduce sliding wear for bulk material flows, and how its performance remains under influence of wear accumulation on the longer term. A numerical model based on a deformable geometry technique is validated and successfully simulates the deformation of the convex pattern surface due to abrasive wear. The numerical results indicate that the deformed convex pattern surface leads to lower sliding wear than a plain sample, although its effectiveness weakens as wear accumulates. The convex pattern surface reduces wear as it alters the flow behaviour of bulk material by facilitating the rolling of individual particles and changing bulk flow directions. The research questions formulated in Chapter 1 are addressed below.

1. ***What are the main wear mechanisms in bulk handling and what is a suitable numerical method for wear modelling in this context?***

Wear occurs as a result of interaction between particles and geometry during the bulk handling process. Two main wear mechanisms are abrasive wear and impact wear. Each of the wear mechanisms contains multiple wear modes, depending on the three system characteristics, namely particle properties, surface properties, and operational conditions.

The wear modes for the abrasive wear consist of micro-cutting, micro-ploughing, and wedge formation, while the impact wear deforms a surface by micro-cutting and lip formation associated with the impact angle of particles.

Multiple numerical methods including two coupled methods are evaluated on the suitability to model the surface deformation caused by bulk material. The selection of the numerical model refers to bulk material and surface deformation. By comparing the methods, the DEM with deformable geometry technique has the advantages to integrate free flowing bulk material and surface deformation effectively and accurately.

2. *What is the effect of the parameters of the convex configuration on wear reduction performance of the convex pattern surface?*

Two flow regimes, which highly depend on particle bed thickness, are formed, namely, the continuous and discontinuous flow regime. The mechanism of the sliding wear reduction for the two flow regimes differs. For the continuous flow regime, the convex pattern surface can significantly facilitate the rolling of particles to reduce the sliding between particles and the sample. The discontinuous flow regime can reduce the relative sliding velocity and therefore decline the sliding distance. The continuous flow regime is preferred, as this flow regime induces less particle accumulation and more apparent rolling effect of particles.

Three main factors (major radius, sample velocity, and particle bed thickness) and one interaction (minor radius and horizontal distance) have statistical significance based on the regression model. The particle bed thickness has the most significant influence on the sliding wear, and the flow regime is continuous when the particle bed thickness is 40 mm (15 times of d_{50}). The height and the minor radius of the convex have no significant influence on the sliding wear, which is consistent with the previous study [7].

The combination of configuration and operational conditions of run 5 and run 2 indicates the minimum wear rates for the continuous and discontinuous flow regimes, respectively. The properties of the two runs hint to a design that is optimal in both regimes simultaneously. It should be noted that this optimal design is based on the specific dry bulk material with d_{50} of 2.65 mm, and it is suitable for bulk material with similar bulk properties.

3. *To what extent can the convex pattern sample reduce wear for different particle size distributions?*

The particle size has no effect on the sliding wear of the plain surface as the bulk flow behaviour is hardly affected by the surface, while it has a linear relation with the sliding wear for the convex pattern surface. The majority of the sliding wear of the convex pattern surface occurs on the convex part, and the base of the sample is protected by transferring the sliding wear to the convex pattern.

The convex pattern surface enables to reduce the sliding wear compared with the plain surface when the scaling factor is lower than 4 under the modelling conditions. α_{ER} which is defined as the ratio of the particle radius to the equivalent radius of the convex determines the effect of the convex pattern surface. When α_{ER} is lower than 1, the convex pattern can reduce the sliding wear by altering the flow behaviour of particles. When α_{ER} is higher than 1, particles can traverse across the convex pattern, leading to the resistance of the particles.

The investigated convex pattern surfaces can, in some cases, significantly accelerate the rolling of particles compared to the plain surface. It should be noted that only the flow behaviour cannot fully reflect the effect of the convex pattern on the sliding wear.

4. *In what way can the surface deformation caused by sliding of a single particle be modelled?*

For the sliding of a particle with the radius of 3 mm, the mesh size of the disc is set as 0.1 mm. The wear contour indicates that the mesh size from 0.1 mm to 1 mm converges to total wear volume, but has a significant effect on the wear profile of the geometry. The coarser mesh generates wider and shallower contours, while a fine mesh can obtain comparable wear contour with test results. This is because the contact between particle and disc involves more elements for the surface with fine meshes, so the deformation of the disc evolves more elements and generates a more precise contour.

For the geometrical deformation technique, the wear path reaches a relatively steady state after eight revolutions. It is verified that the wear depths and wear widths of the wear contours follow normal distributions after a run-in phase because of the self-smoothing effect of the interconnected common nodes of the mesh elements.

The wear coefficient is calibrated by comparing the wear volume between simulation and test results, and the wear volume has a quadratic relation with the number of revolutions. The wear volume of the test accurately predicts the simulation results with the minimum number of revolutions when the wear coefficient is lower than $2\times10^{-11}\mathrm{Pa}^{-1}$. For different wear coefficients, the wear volumes correspond to different quadratic relations. The lower the wear coefficient, the weaker the tendency of the quadratic relation.

To obtain comparable wear results, the minimum number of revolutions is determined as eight, and the corresponding maximum scaling factor, which is defined as the ratio of the number of test revolutions to that of the modelling revolution, is 162.8. By scaling up the wear coefficient and properly selecting the mesh size, the long-term laboratory pin-on-disc test can be modelled by a short-term numerical model. This scaling effect can significantly save computational time with promising calculation precision.

5. ***To what extent does the deformed convex pattern sample continue to reduce sliding wear caused by bulk material?***

The wear experiments indicate that the convex pattern sample can reduce wear by 43 % compared to a plain sample and that there is a linear correlation between wear volume loss and test time for both the plain and convex pattern samples over a short period of time. The sample deformation shows that the sides of the convex pattern sample are subjected to more severe wear.

The numerical model is validated by comparing the wear volumes of a plain sample obtained in simulation and experiment. The result indicates wear reduction rates of 68.9 % and 43.0 % for the simulation and experiments, respectively. As the 56-hour circular wear experiment can be reliably simulated by 2 revolutions after the material flow reaches a stable state, a scaling factor is calculated as 4.0×10^{4} by comparing the effective distance travelled in the experiment and simulation.

The numerical model indicates that there is a linear relation between the number of revolutions and the wear volume of a plain sample and a quadratic relation for the convex pattern sample. This implies that the trend of wear reduction weakens as a result of the deformation. Particle size also has a significant effect on the effectiveness of wear reduction of the convex pattern sample. The wear caused by the contact with the particles corresponding to lower scaling factor is less than that corresponding to the higher scaling factor.

The convex pattern accounts for 56 % of the total wear volume of the convex pattern sample. The deformation distribution of the convex pattern depends on the flow behaviour of particles, and the deformation accelerates as the rolling of particles weakens. The convex elements at the sides of the sample experience more severe deformation, similar to what was observed in the experiment.

The contact behaviour of particles at the bottom layer shows that the convex pattern decelerates the transitional velocity of particles and facilitates rolling, leading to a shorter sliding distance and therefore less wear than a plain sample.

7.2 Recommendations

The ability of a convex pattern surface is to reduce wear compared to a plain sample during bulk handling. To boost the application of the convex pattern surfaces to industries dealing with a large amount of material and facing severe wear, a further study from three aspects, including numerical model, laboratory test, and applications, is recommended.

1. Numerical model

Different wear models should be compared and selected cautiously. Archard wear model is widely applied to the research of wear in the mining industry. However, it only takes the sliding of particles into account. The rolling of particles with sharp edges has a significant effect on the deformation of a surface. Therefore, depending on particle properties, future work should integrate the rolling of particle into a wear model.

The effect of particle shape on the sliding wear of the convex pattern surface should be considered. The mechanism of sliding wear reduction is attributed to the rolling and guiding effect on particles, so the simplified spherical particles take the advantage of being guided and rolled. To suit the application of the bulk handling process, particle shape is a critical factor to be investigated.

Rolling model Type A can be replaced by rolling model Type C. Model A has the drawback of dissipating all kinetic energy and the residual kinetic energy depends on the time step adopted in simulations. Rolling model C can provide stable torques and appears to work well in both static and dynamic scenarios, so the more accurate bulk flow behaviour will be simulated.

2. Laboratory test

A long-term laboratory test should be performed. As indicated in the numerical result, the effectiveness of the convex pattern surface weakens as the surface deformation affects the flow behaviour of particles. Therefore, to have an insight into the effect of the convex pattern sample on the sliding wear reduction, the laboratory test should continue to be conducted until the convex pattern is completely worn out.

The reconstruction of the convex pattern after 184-hours testing based on the 3D scanning is insufficient as the deformation is limited compared to the precision of the scanner, leading to a relatively high measuring error. The deformation of the convex pattern sample after a long time test should be reconstructed based on the 3D scanning to compare with the numerical result.

The laboratory test is limited to the specific free-flowing river gravel with d_{50} of 2.65 mm. As the numerical result indicates that the particle size has significant effect on the wear performance of the convex pattern surface, it is essential to investigate to what extent the particle size affects wear reduction and surface deformation at laboratory scale.

Particle hardness directly affects the wear mode and therefore the long-term wear performance of the convex pattern sample, so it is worth to evaluate the surface deformation of the sample under the conditions of different particle hardness.

To reflect more realistic practice and reduce the testing time, the operational conditions can be changed such as increasing the particle bed height to resemble higher normal loads, using new particles with high angularity to get more representative results, and increasing the testing speed to raise the sliding distance of material.

3. Industrial applications

A transfer chute equipped with a convex pattern should be manufactured and tested to confirm that the convex pattern sample reduces sliding wear compared to a plain sample on industrial applications. To consist with the laboratory test, it is recommended to commence testing free-flowing material with particle size smaller than the equivalent radius of the convex.

Another principal wear mechanism, namely impact wear, which is out of the scope of this thesis, plays a significant role in the wear of bulk handling equipment, so it is worth investigating whether the convex pattern surface might exhibit wear reduction properties.

Although the convex pattern enables to reduce wear, the flow resistance caused by the interface should be evaluated. Considering a handling surface equipped with the convex configuration leads to extra manufacturing cost, the applicability of the design should be deliberated when the raised cost is higher compared to that caused by the maintenance and downtime of a plain surface.

Bibliography

[1] D. Schulze, Powders and Bulk Solids, 2021. https://doi.org/10.1007/978-3-030-76720-4.

[2] Edem, Upgrading a coal transfer chute, Altair. (2022). https://www.altair.com/resource/upgrading-a-coal-transfer-chute-hatch-deploys-altair-edem-bulksim-solution-for-mining (accessed March 8, 2022).

[3] A.W. Roberts, M. Ooms, S.J. Wiche, Concepts of boundary friction, adhesion and wear in bulk solids handling operations, in: Third Int. Conf. Bulk Mater. Storage, Handl. Transp., 1989: p. 349.

[4] K.R.G. Tuckey, Intelligent selection of engineered wear linings in iron ore plant, Miner. Process. Extr. Metall. 112 (2003) 33–38. https://doi.org/10.1179/037195503225011420.

[5] G. Chen, Surface Wear Reduction of Bulk Solids Handling Equipment Using Bionic Design, 2017. https://doi.org/10.4233/uuid:b60cb231-222d-434d-b987-cf36605bc719.

[6] A.W. Roberts, Chute performance and design for rapid flow conditions, Chem. Eng. Technol. 26 (2003) 163–170. https://doi.org/10.1002/ceat.200390024.

[7] M. Andrejiova, A. Grincova, D. Marasova, Measurement and simulation of impact wear damage to industrial conveyor belts, Wear. 368–369 (2016) 400–407. https://doi.org/10.1016/j.wear.2016.10.010.

[8] D. Ilic, Development of design criteria for reducing wear in iron ore transfer chutes, Wear. 434–435 (2019) 202986. https://doi.org/10.1016/j.wear.2019.202986.

[9] A.W. Roberts, S.J. Wiche, Prediction of lining wear life of bins and chutes in bulk solids handling operations, Tribol. Int. 26 (1993) 345–351. https://doi.org/10.1016/0301-679X(93)90071-8.

[10] O. V. Penkov, Y.A. Bugayev, I. Zhuravel, V. V. Kondratenko, A. Amanov, D.E. Kim, Friction and wear characteristics of C/Si bi-layer coatings deposited on silicon substrate by DC magnetron sputtering, Tribol. Lett. 48 (2012) 123–131. https://doi.org/10.1007/s11249-012-0008-7.

[11] M. Khadem, O. V. Penkov, H.K. Yang, D.E. Kim, Tribology of multilayer coatings for wear reduction: A review, Friction. 5 (2017) 248–262. https://doi.org/10.1007/s40544-

017-0181-7.

[12] J.F.V. Vincent, O.A. Bogatyreva, N.R. Bogatyrev, A. Bowyer, A.K. Pahl, Biomimetics: Its practice and theory, J. R. Soc. Interface. 3 (2006) 471–482. https://doi.org/10.1098/rsif.2006.0127.

[13] H. Yu, Z. Han, J. Zhang, S. Zhang, Bionic design of tools in cutting: Reducing adhesion, abrasion or friction, Wear. 482–483 (2021) 203955. https://doi.org/10.1016/j.wear.2021.203955.

[14] X.F. Yang, R. Xia, H.W. Zhou, L. Guo, L.J. Zhang, Bionic surface design of cemented carbide drill bit, Sci. China Technol. Sci. 59 (2016) 175–182. https://doi.org/10.1007/s11431-015-5942-9.

[15] G. Chen, G. Lodewijks, D.L. Schott, Numerical prediction on abrasive wear reduction of bulk solids handling equipment using bionic design, Part. Sci. Technol. 37 (2019) 960–969. https://doi.org/10.1080/02726351.2018.1480547.

[16] G. Chen, D.L. Schott, G. Lodewijks, Bionic design methodology for wear reduction of bulk solids handling equipment, Part. Sci. Technol. 35 (2017) 525–532. https://doi.org/10.1080/02726351.2016.1144666.

[17] I. Hutchings, P. Shipway, Wear by hard particles, 2nd ed., Elsevier Ltd., 2017. https://doi.org/10.1016/b978-0-08-100910-9.00006-4.

[18] I.M. Hutchings, Mechanisms of wear in powder technology: A review, Powder Technol. 76 (1993) 3–13. https://doi.org/10.1016/0032-5910(93)80035-9.

[19] A. Misra, I. Finnie, A review of the abrasive wear of metals, J. Eng. Mater. Technol. Trans. ASME. 104 (1982) 94–101. https://doi.org/10.1115/1.3225058.

[20] J. Luo, W. Zhang, Microstructure and mechanical properties of Mg-1Er-0.6Zr, Spec. Cast. Nonferrous Alloy. 32 (2012) 789–792.

[21] I. Hutchings, P. Shipway, Friction and Wear of Engineering Materials, 2017. https://doi.org/10.1016/B978-0-08-100910-9.00003-9.

[22] I.M. Hutchings, Wear by particulates, Chem. Eng. Sci. 42 (1987) 869–878. https://doi.org/10.1016/0009-2509(87)80045-3.

[23] J.G.A. Bitter, A study of erosion phenomena. Part II, Wear. 6 (1963) 169–190. https://doi.org/10.1016/0043-1648(63)90073-5.

[24] J.G.A. Bitter, A Study of Erosion Phenomena Part I, Wear. 6 (1963) 169–190.

[25] G.P. Tilly, W. Sage, The interaction of particle and material behaviour in erosion processes, Wear. 16 (1970) 447–465. https://doi.org/10.1016/0043-1648(70)90171-7.

[26] D.J. O’Flynn, M.S. Bingley, M.S.A. Bradley, A.J. Burnett, A model to predict the solid particle erosion rate of metals and its assessment using heat-treated steels, Wear. 248 (2001) 162–177. https://doi.org/10.1016/S0043-1648(00)00554-8.

[27] D. Tabor, The hardness of metals, Oxford Clarendon Press ; New York Oxford Univ. Press. 2000. (n.d.).

[28] M.A. Moore, Abrasive wear, Int. J. Mater. Eng. Appl. 1(2) (1978) 97–111. https://doi.org/10.1016/s0261-3069(78)80015-6.

[29] K.L. Johnson, The correlation of indentation experiments, J. Mech. Phys. Solids. 18 (1970) 115–126. https://doi.org/10.1016/0022-5096(70)90029-3.

[30] P.A. Swanson, A.F. Vetter, The Measurement of Abrasive Particle Shape and Its Effect on Wear, ASLE Trans. 28 (1985) 225–230. https://doi.org/10.1080/05698198508981615.

[31] S. V. Prasad, T.H. Kosel, A study of carbide removal mechanisms during quartz abrasion. II: Effect of abrasive particle shape, Wear. 95 (1984) 87–102. https://doi.org/10.1016/0043-1648(84)90193-5.

[32] M. Liebhard, A. Levy, The effect of erodent particle characteristics on the erosion of metals, Wear. 151 (1991) 381–390. https://doi.org/10.1016/0043-1648(91)90263-T.

[33] S. Bahadur, R. Badruddin, Erodent particle characterization and the effect of particle size and shape on erosion, Wear. 138 (1990) 189–208. https://doi.org/10.1016/0043-1648(90)90176-B.

[34] I. Deiros Quintanilla, G. Combe, F. Emeriault, C. Voivret, J.F. Ferellec, X-ray CT analysis of the evolution of ballast grain morphology along a Micro-Deval test: key role of the asperity scale, Granul. Matter. 21 (2019). https://doi.org/10.1007/s10035-019-0881-y.

[35] M.J. Rhodes, Introduction to particle technology, (2008). http://site.ebrary.com/id/10232631.

[36] A. Misra, I. Finnie, On the size effect in abrasive and erosive wear, Wear. 65 (1981) 359–373. https://doi.org/10.1016/0043-1648(81)90062-4.

[37] I.R. Kramer, L.J. Demer., The effect of surface removal on the plastic behaviour of aluminum single crystals, Trans. Metall. Soc. AIME. (1961) 780–786.

[38] J.T. Fourie, Plastic deformation of thin copper single crystals. I. The separate roles of edge and screw dislocations in stage I of work hardening, Philos. Mag. 15 (1967) 187–198. https://doi.org/10.1080/14786436708230357.

[39] M.A. Moore, R.M. Douthwaite, Plastic deformation below worn surfaces, Metall. Trans. A. 7 (1976) 1833–1839. https://doi.org/10.1007/BF02654978.

[40] A. Kelly, N.H. Macmillan, Strong solids 1966, Oxford, Clarendon Press. (1971).

[41] V. Gioncu, F. Mazzolani, Ductility of Seismic-Resistant Steel Structures, 2003. https://doi.org/10.1201/9781482271904.

[42] J.R. Rice, R. Thomson, Ductile versus brittle behaviour of crystals, Philos. Mag. 29 (1974) 73–97. https://doi.org/10.1080/14786437408213555.

[43] Z. Gahr, Karl-Heinz, Microstructure and wear of materials, (1987).

[44] K.H.Z. Gahr, Wear by hard particles, Tribol. Int. 31 (1998) 587–596. https://doi.org/10.1016/S0301-679X(98)00079-6.

[45] D. Aquaro, E. Fontani, Erosion of ductile and brittle materials, Meccanica. 36 (2001) 651–661. https://doi.org/10.1023/A:1016396719711.

[46] B.R. Lawn, M. V. Swain, Microfracture beneath point indentations in brittle solids, J. Mater. Sci. 1975 101. 10 (1975) 113–122. https://doi.org/10.1007/BF00541038.

[47] B. Lawn, R. Wilshaw, Indentation fracture: principles and applications, J. Mater. Sci. 10 (1975) 1049–1081. https://doi.org/10.1007/BF00823224.

[48] J.J. Coronado, S.A. Rodríguez, A. Sinatora, Effect of particle hardness on mild-severe wear transition of hard second phase materials, Wear. 301 (2013) 82–88. https://doi.org/10.1016/j.wear.2012.12.016.

[49] L. Fang, Q.D. Zhou, Y.J. Li, An explanation of the relation between wear and material hardness in three-body abrasion, Wear. 151 (1991) 313–321. https://doi.org/10.1016/0043-1648(91)90258-V.

[50] L. Fang, W. Liu, D. Du, X. Zhang, Q. Xue, Predicting three-body abrasive wear using Monte Carlo methods, Wear. 256 (2004) 685–694. https://doi.org/10.1016/S0043-1648(03)00464-2.

[51] E. Rabinowicz, L.A. Dunn, P.G. Russell, A study of abrasive wear under three-body conditions, Wear. 4 (1961) 345–355. https://doi.org/10.1016/0043-1648(61)90002-3.

[52] A. Misra, I. Finnie, Correlations between two-body and three-body abrasion and erosion of metals, Wear. 68 (1981) 33–39. https://doi.org/10.1016/0043-1648(81)90017-X.

[53] W. Yiling, W. Zishan, An analysis of the influence of plastic indentation on three-body abrasive wear of metals, Wear. 122 (1988) 123–133. https://doi.org/10.1016/0043-1648(88)90073-7.

[54] P.H. Adler, G.B. Olson, W.S. Owen, Strain Hardening of Hadfield Manganese Steel, Metall. Mater. Trans. A. 17 (1986) 1725–1737. https://doi.org/10.1007/BF02817271.

[55] M. Lindroos, M. Apostol, V. Heino, K. Valtonen, A. Laukkanen, K. Holmberg, V.T. Kuokkala, The deformation, strain hardening, and wear behaviour of chromium-alloyed hadfield steel in abrasive and impact conditions, Tribol. Lett. 57 (2015) 1–11. https://doi.org/10.1007/s11249-015-0477-6.

[56] G.L. Sheldon, Effects of surface hardness and other material properties on erosive wear of metals by solid particles, J. Eng. Mater. Technol. Trans. ASME. 99 (1977) 133–137. https://doi.org/10.1115/1.3443422.

[57] M.S. Bingley, S. Schnee, A study of the mechanisms of abrasive wear for ductile metals under wet and dry three-body conditions, Wear. 258 (2005) 50–61. https://doi.org/10.1016/j.wear.2004.01.022.

[58] I. Finnie, D.H. McFadden, On the velocity dependence of the erosion of ductile metals by solid particles at low angles of incidence, Wear. 48 (1978) 181–190. https://doi.org/10.1016/0043-1648(78)90147-3.

[59] I.M. Hutchings, A model for the erosion of metals by spherical particles at normal incidence, Wear. 70 (1981) 269–281. https://doi.org/10.1016/0043-1648(81)90347-1.

[60] R.E. Winter, I.M. Hutchings, Solid particle erosion studies using single angular particles, Wear. 29 (1974) 181–194. https://doi.org/10.1016/0043-1648(74)90069-6.

[61] T. Deng, M.S. Bingley, M.S.A. Bradley, The influence of particle rotation on the solid particle erosion rate of metals, Wear. 256 (2004) 1037–1049. https://doi.org/10.1016/S0043-1648(03)00536-2.

[62] I.M. Hutchings, Deformation of metal surfaces by the oblique impact of square plates, Int. J. Mech. Sci. 19 (1977) 45–52. https://doi.org/10.1016/0020-7403(77)90015-7.

[63] I.M. Hutchings, Mechanisms of the erosion of metals by solid particles., (1979). https://doi.org/10.1520/stp35795s.

[64] I. Finne, Erosion of surfaces, Wear. 3 (1960) 87–103. https://doi.org/10.1016/0043-1648(60)90055-7.

[65] L.K. Nordell, Particle flow modeling: transfer chutes & other applications, Int. Mater. Handl. Conf. (BELTCON 9), Johannesburg, South Africa. (1997) 1–16.

[66] D.B. Hastie, A.P. Grima, P.W. Wypych, Validation of particle flow through a conveyor transfer hood via particle velocity analysis, (2008). https://ro.uow.edu.au/engpapers/1315 (accessed April 6, 2022).

[67] A.P. Grima, P.W. Wypych, Discrete element simulation of a conveyor impact-plate transfer : calibration , validation and scale-up, Aust. Bulk Handl. Rev. (2010) 64–72. http://www.bulkhandling.com.au/pdfs/discrete-elementsimulation.pdf.

[68] Edem, Upgrading a coal transfer chute, Altair. (2022). https://www.altair.com/resource/upgrading-a-coal-transfer-chute-hatch-deploys-altair-edem-bulksim-solution-for-mining.

[69] H. Zhou, Y. Chen, M.A. Sadek, Modelling of soil-seed contact using the Discrete Element Method (DEM), Biosyst. Eng. 121 (2014) 56–66. https://doi.org/10.1016/j.biosystemseng.2014.02.006.

[70] T.J. Donohue, C. Wheeler, A. Katterfeld, T.J. Donohue, A.W. Roberts, D. Ilic, A. Katterfeld, Effective Transfer Chute Design including Dust Control for Handling Grains and other Products, Silos Granul. Mater. (SIGMA). Int. Conf. Agric. Eng. 2012 Agric. Eng. a Heal. Life. (n.d.).

[71] C.J. Coetzee, Review: Calibration of the discrete element method, Powder Technol. 310 (2017) 104–142. https://doi.org/10.1016/J.POWTEC.2017.01.015.

[72] G. Strang, G.J. Fix, D.S. Griffin, An Analysis of the Finite-Element Method, J. Appl. Mech. 41 (1974) 62–62. https://doi.org/10.1115/1.3423272.

[73] P. Põdra, S. Andersson, Simulating sliding wear with finite element method, Tribol. Int. 32 (1999) 71–81. https://doi.org/10.1016/S0301-679X(99)00012-2.

[74] V. Hegadekatte, N. Huber, O. Kraft, Finite element based simulation of dry sliding wear, Model. Simul. Mater. Sci. Eng. 13 (2005) 57–75. https://doi.org/10.1088/0965-0393/13/1/005.

[75] X. Shen, Y. Liu, L. Cao, X. Chen, Numerical simulation of sliding wear for self-lubricating spherical plain bearings, J. Mater. Res. Technol. 1 (2012) 8–12. https://doi.org/10.1016/S2238-7854(12)70003-0.

[76] K. Shimizu, T. Noguchi, H. Seitoh, M. Okada, Y. Matsubara, FEM analysis of erosive wear, Wear. 250–251 (2001) 779–784. https://doi.org/10.1016/S0043-1648(01)00716-5.

[77] L.E. Crocker, A Review of Current Methods for Modelling Erosive Wear, 2011.

[78] L. Tang, S. Ding, Y. Xie, Y. Huo, A multilayer nodes update method in FEM simulation of large depth fretting wear, Wear. 301 (2013) 483–490. https://doi.org/10.1016/j.wear.2012.12.038.

[79] S. Fouvry, C. Paulin, T. Liskiewicz, Application of an energy wear approach to quantify fretting contact durability: Introduction of a wear energy capacity concept, Tribol. Int. 40 (2007) 1428–1440. https://doi.org/10.1016/j.triboint.2007.02.011.

[80] S. Garcin, S. Fouvry, S. Heredia, A FEM fretting map modeling: Effect of surface wear on crack nucleation, Wear. 330–331 (2015) 145–159. https://doi.org/10.1016/j.wear.2015.01.013.

[81] R. Branco, F. V. Antunes, J.D. Costa, A review on 3D-FE adaptive remeshing techniques for crack growth modelling, Eng. Fract. Mech. 141 (2015) 170–195. https://doi.org/10.1016/j.engfracmech.2015.05.023.

[82] J.H. Song, H. Wang, T. Belytschko, A comparative study on finite element methods for dynamic fracture, Comput. Mech. 42 (2008) 239–250. https://doi.org/10.1007/s00466-007-0210-x.

[83] M. Arjmandi, M. Ramezani, Finite element modelling of sliding wear in three-dimensional textile hydrogel composites, Tribol. Int. 133 (2019) 88–100. https://doi.org/10.1016/j.triboint.2019.01.011.

[84] P. Arnaud, S. Fouvry, S. Garcin, A numerical simulation of fretting wear profile taking account of the evolution of third body layer, Wear. 376–377 (2017) 1475–1488. https://doi.org/10.1016/j.wear.2017.01.063.

[85] I. Llavori, J.A. Esnaola, A. Zabala, M. Larrañaga, X. Gomez, Fretting: Review on the Numerical Simulation and Modeling of Wear, Fatigue and Fracture, Contact Fract. Mech. (2018). http://dx.doi.org/10.1016/j.colsurfa.2011.12.014.

[86] M. Takaffoli, M. Papini, Finite element analysis of single impacts of angular particles on ductile targets, Wear. 267 (2009) 144–151. https://doi.org/10.1016/j.wear.2008.10.004.

[87] R. Porcaro, A.G. Hanssen, M. Langseth, A. Aalberg, Self-piercing riveting process: An experimental and numerical investigation, J. Mater. Process. Technol. 171 (2006) 10–20. https://doi.org/10.1016/j.jmatprotec.2005.05.048.

[88] H.C. Lee, J.S. Choi, K.H. Jung, Y.T. Im, Application of element deletion method for numerical analyses of cracking, Manuf. Eng. 35 (2009) 154–161.

[89] J. Campbell, R. Vignjevic, Development of lagrangian hydrocode modelling for debris impact damage prediction, Int. J. Impact Eng. 20 (1997) 143–152. https://doi.org/10.1016/s0734-743x(97)87488-x.

[90] S.P. Timoshenko, X. On the transverse vibrations of bars of uniform cross-section , London, Edinburgh, Dublin Philos. Mag. J. Sci. 43 (1922) 125–131. https://doi.org/10.1080/14786442208633855.

[91] H.T. Phan, A.K. Tieu, H. Zhu, B. Kosasih, Q. Zhu, A. Grima, T.D. Ta, A study of abrasive wear on high speed steel surface in hot rolling by Discrete Element Method,

Tribol. Int. 110 (2017) 66–76. https://doi.org/10.1016/j.triboint.2017.01.034.

[92] J. Quist, M. Evertsson, J. Franke, The Effect of Liner Wear on Gyratory Crushing – A DEM Case Study, 3rd Int. Comput. Model. Symp. by MEI. (2011) 1–14. https://research.chalmers.se/en/publication/214351.

[93] D. André, I. Iordanoff, J.L. Charles, J. Néauport, Discrete element method to simulate continuous material by using the cohesive beam model, Comput. Methods Appl. Mech. Eng. 213–216 (2012) 113–125. https://doi.org/10.1016/j.cma.2011.12.002.

[94] I. Iordanoff, A. Battentier, J. Néauport, J.L. Charles, A discrete element model to investigate sub-surface damage due to surface polishing, Tribol. Int. 41 (2008) 957–964. https://doi.org/10.1016/j.triboint.2008.02.018.

[95] D.O. Potyondy, P.A. Cundall, A bonded-particle model for rock, Int. J. Rock Mech. Min. Sci. 41 (2004) 1329–1364. https://doi.org/10.1016/j.ijrmms.2004.09.011.

[96] D. Iliescu, D. Gehin, I. Iordanoff, F. Girot, M.E. Gutiérrez, A discrete element method for the simulation of CFRP cutting, Compos. Sci. Technol. 70 (2010) 73–80. https://doi.org/10.1016/j.compscitech.2009.09.007.

[97] Y. Tan, D. Yang, Y. Sheng, Discrete element method (DEM) modeling of fracture and damage in the machining process of polycrystalline SiC, J. Eur. Ceram. Soc. 29 (2009) 1029–1037. https://doi.org/10.1016/j.jeurceramsoc.2008.07.060.

[98] W. Li, Y. Huang, B. Fu, Y. Cui, S. Dong, Fretting damage modeling of liner-bearing interaction by combined finite element - Discrete element method, Tribol. Int. 61 (2013) 19–31. https://doi.org/10.1016/j.triboint.2012.11.019.

[99] G. Van Wyk, D.N.J. Els, G. Akdogan, S.M. Bradshaw, N. Sacks, Discrete element simulation of tribological interactions in rock cutting, Int. J. Rock Mech. Min. Sci. 65 (2014) 8–19. https://doi.org/10.1016/j.ijrmms.2013.10.003.

[100] J. Rojek, Discrete element thermomechanical modelling of rock cutting with valuation of tool wear, Comput. Part. Mech. 1 (2014) 71–84. https://doi.org/10.1007/s40571-014-0008-5.

[101] M. Stavropoulou, Modeling of small-diameter rotary drilling tests on marbles, Int. J. Rock Mech. Min. Sci. 43 (2006) 1034–1051. https://doi.org/10.1016/j.ijrmms.2006.03.008.

[102] O. Su, N. Ali Akcin, Numerical simulation of rock cutting using the discrete element method, Int. J. Rock Mech. Min. Sci. 48 (2011) 434–442. https://doi.org/10.1016/j.ijrmms.2010.08.012.

[103] R.L.J. Helmons, S.A. Miedema, M. Alvarez Grima, C. van Rhee, Modeling fluid pressure effects when cutting saturated rock, Eng. Geol. 211 (2016) 50–60. https://doi.org/10.1016/j.enggeo.2016.06.019.

[104] J. Sun, Excavation of Hard Deposits and Rocks On the Cutting of Saturated Rock, 2019. https://doi.org/10.4233/uuid.

[105] M. Takaffoli, M. Papini, Material deformation and removal due to single particle impacts on ductile materials using smoothed particle hydrodynamics, Wear. 274–275 (2012) 50–59. https://doi.org/10.1016/j.wear.2011.08.012.

[106] Y. Wang, H.H. Bui, G.D. Nguyen, P.G. Ranjith, A new SPH-based continuum framework with an embedded fracture process zone for modelling rock fracture, Int. J. Solids Struct. 159 (2019) 40–57. https://doi.org/10.1016/j.ijsolstr.2018.09.019.

[107] M.B. Liu, G.R. Liu, Smoothed particle hydrodynamics (SPH): An overview and recent developments, 2010. https://doi.org/10.1007/s11831-010-9040-7.

[108] M.M. Atif, S.W. Chi, E. Grossi, A.A. Shabana, Evaluation of breaking wave effects in liquid sloshing problems: ANCF/SPH comparative study, Nonlinear Dyn. 97 (2019) 45–62. https://doi.org/10.1007/s11071-019-04927-5.

[109] M. Hušek, J. Kala, F. Hokeš, P. Král, How to Handle Irregular Distribution of SPH

Particles in Dynamic Fracture Analysis, 1 (2016) 212–217.

[110] J. Remacle, J. Lambrechts, B. Seny, Blossom-Quad: A non-uniform quadrilateral mesh generator using a minimum-cost perfect-matching algorithm, International. (2012) 1102–1119. https://doi.org/10.1002/nme.

[111] W. Hu, Q. Tian, H. Hu, Dynamic fracture simulation of flexible multibody systems via coupled finite elements of ANCF and particles of SPH, Nonlinear Dyn. 84 (2016) 2447–2465. https://doi.org/10.1007/s11071-016-2657-9.

[112] S. Chakraborty, A. Shaw, A pseudo-spring based fracture model for SPH simulation of impact dynamics, Int. J. Impact Eng. 58 (2013) 84–95. https://doi.org/10.1016/j.ijimpeng.2013.03.006.

[113] M. Calamaz, J. Limido, M. Nouari, C. Espinosa, D. Coupard, M. Salaün, F. Girot, R. Chieragatti, Toward a better understanding of tool wear effect through a comparison between experiments and SPH numerical modelling of machining hard materials, Int. J. Refract. Met. Hard Mater. 27 (2009) 595–604. https://doi.org/10.1016/j.ijrmhm.2008.09.005.

[114] Y.F. Wang, Z.G. Yang, A coupled finite element and meshfree analysis of erosive wear, Tribol. Int. 42 (2009) 373–377. https://doi.org/10.1016/j.triboint.2008.07.009.

[115] W. Jianming, G. Na, G. Wenjun, Abrasive waterjet machining simulation by SPH method, Int. J. Adv. Manuf. Technol. 50 (2010) 227–234. https://doi.org/10.1007/s00170-010-2521-x.

[116] P. Baranowski, K. Damaziak, J. Malachowski, V.P. Sergienko, S.N. Bukharov, Modeling of abrasive wear by the meshless smoothed particle hydrodynamics method, J. Frict. Wear. 37 (2016) 94–99. https://doi.org/10.3103/S1068366616010037.

[117] F. Perazzo, R. Löhner, F. Labbe, F. Knop, P. Mascaró, Numerical modeling of the pattern and wear rate on a structural steel plate using DEM, Miner. Eng. 137 (2019) 290–302. https://doi.org/10.1016/j.mineng.2019.04.012.

[118] F. Schramm, Kalácska, V. Pfeiffer, J. Sukumaran, P. De Baets, L. Frerichs, Modelling of abrasive material loss at soil tillage via scratch test with the discrete element method, J. Terramechanics. 91 (2020) 275–283. https://doi.org/10.1016/j.jterra.2020.08.002.

[119] P.M. Esteves, D.B. Mazzinghy, R. Galéry, L.C.R. Machado, Industrial vertical stirred mills screw liner wear profile compared to discrete element method simulations, Minerals. 11 (2021) 1–20. https://doi.org/10.3390/min11040397.

[120] J. Rojek, E. Onate, Multiscale analysis using a coupled discrete/finite element model, Interact. Multiscale Mech. 1 (2008) 1–31. https://doi.org/10.12989/imm.2008.1.1.001.

[121] C. Labra, J. Rojek, E. Oñate, Discrete/Finite Element Modelling of Rock Cutting with a TBM Disc Cutter, Rock Mech. Rock Eng. 50 (2017) 621–638. https://doi.org/10.1007/s00603-016-1133-7.

[122] C. Labra, J. Rojek, E. Oñate, F. Zarate, Advances in discrete element modelling of underground excavations, Acta Geotech. 3 (2008) 317–322. https://doi.org/10.1007/s11440-008-0071-2.

[123] S.P. Xiao, T. Belytschko, A bridging domain method for coupling continua with molecular dynamics, Comput. Methods Appl. Mech. Eng. 193 (2004) 1645–1669. https://doi.org/10.1016/j.cma.2003.12.053.

[124] P. Hilgraf, Wear in bulk materials handling, Bulk Solids Handl. (2007) 464.

[125] L. Ren, Progress in the bionic study on anti-adhesion and resistance reduction of terrain machines, Sci. China, Ser. E Technol. Sci. 52 (2009) 273–284. https://doi.org/10.1007/s11431-009-0042-3.

[126] J. Tong, T. biao Lü, Y. hai Ma, H. kun Wang, L. quan Ren, R.D. Arnell, Two-Body Abrasive Wear of the Surfaces of Pangolin Scales, J. Bionic Eng. 4 (2007) 77–84. https://doi.org/10.1016/S1672-6529(07)60017-1.

[127] L. Ren, J. Tong, S. Zhang, B. Cheng, Reducing sliding resistance of soil against bulldozing plates by unsmoothed bionics surfaces, J. Terramechanics. 32 (1995) 303–309. https://doi.org/10.1016/0022-4898(96)00001-8.

[128] A. Filippov, S.N. Gorb, Frictional-anisotropy-based systems in biology: Structural diversity and numerical model, Sci. Rep. 3 (2013) 1–6. https://doi.org/10.1038/srep01240.

[129] G. Ke, S. Youhong, G. Runfeng, X. Liang, W. Chuanliu, L. Yumin, Application and prospect of bionic non-smooth theory in drilling engineering, Pet. Explor. Dev. 36 (2009) 519-522,541. https://doi.org/10.1016/S1876-3804(09)60143-9.

[130] R. Arvind Singh, E.-S. Yoon, Biomimetics in Tribology - Recent Developments, J. Korean Phys. Soc. 52 (2008) 656–668.

[131] C. Greiner, M. Schäfer, Bio-inspired scale-like surface textures and their tribological properties, Bioinspiration and Biomimetics. 10 (2015). https://doi.org/10.1088/1748-3190/10/4/044001.

[132] Y. Yan, W. Vreeburg, G. Chen, D. Schott, Minimization of wear in a transfer chute by geometric optimization of convex pattern surface: A DEM study, Proc. 8th Int. Conf. Discret. Elem. Methods. l (2019).

[133] Y. Yan, W. Vreeburg, G. Chen, C. Wheeler, Design of optimized convex pattern surface for wear tests in a test rig, ICBMH 2019 13th Int. Conf. Bulk Mater. Storage, Handl. Transp. Univ. Newcastle. (2019).

[134] P.A. Cundall, O.D.L. Strack, A discrete numerical model for granular assemblies, Geotechnique. 29 (1979) 47–65. https://doi.org/10.1680/GEOT.1979.29.1.47.

[135] C.J. Coetzee, Review: Calibration of the discrete element method, Powder Technol. 310 (2017) 104–142. https://doi.org/10.1016/j.powtec.2017.01.015.

[136] L. Zhao, X. Liu, J. Mao, D. Xu, A. Munjiza, E. Avital, A novel discrete element method based on the distance potential for arbitrary 2D convex elements, Int. J. Numer. Methods Eng. 115 (2018) 238–267. https://doi.org/10.1002/nme.5803.

[137] D.E.M. Solutions, EDEM 2.3 user guide, Edinburgh, Scotland, UK. (2010).

[138] J. Jäger, Elastic contact of equal spheres under oblique forces, Arch. Appl. Mech. 63 (1993) 402–412. https://doi.org/10.1007/BF00805740.

[139] C. Thornton, Interparticle sliding in the presence of adhesion, J. Phys. D. Appl. Phys. 24 (1991) 1942–1946. https://doi.org/10.1088/0022-3727/24/11/007.

[140] S.M. Derakhshani, D.L. Schott, G. Lodewijks, Micro-macro properties of quartz sand: Experimental investigation and DEM simulation, Powder Technol. 269 (2015) 127–138. https://doi.org/10.1016/j.powtec.2014.08.072.

[141] L. Xu, K. Luo, Y. Zhao, Numerical prediction of wear in SAG mills based on DEM simulations, Powder Technol. 329 (2018) 353–363. https://doi.org/10.1016/j.powtec.2018.02.004.

[142] D. Boemer, J.P. Ponthot, A generic wear prediction procedure based on the discrete element method for ball mill liners in the cement industry, Miner. Eng. 109 (2017) 55–79. https://doi.org/10.1016/j.mineng.2017.02.014.

[143] M.S. Powell, N.S. Weerasekara, S. Cole, R.D. Laroche, J. Favier, DEM modelling of liner evolution and its influence on grinding rate in ball mills, Miner. Eng. 24 (2011) 341–351. https://doi.org/10.1016/j.mineng.2010.12.012.

[144] C.M. Wensrich, A. Katterfeld, Rolling friction as a technique for modelling particle shape in DEM, Powder Technol. 217 (2012) 409–417. https://doi.org/10.1016/j.powtec.2011.10.057.

[145] C.J. Coetzee, Calibration of the discrete element method and the effect of particle shape, Powder Technol. 297 (2016) 50–70. https://doi.org/10.1016/j.powtec.2016.04.003.

[146] J. Ai, J.F. Chen, J.M. Rotter, J.Y. Ooi, Assessment of rolling resistance models in

discrete element simulations, Powder Technol. 206 (2011) 269–282. https://doi.org/10.1016/j.powtec.2010.09.030.

[147] K.M. Khan, G. Bushell, Comment on “rolling friction in the dynamic simulation of sandpile formation,” Phys. A Stat. Mech. Its Appl. 352 (2005) 522–524. https://doi.org/10.1016/j.physa.2005.01.019.

[148] J.F. Archard, Contact and rubbing of flat surfaces, J. Appl. Phys. 24 (1953) 981–988. https://doi.org/10.1063/1.1721448.

[149] X. Qui, A. Potapov, M. Song, L. Nordell, Prediction of Wear of Mill Lifters Using Discrete Element Method, 2001 SAG Conf. Proc. (2001) 2–7. ImpactoRecub.

[150] D. Forsström, P. Jonsén, Calibration and validation of a large scale abrasive wear model by coupling DEM-FEM: Local failure prediction from abrasive wear of tipper bodies during unloading of granular material, Eng. Fail. Anal. 66 (2016) 274–283. https://doi.org/10.1016/j.engfailanal.2016.04.007.

[151] T. Roessler, C. Richter, A. Katterfeld, F. Will, Development of a standard calibration procedure for the DEM parameters of cohesionless bulk materials – part I: Solving the problem of ambiguous parameter combinations, Powder Technol. 343 (2019) 803–812. https://doi.org/10.1016/j.powtec.2018.11.034.

[152] G. Li, L. Yu, S. Yang, An experimental and numerical study of the angle of repose of coarse spheres, 2011 2nd Int. Conf. Mech. Autom. Control Eng. MACE 2011 - Proc. 125 (2011) 267–270. https://doi.org/10.1109/MACE.2011.5986910.

[153] O. Kempthorne, The design and analysis of experiments, Wiley. (1952).

[154] B. Jones, C.J. Nachtsheim, A class of three-level designs for definitive screening in the presence of second-order effects, J. Qual. Technol. 43 (2011) 1–15. https://doi.org/10.1080/00224065.2011.11917841.

[155] D. Schulze, Powders and bulk solids: Behaviour, characterization, storage and flow. 2008, (2003).

[156] A. Svanberg, S. Larsson, R. Mäki, P. Jonsén, Full-scale simulation and validation of wear for a mining rope shovel bucket, Minerals. 11 (2021) 1–26. https://doi.org/10.3390/min11060623.

[157] G. Chen, Surface wear reduction of bulk solids handling equipment using bionic design, Delft University of Technology, 2017.

[158] Y. Yan, R. Helmons, C. Wheeler, D. Schott, Optimization of a convex pattern surface for sliding wear reduction based on a definitive screening design and discrete element method, Powder Technol. 394 (2021) 1094–1110. https://doi.org/10.1016/j.powtec.2021.09.041.

[159] Á. Kalácska, P. De Baets, D. Fauconnier, F. Schramm, L. Frerichs, J. Sukumaran, Abrasive wear behaviour of 27MnB5 steel used in agricultural tines, Wear. 442–443 (2020). https://doi.org/10.1016/j.wear.2019.203107.

[160] T.H. Phan, A.K. Tieu, H.T. Zhu, B.Y. Kosasih, Q. Wu, Q. Fan, D. Le Sun, A Study of Abrasive Wear on High Speed Steel Surface in Hot Rolling, Appl. Mech. Mater. 846 (2016) 589–594. https://doi.org/10.4028/www.scientific.net/amm.846.589.

[161] J. Franke, P.W. Cleary, M.D. Sinnott, How to account for operating condition variability when predicting liner operating life with DEM - A case study, Miner. Eng. 73 (2015) 53–68. https://doi.org/10.1016/j.mineng.2014.11.009.

[162] S. Ma, C. Niu, C. Yan, H. Tan, L. Xu, Discrete element method optimisation of a scraper to remove soil from ridges formed to cold-proof grapevines, Biosyst. Eng. 210 (2021) 156–170. https://doi.org/10.1016/j.biosystemseng.2021.08.014.

[163] E. Katinas, R. Chotěborský, M. Linda, V. Jankauskas, Wear modelling of soil ripper tine in sand and sandy clay by discrete element method, Biosyst. Eng. 188 (2019) 305–319. https://doi.org/10.1016/j.biosystemseng.2019.10.022.

[164] Y.T. Feng, D.R.J. Owen, Discrete element modelling of large scale particle systems—I: exact scaling laws, Comput. Part. Mech. 1 (2014) 159–168. https://doi.org/10.1007/s40571-014-0010-y.

[165] Y.T. Feng, K. Han, D.R.J. Owen, J. Loughran, On upscaling of discrete element models: Similarity principles, Eng. Comput. (Swansea, Wales). 26 (2009) 599–609. https://doi.org/10.1108/02644400910975405.

[166] A.P. Grima, P.W. Wypych, Development and validation of calibration methods for discrete element modelling, Granul. Matter. 13 (2011) 127–132. https://doi.org/10.1007/s10035-010-0197-4.

[167] D.S. Nasato, C. Goniva, S. Pirker, C. Kloss, Coarse graining for large-scale DEM simulations of particle flow - An investigation on contact and cohesion models, Procedia Eng. 102 (2015) 1484–1490. https://doi.org/10.1016/j.proeng.2015.01.282.

[168] M.J. Mohajeri, R.L.J. Helmons, C. van Rhee, D.L. Schott, A hybrid particle-geometric scaling approach for elasto-plastic adhesive DEM contact models, Powder Technol. 369 (2020) 72–87. https://doi.org/10.1016/j.powtec.2020.05.012.

[169] D. Queteschiner, T. Lichtenegger, S. Pirker, S. Schneiderbauer, Multi-level coarse-grain model of the DEM, Powder Technol. 338 (2018) 614–624. https://doi.org/10.1016/j.powtec.2018.07.033.

[170] D.L. Schott, S.W. Lommen, R. van Gils, J. de Lange, M.M. Kerklaan, O.M. Dessing, W. Vreugdenhil, G. Lodewijks, Scaling of particles and equipment by experiments of an excavation motion, Powder Technol. 278 (2015) 26–34. https://doi.org/10.1016/j.powtec.2015.03.012.

[171] T. Roessler, A. Katterfeld, Scaling of the angle of repose test and its influence on the calibration of DEM parameters using upscaled particles, Powder Technol. 330 (2018) 58–66. https://doi.org/10.1016/j.powtec.2018.01.044.

[172] M. Robinson, M. Ramaioli, S. Luding, Fluid-particle flow simulations using two-way-coupled mesoscale SPH-DEM and validation, Int. J. Multiph. Flow. 59 (2014) 121–134. https://doi.org/10.1016/j.ijmultiphaseflow.2013.11.003.

[173] S. Lommen, M. Mohajeri, G. Lodewijks, D. Schott, DEM particle upscaling for large-scale bulk handling equipment and material interaction, Powder Technol. 352 (2019) 273–282. https://doi.org/10.1016/j.powtec.2019.04.034.

[174] S.C. Thakur, J.Y. Ooi, H. Ahmadian, Scaling of discrete element model parameters for cohesionless and cohesive solid, Powder Technol. 293 (2016) 130–137. https://doi.org/10.1016/j.powtec.2015.05.051.

[175] T. Weinhart, C. Labra, S. Luding, J.Y. Ooi, Influence of coarse-graining parameters on the analysis of DEM simulations of silo flow, Powder Technol. 293 (2016) 138–148. https://doi.org/10.1016/j.powtec.2015.11.052.

[176] R. Cai, Y. Zhao, An experimentally validated coarse-grain DEM study of monodisperse granular mixing, Powder Technol. 361 (2020) 99–111. https://doi.org/10.1016/j.powtec.2019.10.023.

[177] P.M. Widartiningsih, Y. Mori, K. Takabatake, C.Y. Wu, K. Yokoi, A. Yamaguchi, M. Sakai, Coarse graining DEM simulations of a powder die-filling system, Powder Technol. 371 (2020) 83–95. https://doi.org/10.1016/j.powtec.2020.05.063.

[178] D. Antypov, J.A. Elliott, On an analytical solution for the damped Hertzian spring, Epl. 94 (2011). https://doi.org/10.1209/0295-5075/94/50004.

[179] A. Ramalho, J.C. Miranda, The relationship between wear and dissipated energy in sliding systems, Wear. 260 (2006) 361–367. https://doi.org/10.1016/j.wear.2005.02.121.

[180] A.B. Yu, X.Z. An, R.P. Zou, R.Y. Yang, K. Kendall, Self-assembly of particles for densest packing by mechanical vibration, Phys. Rev. Lett. 97 (2006) 95–98.

https://doi.org/10.1103/PhysRevLett.97.265501.

[181] X.Z. An, R.Y. Yang, R.P. Zou, A.B. Yu, Effect of vibration condition and inter-particle frictions on the packing of uniform spheres, Powder Technol. 188 (2008) 102–109. https://doi.org/10.1016/j.powtec.2008.04.001.

[182] X. Chen, Y. Liu, Finite element modeling and simulation with ANSYS Workbench, CRC press, 2014.

[183] G. Chen, D.L. Schott, G. Lodewijks, Sensitivity analysis of DEM prediction for sliding wear by single iron ore particle, Eng. Comput. (Swansea, Wales). 34 (2017) 2031–2053. https://doi.org/10.1108/EC-07-2016-0265.

[184] I. Hutchings, P. Shipway, Sliding wear, 2nd ed., Elsevier Ltd., 2017. https://doi.org/10.1016/b978-0-08-100910-9.00005-2.

[185] B.C. Burman, P.A. Cundall, O.D.L. Strack, A discrete numerical model for granular assemblies, Geotechnique. 30 (1980) 331–336. https://doi.org/10.1680/geot.1980.30.3.331.

[186] P.W. Cleary, Predicting charge motion, power draw, segregation and wear in ball mills using discrete element methods, Miner. Eng. 11 (1998) 1061–1080. https://doi.org/10.1016/s0892-6875(98)00093-4.

[187] P.W. Cleary, P. Owen, Development of models relating charge shape and power draw to SAG mill operating parameters and their use in devising mill operating strategies to account for liner wear, Miner. Eng. 117 (2018) 42–62. https://doi.org/10.1016/j.mineng.2017.12.007.

[188] P.W. Cleary, M. Sinnott, R. Morrison, Analysis of stirred mill performance using DEM simulation: Part 2 - Coherent flow structures, liner stress and wear, mixing and transport, Miner. Eng. 19 (2006) 1551–1572. https://doi.org/10.1016/j.mineng.2006.08.013.

[189] L. Xu, S. Bao, Y. Zhao, Multi-level DEM study on liner wear in tumbling mills for an engineering level approach, Powder Technol. 364 (2020) 332–342. https://doi.org/10.1016/j.powtec.2020.02.004.

[190] E. Rojas, V. Vergara, R. Soto, Case study: Discrete element modeling of wear in mining hoppers, Wear. 430–431 (2019) 120–125. https://doi.org/10.1016/j.wear.2019.04.020.

[191] J.T. Kalala, M.H. Moys, Discrete element method modelling of liner wear in dry ball milling, J. South African Inst. Min. Metall. 104 (2004) 597–602.

[192] J. de Bono, H. Li, G. McDowell, A new abrasive wear model for railway ballast, Soils Found. 60 (2020) 714–721. https://doi.org/10.1016/j.sandf.2020.05.001.

[193] L. Godino, I. Pombo, J. Girardot, J.A. Sanchez, I. Iordanoff, Modelling the wear evolution of a single alumina abrasive grain: Analyzing the influence of crystalline structure, J. Mater. Process. Technol. 277 (2020) 116464. https://doi.org/10.1016/j.jmatprotec.2019.116464.

[194] G. Chen, Y. Liu, G. Lodewijks, D.L. Schott, Experimental research on the determination of the coefficient of sliding wear under iron ore handling conditions, Tribol. Ind. 39 (2017) 378–390. https://doi.org/10.24874/ti.2017.39.03.13.

[195] L. Xu, K. Luo, Y. Zhao, J. Fan, K. Cen, Influence of particle shape on liner wear in tumbling mills: A DEM study, Powder Technol. 350 (2019) 26–35. https://doi.org/10.1016/j.powtec.2019.03.033.

[196] Y. Yan, R. Helmons, D. Schott, Pin-on-Disc Modelling with Mesh Deformation Using Discrete Element Method, Mater. 2022, Vol. 15, Page 1813. 15 (2022) 1813. https://doi.org/10.3390/MA15051813.

[197] S.J. Wiche, S. Keys, A.W. Roberts, Abrasion wear tester for bulk solids handling applications, Wear. 258 (2005) 251–257. https://doi.org/10.1016/j.wear.2004.09.014.

[198] Y. Yan, R. Helmons, D. Schott, The Influence of Particle Size on the Sliding Wear of the Con-vex Pattern Surface, Minerals. 12(2) (2021). https://doi.org/10.3390/min12020139.

Nomenclatur

Symbol	Unit	Description
a	mm	Major radius of convex
b	mm	Minor radius of convex
c	mm	Horizontal distance between two convexes
C_V	-	Coefficient of variation
d	mm	Vertical distance between two convexes
D_n	$N \cdot s/m$	Normal coefficient of damping
D_t	$N \cdot s/m$	Tangential coefficient of damping
F_n	N	Normal force
F_t	N	Tangential force
g	m/s^2	Gravitational acceleration
G	GPa	Shear modulus
h	mm	Height of convex
H_a	Pa^{-1}	Particle hardness
H_s	Pa^{-1}	Surface hardness
l	mm	Width of the particle bed
l_s	m	Sliding distance
m	kg/s	Mass flow rate
M_r	$N \cdot m$	Torque
n_i	-	Normal vector of a mesh element
p_c	-	Central point of a mesh element

p_1	-	Coordinates of first note of a triangular element
p_2	-	Coordinates of second note of a triangular element
p_3	-	Coordinates of third note of a triangular element
R	mm	Particle radius
S_n	N/m	Normal stiffness of spring
S_t	N/m	Tangential stiffness of spring
t	mm	Particle bed thickness
Δt	s	Time step
T_d	s	Discharge time
v_p	m/s	Particle velocity
v_t	m/s	Tangential velocity
v_{eff}	m/s	Particle efficient impact veloctity
W_v	mm^3	Wear volume
α_s	Pa^{-1}	Wear coefficient
α_{SB}	$\circ$	Shear angle of shear box test
α_{DD}	$\circ$	Shear angle of drawdown test
α_{ER}	-	Ratio of the equivalent radius of particle to that of convex
α_{PA}	-	Ratio of projected area of particle to that of convex
α_{SA}	-	Ratio of surface area of particle to that of convex
α_V	-	Ratio of volume of particle to that of convex
φ_R	-	Relative wear rate
γ	-	Relative wear rate
ρ	kg/m^3	Bulk density
σ	-	Standard deviation
μ	-	Mean
ω_{rel}	-	Relative angular velocity
ω	rad/s	Angular velocity
υ	-	Poisson ratio
φ	mm^3/mm	Wear rate

Acknowledgements

Time flies without any trace but my memories still excite me. The first day in the Netherlands is destined to be one of the most unforgettable moments in my life, where I started an extraordinary journey. The journey was tough, full of mud, and bitter-teared but it ascends me to a broader and broader future. At the end of the journey, I would like to acknowledge the ones who brought me hope and joy.

Dr. Dingena Schott, my promotor, thank you but only saying thank you is far less! I appreciate the routine meetings where you gave me supportive and critical suggestions. Every discussion with you gave me a new perspective on my research. You inspired me to dig deeper into the essence of every problem and challenge. During the unexpected special period, you encouraged me to keep confident and patient and always told me I was making progress and would be there on time. Thank you for allowing me to stay in China for almost one year because of my personal issue. Without your unconditional understanding and help, I could hardly finish this journey. My appreciation for you never ends and I wish you and your family all the best from my deep heart.

I would like to thank my daily supervisor, Dr. Rudy Helmons! I appreciate your rigorous and scientific attitude toward details no matter referring to data processing or content writing. You pushed me to pursue perfection and broke through my limits. When I caught problems, I could always walk by to you and seek a new point of view. Your encouragement and compliments motivated me to explore further and improve myself in all aspects. I also enjoyed the topics outside of the research work, which inspired me to jump out of my thinking settings to understand the differences in the world.

Apart from my promotors and supervisors, I also want to express my appreciation to my co-operators at the University of Newcastle, Australia. Thank you Prof. Craig Wheeler and Dr. Michael Carr for manufacturing the test samples and arranging experiments for me. With your support and aid, I obtained possibilities to convince myself of the value of my work. I would also appreciate the constructive feedback for several manuscripts.

I would like to thank the colleagues working in the Granular Characterisation and Modelling lab. My colleagues, Javad, Hamid, and Marc, provided me with supportive suggestions, and talking with you was always inspiring. It was enjoyable to have meetings

every week with you (Ana, Aaron, Ahmed, Hesam, Marc, Marcel, Jeseung, Jovana, Raïsa, Skirmantas, Saurav, Zhaorui) where we presented our works and collided thoughts. Apart from work, we also had joyful moments, chats, games, and voluntary services.

I would like to acknowledge the secretaries, giving special thanks to Dineke, Gracia, Patty, Anouk, Monique, and Pauline, the managers and the secretaries of the M&TT department, for all their daily support and organizing activities during holidays.

During this journey, friends brought me relaxing moments when I was in bad emotions. One of my officemates Adrien, I would like to thank you for your kindness and thoughtfulness. You dragged me from the dark time and made my confidence back. You always gave me constructive suggestions and made me to think of my furture futher and earlier. I would like to show my thanks to the colleagues with whom I had lunch together, Pan, Yimeng, Xiaohuan, Changyuan, Mingxin, Zhe, Jian, Xiuhan, Evelien, Annabel, Nikos, Jesper and others. I also enjoyed the basketball time every week with my friends, Chao, Fengqi, Rui, Mingyan, Hanqing, Jian, Yi, Longyu and everyone we played together. Yongli, we met four years ago in a conference and became good friends.

I want to say thank you to all of my family members. To my parents and my sisters, with your encouragement, inspiration, and love, I can pursue my goals without worries. Your dedication engraves in my heart and I hope I make you proud. I also would like to thank my parents-in-law. Thank you for supporting and understanding me and caring my wife and daughter.

Finally yet importantly, I would like to thank my wife and my daughter. My wife, Hong, your sacrifice for our family is priceless and I promise you a great future. My daughter, Yihe, you are my angel and my sunshine. Only seeing you smiling melts my heart! I wish you happy every second.

November 9, 2022, Yunpeng Yan, Delft

Curriculum Vitae

Yunpeng Yan received the B.Sc. degree in Agricultural Mechanization and its Automation at Shandong Agricultural University, Shandong, China, from September 2011 to June 2015. At the same year, he started his master in Agricultural Mechanization Engineering at the Key Laboratory of Bionic Engineering, Jilin University, China, from September 2015 to June 2018.

Granted by the China Scholarship Council, Yunpeng Yan started his PhD research in November 2018 at the Department of Maritime Technology and Transport, Faulty of Mechanical, Maritime and Materials Engineering, Delft University of Technology, the Netherlands, under the supervision of Dr.ir Dingena Schott and Dr.ir Rudy Helmons. His research interests include discrete element method, optimization design, numerical modelling, and surface deformation reconstruction.

Publications

Journal papers

1. Yan, Y., Helmons, R., Wheeler, C., & Schott, D. (2021). Optimization of a convex pattern surface for sliding wear reduction based on a definitive screening design and discrete element method. Powder Technology, 394, 1094-1110. https://doi.org/10.1016/j.powtec.2021.09.041

2. Yan, Y., Helmons, R. L. J., & Schott, D. L. (2022). Pin-on-Disc Modelling with Mesh Deformation Using Discrete Element Method. Materials, 15(5), [1813]. https://doi.org/10.3390/ma15051813

3. Yan, Y., Helmons, R. L. J., & Schott, D. L. (2022). The Influence of Particle Size on Sliding Wear of a Convex Pattern Surface. Minerals, 12(2), [139]. https://doi.org/10.3390/min12020139

4. Yan, Y., Helmons, R., Carr, M., Wheeler, C., & Schott, D. “Surface deformation of A Convex Pattern Surface Using DEM with Deformable Geometry Technique”. Submitted to Powder Technology.

Conference papers

1. Yan, Y., Vreeburg, W., Chen, G., Wheeler, C., & Schott, D. (2019). Design of Optimized Convex Pattern Surface for Wear Tests in A Test Rig. 13th International Conference on Bulk Materials Storage, Handling and Transportation.
2. Yan, Y., Vreeburg, W., Chen, G., & Schott, D. (2019). Minimization of wear in a transfer chute by geometric optimization of convex pattern surface: A DEM study. In Proceedings of the 8th International Conference on Discrete Element Methods (DEM8). Oral presentation.
3. Yan, Y., Helmons, R., Carr, M., Wheeler, C., & Schott, D. (2022). Wear modelling of a convex pattern surface using DEM. In Proceedings of the 10th International Conference on Conveying and Handling of Particulate Solids. Oral presentation.
4. Yan, Yunpeng, Rudy Helmons, Dingena Schott. "Wear deformation of a convex pattern surface using DEM and deformable geometry technique", In Proceedings of the World Congress on Particle Technology (WCPT9). Spain, 2022. Oral presentation.

Samenvatting

Bulk handling speelt een belangrijke rol in tal van industrieën, zoals de mijnbouw, landbouw, chemische en farmaceutische industrie. Voor de mijnbouw leidt de economische ontwikkeling tot een toenemende vraag naar staal en daarmee de grondstoffen die voor de staalproductie worden gebruikt, zoals kolen en ijzererts. Omgaan met bulk materiaal leidt tot ernstige slijtage van bulk handling apparatuur vanwege de ontelbare contacten tussen materialen en apparatuur oppervlakken. De slijtage veroorzaakt oppervlaktevervorming en verslechtering van de handling apparatuur, wat zorgt voor een verhoogd risico op vermindering van de levensduur van de machine.

Geïnspireerd door een bionische ontwerpmethode, pastte een eerdere studie een convex patroon toe op een transfertrechter om slijtage veroorzaakt door bulk materiaal te verminderen. De convexe patroonconfiguratie wordt voorgesteld door biologische morfologieën te zoeken en de overeenkomstige mechanismes voor slijtagevermindering van elke morfologie te categoriseren. Een numerieke studie gebaseerd op het Archard-slijtagemodel met behulp van de discrete-elementenmethode (DEM) geeft aan dat het convexe patroonoppervlak de abrasieve slijtage met 63% kan verminderen in vergelijking met een glad oppervlak.

In navolging van de vorige studie, heeft dit proefschrift tot doel de principes van de convexe configuratie op slijtagevermindering voor bulk handling apparatuur bloot te leggen en de oppervlaktevervorming als gevolg van het contact met bulk materiaal te voorspellen. Voor de oppervlaktevervorming, door meerdere numerieke methoden te evalueren, heeft DEM met vervormbare geometrietechniek het voordeel om bulk materiaal en oppervlaktevervorming effectief en nauwkeurig te integreren.

Dit proefschrift bestaat uit twee delen. Het eerste deel gaat in op de slijtagemechanismen van het convexe patroonoppervlak met niet-vervormbare geometrie om slijtage te verminderen. Het tweede deel modelleert de oppervlaktevervorming veroorzaakt door contact van één enkel deeltje en meerdere contacten van bulk materiaal afzonderlijk.

De convexe configuratie is geoptimaliseerd op basis van een ontwerp-van-experimentenbenadering. Door een ‘definitive screening design (DSD)’ toe te passen, worden zes factoren, waaronder twee operationele condities op drie niveaus, geëvalueerd. Door de combinatie van ontwerpfactoren wordt onderscheid gemaakt tussen twee type stromingen, namelijk continu en discontinu stromingsregime. Hoewel het discontinue stroomregime in staat is om slijtage te verminderen, wordt dit gebied niet meegenomen omdat het ernstige deeltjesaccumulatie veroorzaakt. Voor het continue stroomregime geeft een regressiemodel aan dat drie individuele factoren en één interactie een significant effect hebben op de slijtagesnelheid. Het ontwerp met de laagste slijtagesnelheid wordt beschouwd als een referentie voor de volgende studie. Het numerieke resultaat houdt in dat het convexe patroonmonster slijtage vermindert in vergelijking met een gewoon monster, omdat het het bulkstroomgedrag verandert. Zo wordt het rollen van deeltjes gestimuleerd en glijden van deeltjes vertraagd.

Aangezien bulkverwerkingsapparatuur meerdere materialen met verschillende verdelingen van deeltjesgrootte behandelt, is het essentieel om het effect van deeltjesgrootte op glijdende slijtage van het convexe patroonmonster te begrijpen. Een grove korreltechniek, die wordt gebruikt om de rekentijd te verminderen door fysieke deeltjes te vervangen door representatieve pakketten, is geïmplementeerd om de effectiviteit van het referentiemonster op vermindering van glijdende slijtage te evalueren. Het resultaat toont aan dat wanneer de deeltjesstraal kleiner is dan de equivalente straal van de het convexe oppervlak, het convexe patroonmonster slijtage vermindert door het stromingsgedrag van deeltjes te veranderen. Anders gaan de deeltjes door het convexe patroon, waardoor de weerstand van de deeltjes verandert en daardoor de slijtage toeneemt.

Aangezien de mechanismen van het convexe patroonmonster op slijtagevermindering worden onthuld, is het cruciaal om de effectiviteit te onderzoeken van het monster dat onderhevig is aan oppervlaktevervorming als gevolg van slijtage. DEM gecombineerd met een vervormbare geometrietechniek wordt geïmplementeerd om de oppervlaktevervorming als gevolg van slijtage te modelleren. Als benchmark wordt een enkele contacttest, namelijk een pin-on-disc-test, uitgevoerd om de haalbaarheid van het numerieke model te evalueren. Drie slijtage-eigenschappen van een vermaasde schijf, waaronder slijtagediepte, slijtagebreedte en slijtagevolume, worden vergeleken met de testresultaten. De gevoeligheid van de maaswijdte geeft aan dat de maaswijdte het slijtagevolume doet convergeren, maar het heeft een significant effect op de vorm van de slijtagecontour. Na het ervaren van een inloopfase, tonen de numerieke resultaten aan dat door de slijtagecoëfficiënt van het Archard-slijtagemodel goed op te schalen en de elementgrootte te selecteren, de langdurige of grootschalige laboratorium test worden gemodelleerd door een korte- of numerieke simulatie op korte afstand. Het schaaleffect maakt het mogelijk om de rekentijd aanzienlijk te verminderen met een veelbelovende rekennauwkeurigheid.

Verder wordt de oppervlaktevervorming van een convex patroonmonster als gevolg van het contact met bulkmateriaal gemodelleerd. De slijtage-experimenten zijn uitgevoerd op een cirkelvormige slijtagetester en de resultaten tonen aan dat het convexe patroonmonster de slijtage met 43% vermindert in vergelijking met een gewoon monster na het experiment van 56 uur. Om de vervorming van het convexe patroonmonster te onderzoeken, wordt de slijtagecontour gereconstrueerd op basis van de puntenwolk verkregen uit 3D-scanning. Het numerieke model wordt gevalideerd door het slijtagevolume van een gewoon monster te vergelijken tussen het simulatie- en het slijtage-experiment. De simulatieresultaten geven aan dat het vervormde convexe patroonoppervlak de glijdende slijtage blijft verminderen in vergelijking met een gewoon monster en dat de reductieprestaties afnemen naarmate de slijtage evolueert. Aan de andere kant speelt de deeltjesgrootte een belangrijke rol in de effectiviteit van slijtagevermindering op het convexe patroonmonster. De slijtage veroorzaakt door contact met de deeltjes overeenkomend met een lagere schaalfactor is minder dan die overeenkomt met een hogere. Dit ligt in lijn met de studie met niet-vervormbare geometrie.

Samenvattend, het convexe patroonoppervlak vermindert slijtage omdat het vloeigedrag van bulkmateriaal verandert door het rollen te stimulerenen het glijden van individuele deeltjes te verminderen. Zoals aangegeven in een gevalideerd numeriek model, ondermijnt de oppervlaktevervorming de effectiviteit van het convexe patroon omdat het de mogelijkheid om het bulkstroomgedrag te veranderen vermindert. Vergeleken met een gewoon monster, blijft het convexe patroonmonster de slijtage verminderen met de oppervlaktevervorming.

Verder onderzoek moet gericht zijn op langdurige en grootschalige laboratorium experimenten. Ook moet de haalbaarheid worden geëvalueerd in hoeverre het convexe patroonoppervlak kan worden toegepast op industriële machines, welke te maken hebben met ernstige slijtage.

TRAIL Thesis Series

The following list contains the most recent dissertations in the TRAIL Thesis Series. For a complete overview of more than 275 titles see the TRAIL website: www.rsTRAIL.nl.

The TRAIL Thesis Series is a series of the Netherlands TRAIL Research School on transport, infrastructure and logistics.

Yan, Y., *Wear Behaviour of A Convex Pattern Surface for Bulk Handling Equipment,* T2022/16, December 2022, TRAIL Thesis Series, the Netherlands

Giudici, A., *Cooperation, Reliability, and Matching in Inland Freight Transport*, T2022/15, December 2022, TRAIL Thesis Series, the Netherlands

Nadi Najafabadi, A., *Data-Driven Modelling of Routing and Scheduling in Freight Transport*, T2022/14, October 2022, TRAIL Thesis Series, the Netherlands

Heuvel, J. van den, *Mind Your Passenger! The passenger capacity of platforms at railway stations in the Netherlands*, T2022/13, October 2022, TRAIL Thesis Series, the Netherlands

Haas, M. de, *Longitudinal Studies in Travel Behaviour Research*, T2022/12, October 2022, TRAIL Thesis Series, the Netherlands

Dixit, M., *Transit Performance Assessment and Route Choice Modelling Using Smart Card Data*, T2022/11, October 2022, TRAIL Thesis Series, the Netherlands

Du, Z., *Cooperative Control of Autonomous Multi-Vessel Systems for Floating Object Manipulation*, T2022/10, September 2022, TRAIL Thesis Series, the Netherlands

Larsen, R.B., *Real-time Co-planning in Synchromodal Transport Networks using Model Predictive Control*, T2022/9, September 2022, TRAIL Thesis Series, the Netherlands

Zeinaly, Y., *Model-based Control of Large-scale Baggage Handling Systems: Leveraging the theory of linear positive systems for robust scalable control design*, T2022/8, June 2022, TRAIL Thesis Series, the Netherlands

Fahim, P.B.M., *The Future of Ports in the Physical Internet*, T2022/7, May 2022, TRAIL Thesis Series, the Netherlands

Huang, B., *Assessing Reference Dependence in Travel Choice Behaviour*, T2022/6, May 2022, TRAIL Thesis Series, the Netherlands

Reggiani, G., *A Multiscale View on Bikeability of Urban Networks*, T2022/5, May 2022, TRAIL Thesis Series, the Netherlands

Paul, J., *Online Grocery Operations in Omni-channel Retailing: opportunities and challenges*, T2022/4, March 2022, TRAIL Thesis Series, the Netherlands

Liu, M., *Cooperative Urban Driving Strategies at Signalized Intersections*, T2022/3, January 2022, TRAIL Thesis Series, the Netherlands

Feng, Y., *Pedestrian Wayfinding and Evacuation in Virtual Reality*, T2022/2, January 2022, TRAIL Thesis Series, the Netherlands

Scheepmaker, G.M., *Energy-efficient Train Timetabling*, T2022/1, January 2022, TRAIL Thesis Series, the Netherlands

Bhoopalam, A., *Truck Platooning: planning and behaviour*, T2021/32, December 2021, TRAIL Thesis Series, the Netherlands

Hartleb, J., *Public Transport and Passengers: optimization models that consider travel demand*, T2021/31, TRAIL Thesis Series, the Netherlands

Azadeh, K., *Robotized Warehouses: design and performance analysis*, T2021/30, TRAIL Thesis Series, the Netherlands

Chen, N., *Coordination Strategies of Connected and Automated Vehicles near On-ramp Bottlenecks on Motorways*, T2021/29, December 2021, TRAIL Thesis Series, the Netherlands

Onstein, A.T.C., *Factors influencing Physical Distribution Structure Design*, T2021/28, December 2021, TRAIL Thesis Series, the Netherlands

Olde Kalter, M.-J. T., *Dynamics in Mode Choice Behaviour*, T2021/27, November 2021, TRAIL Thesis Series, the Netherlands

Los, J., *Solving Large-Scale Dynamic Collaborative Vehicle Routing Problems: an Auction-Based Multi-Agent Approach*, T2021/26, November 2021, TRAIL Thesis Series, the Netherlands